UNIVERSITÀ DEGLI STUDI
DI MODENA E REGGIO EMILIA

Doctoral School in Industrial Innovation Engineering

Cycle XXXVIII

Design, simulation, prototyping and testing of a new vibrating membrane suitable to enhance the acquisition of lung sounds in electronic stethoscopes

Supervisor
Prof. Dr. Fabrizio Pancaldi

PhD Candidate
Marco Modena

PhD Course Coordinator
Prof. Dr. Franco Zambonelli

Academic Year 2024–2025

“If I have seen further it is by standing on the shoulders of giants”

– Isaac Newton

Dedicato alla mia famiglia

Contents

Nomenclature

AAV	ANCA-Associated Vasculitis
AE	Acute Exacerbation
CTD	Connective Tissue Disease
DLCO	Diffusing capacity of the Lung for Carbon Monoxide
DM	Dermatomyositis
DOE	Design of Experiment
FRF	Frequency Response Function
GPA	Granulomatosis with PolyAngiitis
HRCT	High-Resolution Computed Tomography
ICT	Information and Communication Technology
ILD	Interstitial Lung Disease
IPF	Idiopathic Pulmonary Fibrosis
MCTD	Mixed Connective Tissue Disease
MEMS	Micro Electro Mechanical System
MPA	Microscopic PolyAngiitis
NHSs	National Health Systems
NLPQL	NonLinear Programming Quadratic Lagrangian
PFT	Pulmonary Function Test
PH	Pulmonary Hypertension
PM	Polymyositis
pSS	Primary Sjögren's syndrome

QOL	Quality Of Life
RA	Rheumatoid Arthritis
SLE	Systemic Lupus Erythematosus
SSc	Systemic Sclerosis

Abstract

Lung involvement is a frequent and clinically relevant comorbidity in a wide spectrum of diseases, including connective tissue diseases, Sjögren's syndrome, rheumatoid arthritis, systemic vasculitides, and viral infections such as COVID-19. Despite their diverse etiologies, these conditions often converge toward interstitial lung disease (ILD), a major determinant of morbidity and mortality. Early identification of ILD remains a crucial yet challenging goal, as early clinical manifestations are often subtle and typically become evident only at advanced stages. Current diagnostic methods, particularly high resolution computed tomography (HRCT), are unsuitable for routine screening due to cost and radiation exposure.

Physical examination, specifically lung auscultation, offers a simple, reproducible, and non invasive means for early ILD detection. "Velcro-like" crackles are characteristic of fibrotic involvement of the lung parenchyma and correlate with radiologic findings such as honeycombing and ground glass opacities. In recent years, the automated detection and classification of pathological lung sounds has become an active field of research, leveraging digital signal processing and machine learning. However, the lack of standardization in data acquisition and the limited sensitivity of current electronic stethoscopes restrict diagnostic performance.

The scope of this thesis consists of designing, simulating, developing, and testing a novel vibrating membrane, also known as diaphragm, specifically optimized for pulmonary sound acquisition. The new diaphragm is intended to enhance the performance of electronic stethoscopes in terms of acoustic bandwidth and sensitivity.

To this aim, an initial simulation model representing the current non-optimized membrane configuration was developed and validated against reference data, with a commercial diaphragm produced by Littmann used as a benchmark, designed as a compromise between cardiac and pulmonary auscultation. Once the model was verified, it was employed to determine the optimal design parameters maximizing the membrane's dynamic performance. By improving the mechanical response, the proposed membrane enables the system to capture lung sounds with richer spectral content and higher signal quality, thus providing a more informative input for subsequent computational and diagnostic analysis.

The research integrates analytical modeling, one-dimensional (1D) and two/three-dimensional (2D/3D) simulations, and experimental prototyping. The membrane geometry and material parameters were systematically optimized to extend frequency response and pressure gain while maintaining structural integrity. The de-

veloped prototypes have been tested in an experimental setup composed by a programmable shaker, an accelerometer and a laser vibrometer. The shaker provides the excitation to the vibrating membrane, whereas the sensors allow to acquire the force applied to the diaphragm and the related displacement. The tested prototypes demonstrated strong agreement with the simulated models, confirming the validity of the numerical approach and establishing it as a valuable design tool for future membrane development. In particular, the proposed design improves the quality of the acquired signal and lays the foundation for more reliable automated identification of pathological pulmonary sounds, ultimately contributing to earlier diagnosis of ILD and related disorders.

This work thus bridges clinical needs and engineering innovation, offering a technological advancement that may support more effective, less expensive and non invasive screening strategies for interstitial lung disease.

1 Introduction

1.1 Clinical Contest, Scope and Structure of the Thesis

Pulmonary involvement represents a frequent complication in a wide range of pathological conditions. These include autoimmune diseases, such as Sjögren's syndrome and rheumatoid arthritis, viral infections including COVID-19, and systemic vasculitides. Although characterized by distinct pathophysiological mechanisms, these disorders often converge on a common clinical outcome, namely interstitial lung disease (ILD).

Sjögren's syndrome and rheumatoid arthritis are connective tissue diseases (CTDs). Rheumatoid arthritis (RA) is an autoimmune disease impacting around 1% of population [1]. The first symptom to emerge is swelling of the joints then the disease gradually causes pain, chronic pain and even deformity of joints. The most severe comorbidities are cardiovascular disease and interstitial lung disease (ILD). Posterior statistics and retrospective studies have shown that the life expectancy of individuals diagnosed with secondary ILD to RA (RA-ILD) is very low, on the order of 3-8 years [10, 8]. In practice, the lung parenchyma is replaced by fibrotic tissue with a reduced capability to exchange oxygen and carbon dioxide between blood and air. Currently, only one drug can halt the progression of ILD, but it is effective only if administered at the very early stages of the disease. The pathogenesis of RA and RA-ILD is almost unknown, as well as the onset of RA-ILD is not predictable. Symptoms emerge late in the clinical history and are not useful for diagnosis. In fact, patients can be asymptomatic at the early stages of the disease, and some suggestive clinical manifestations, such as dyspnea, fatigue and cough, can also derive from extra-pulmonary causes.

Since pulmonary involvement and interstitial lung disease constitute a shared clinical endpoint of several pathological conditions, timely and, when necessary, remote diagnostic strategies are crucial. The coronavirus disease 2019 (COVID-19) pandemic has highlighted this need, placing unprecedented pressure on healthcare systems worldwide. In particular, the remote monitoring of patients with few or mild symptoms has become a major challenge in settings where hospital access is limited or discouraged. Early detection of interstitial pneumonia is therefore essential to optimize patient outcomes.

ANCA-associated vasculitides (AAV) comprises a group of autoimmune disorders primarily targeting small blood vessels. The principal forms include granulomatosis with polyangiitis (GPA), microscopic polyangiitis (MPA), and eosinophilic granulomatosis with polyangiitis (EGPA) [43].

Pulmonary involvement is common in these conditions, though the patterns and severity vary among the different types. In recent years, increasing attention has been directed toward ILD, which appears to be more prevalent in MPA, affecting up to 45% of patients, compared to GPA, where it occurs in approximately 23% of cases [43].

High-resolution computed tomography (HRCT) is the gold standard for the diagnosis of ILD and it is mandatory in case of suspected ILD. Nevertheless, routine use of HRCT for screening programs is not recommended due to both the high costs imposed on the national health system (NHS) and patients' exposure to ionizing radiation. To enhance the appropriate use of HRCT for early ILD diagnosis, physical lung examination has been suggested as a simple and reproducible screening method. Indeed, lung auscultation can detect fine bibasilar, end-inspiratory, "velcro-like" crackles, which may precede the development of clinically overt ILD. Velcro crackles generated in the lung parenchyma has been independently associated with different radiological patterns, namely honeycombing, ground glass and traction bronchiectasis [74].

The detection and/or classification of abnormal lung sounds represents a well consolidated field of research. On one hand, numerous studies focus on classifying lung sounds obtained from diverse datasets. The term 'diverse datasets,' refers to collections of lung sounds originating from different sources, which were not consistently recorded following standardized procedures. Pancaldi et al. [75] presented a processing pipeline based of time-frequency analysis through STFT, identification of the inspiration period, bandwidth computation and hard thresholding. The overall accuracy over a RA-ILD dataset of 137 patients was 83.9% [57]. Manfredi et al. [7] utilized an algorithmic approach for diagnosing ILD secondary to connective tissue diseases (CTD). The idea behind the work [7] consists of considering velcro crackles as voiced/unvoiced sounds and filtering them through linear predictive coding. Principal component analysis and hard thresholding is used for classification. The processing chain workflow is thoroughly detailed in [33]. The overall diagnostic accuracy was 82.6%. The overall diagnostic accuracy for CTD-ILD was 91%. Fava et al. [32] proposed an algorithmic approach to clean the datasets of lung sounds from "bad" auscultations. Bad auscultation is a lung sounds where the useful respiratory signal is absent or is overcome by noise or artifacts. Pre-processing is based on VMD and harmonic-percussive source separation (HPSS) [76]. Classification into good and bad signal is performed through the k-nearest neighbors (KNN) algorithm. The overall accuracy of the DNN developed in [73] applied to the clean dataset in the diagnosis of CTD-ILD and RA-ILD is 97% and 68%, respectively. Unlike the impressive performance of the DNN presented in [73, 32] for the diagnosis of CTD-ILD, the overall accuracy of the same DNN for the diagnosis of RA-ILD can be

considered rather limited.

The scope of this thesis consists of designing, simulating and realizing a novel vibrating membrane for electronic stethoscopes, with the aim of maximizing both bandwidth and sensitivity thus producing a better quality signal. By optimizing the membrane to achieve a broader frequency range and higher pressure gain, the acoustic signal collected during chest auscultation preserves richer spectral content, while the system exhibits greater sensitivity, providing a more informative input for subsequent analysis. Through improved frequency analysis, this approach facilitates a clearer characterization of pulmonary acoustic components. To this end, modifications of the membrane stiffness distribution are investigated in order to improve bandwidth while preserving sensitivity.

The structure of this manuscript is organized as follows. **Chapter 2** provides a comprehensive overview of the clinical background. In **Chapter 3**, electronic stethoscopes are introduced, highlighting their functionalities, advantages, and existing challenges. **Chapter 4** details the validation of the proposed framework in both one-dimensional and multi-dimensional (2D/3D) configurations. **Chapter 5** is dedicated to the optimization and prototyping of the membranes. Finally, **Chapter 6** presents the conclusions and discusses potential directions for future research.

2 Clinical Background and Problem Statement

2.1 Introduction

Pulmonary involvement in autoimmune diseases represents a significant clinical challenge and is increasingly recognized as a major contributor to patient morbidity and mortality [7]. Among these conditions are viral infections such as COVID-19, systemic vasculitides, and connective tissue diseases (CTDs), including rheumatoid arthritis (RA), Sjögren's syndrome, systemic sclerosis, polymyositis, dermatomyositis and mixed connective tissue disease also frequently present interstitial lung disease (ILD) as a serious complication [32]. The presence of ILD in these patients not only worsens their prognosis but also complicates therapeutic management due to overlapping systemic inflammation and lung pathology [32].

Interstitial lung disease comprises a heterogeneous group of disorders characterized by inflammation and fibrosis of the pulmonary interstitium, ultimately leading to impaired gas exchange of oxygen and carbon dioxide between blood and air, progressive respiratory failure, and increased mortality. The clinical course of ILD in autoimmune diseases is often insidious, with symptoms such as exertional dyspnea and non-productive cough appearing late, after significant lung damage has occurred. Early diagnosis of ILD is therefore essential to allow timely intervention aimed at halting or slowing fibrotic progression [73].

Despite advances in imaging and pulmonary function testing, early identification of ILD remains challenging. High-resolution computed tomography (HRCT) is considered the gold standard for detecting lung fibrosis and other ILD patterns, but its routine use for screening purposes is limited by cost, radiation exposure, and availability constraints. Pulmonary function tests (PFTs) provide functional insight but often lack sensitivity in early disease stages, as patients may compensate for mild fibrosis through increased ventilatory effort [32].

In this context, lung auscultation offers a valuable, non-invasive, bedside approach. Specifically, the presence of "velcro crackles," fine inspiratory sounds resembling the separation of hook and loop fasteners, has been recognized as an early clinical marker of pulmonary fibrosis. However, traditional auscultation is subject to significant interobserver variability and depends on clinician expertise [7].

Recent technological advances have fostered the development of electronic auscultation devices, capable of acquiring high-fidelity lung sounds combined with sophisticated signal processing and machine learning algorithms for automatic detection and classification of pathological sounds [33]. Among these innovations, vibrating membrane sensors have shown promise in enhancing sound acquisition quality while minimizing ambient noise interference.

This chapter offers a comprehensive overview of the clinical significance and epidemiology of pulmonary involvement in RA, CTDs, and Sjögren's syndrome, with additional consideration of COVID-19 and vasculitides. It further explores the diagnostic potential of lung sound analysis and highlights recent technological advances in electronic auscultation relevant to the present PhD project. Although the core of the thesis focuses on the vibrating membrane of electronic stethoscopes, the included articles are highly relevant as they provide the necessary foundations by addressing both disease contexts and the reliability of the devices.

2.2 Pulmonary Implications of Chronic Connective Tissue Diseases

The chronic diseases of interest most common are: connective tissue diseases such as rheumatoid arthritis and Sjögren's syndrome. These diseases can lead to complications and progress into interstitial lung diseases.

Connective tissue diseases (CTDs) represent a broad spectrum of systemic autoimmune disorders characterized by immune-mediated inflammation affecting various organs, including the lungs. Pulmonary complications in CTDs, especially interstitial lung disease (ILD), are among the most frequent and severe extra-articular manifestations. These complications significantly influence morbidity and mortality, often dictating patient prognosis and therapeutic decisions [32].

Systemic sclerosis (SSc), polymyositis, dermatomyositis, and mixed connective tissue disease (MCTD) are notable CTDs with a high incidence of lung involvement. Among these, systemic sclerosis-associated interstitial lung disease (SSc-ILD) is particularly prevalent. Overall, lung involvement, including ILD, pulmonary hypertension (PH), or a combination of both, affects more than 70% of patients with SSc, while pulmonary vascular disease, primarily pulmonary arterial hypertension, occurs in 10–40% of cases [19]. The onset and progression of ILD in CTDs are heterogeneous, with some patients experiencing rapid deterioration while others show a more indolent course.

Connective tissue disease associated interstitial lung disease (CTD-ILD) encompasses a group of systemic autoimmune disorders that result in interstitial abnormalities or pulmonary fibrosis. The pathogenesis of CTD-ILD remains incompletely understood due to disease heterogeneity and the lack of preclinical models. Some

risk factors overlap with those of idiopathic pulmonary fibrosis, including genetic predispositions and environmental exposures. A key mechanism appears to involve alveolar type II cell dysfunction, which triggers multiple profibrotic pathways, including inflammatory cascades, leading to fibroblast proliferation and activation. This results in abnormal lung remodeling and aberrant repair, ultimately causing interstitial fibrosis. In CTD-ILD, dysregulation of regulatory inflammatory pathways is a major contributing factor. Understanding these mechanisms is crucial for the development of targeted therapies and for identifying biomarkers that can aid in early diagnosis, clinical monitoring, and prognostication [20].

Early identification of ILD in CTDs is crucial to initiate immunosuppressive or antifibrotic therapies aimed at limiting lung damage and improving survival. However, early diagnosis remains problematic due to subtle or absent initial respiratory symptoms and the limitations of conventional diagnostic tools. HRCT is the reference imaging technique, providing detailed characterization of fibrosis and inflammation, yet its routine use is limited by cost, radiation concerns, and accessibility issues. Pulmonary function tests (PFTs) are supportive but often insufficiently sensitive for detecting early disease.

Physical lung examination, specifically auscultation, can reveal fine inspiratory crackles ("velcro crackles"), which are correlated with fibrotic changes on imaging. However, standard auscultation is operator dependent and subjective, limiting its reliability in clinical practice [32][7][74].

The clinical challenges described above translate into specific technical requirements for lung sound acquisition systems. Velcro crackles are brief, high-frequency acoustic events often occurring at low amplitude, particularly in early-stage disease. Therefore, detection of these signals requires transducing element with adequate bandwidth to capture high-frequency components and sufficient sensitivity to detect weak acoustic vibrations in the presence of physiological background noise. Additionally, reproducibility and operator independence demand stable mechanical and acoustic performance. These considerations define the design constraints for the development and optimization of the sensing element, highlighting the importance of improving bandwidth and sensitivity in order to enhance early ILD detection.

Connective tissue diseases, comprising systemic sclerosis (SSc), polymyositis (PM) / dermatomyositis (DM), mixed connective tissue disease (MCTD), and others, collectively affect millions worldwide. Pulmonary involvement, primarily ILD, is a leading cause of morbidity and mortality in these diseases.

ILD is the leading cause of death in SSc patients, accounting for approximately one-third of mortality in this population [21].

In a retrospective study of 156 patients with PM and DM, 36 patients (23.1%) developed interstitial lung disease (ILD). Among these, 19.4% showed resolution of pulmonary abnormalities, whereas 25% experienced disease progression. Morbidity and mortality rates in PM/DM patients with ILD were 13.9% and 36.4%,

respectively [22]. ILD in these diseases is often associated with a worse prognosis, particularly in subsets with rapidly progressive disease.

Acute exacerbation (AE) is a possible manifestation of interstitial lung diseases (ILD) associated to very high mortality. It's defined as clinically significant respiratory deterioration with evidence of new widespread alveolar abnormalities on computed tomography scan. AE is better described in idiopathic pulmonary fibrosis (IPF) but also reported in ILD secondary to CTD and vasculitis. The main features and the real clinical impact of this severe complication in these patients are not well defined. AE occurred in 9/78 patients, with an incidence of 5.77/100 patients/year, and 5/9 patients died because of AE. The baseline value of DLCO was significantly associated to the risk of AE at Cox regression. In patients with ILD related to rheumatic systemic diseases AE can occur with an incidence similar to IPF [23].

Although lung involvement can profoundly affect the clinical course and prognosis, standardized assessment of ILD is not well established across all CTDs. Routine evaluation is relatively better defined in patients with systemic sclerosis (SSc) [24], but less commonly implemented for other CTDs, such as primary Sjögren's syndrome (pSS) or systemic lupus erythematosus (SLE), which may also develop ILD[25], [26, 27, 28]. Emerging evidence indicates that severe ILD may be more prevalent in non-SSc CTDs than previously recognized; however, the lack of routine screening often leads to delayed diagnosis [7].

2.2.1 Rheumatoid Arthritis and Interstitial Lung Disease

Rheumatoid arthritis is a chronic systemic autoimmune disease primarily characterized by symmetric polyarthritis leading to joint destruction. Extra-articular manifestations are common and diverse, with pulmonary involvement being one of the most severe and prognostically relevant complications. Among these, rheumatoid arthritis associated interstitial lung disease (RA-ILD) affects a significant subset of patients, contributing to increased morbidity and mortality.

Rheumatoid arthritis (RA) is a chronic systemic autoimmune disease affecting approximately 1% of the adult population worldwide, with a higher prevalence in women and individuals aged between 40 and 60 years [1, 2].

Among RA patients, one of the most severe extra-articular complications is interstitial lung disease (ILD), which occurs in about 5% of cases in clinically significant form. However, the use of more sensitive imaging techniques, such as high-resolution computed tomography (HRCT), reveals a prevalence of subclinical lung involvement reaching and exceeding 30% of RA patients [3, 4]. Interstitial lung disease (ILD) is a common extra-articular manifestation in patients affected by RA, with a prevalence ranging between 19% and 58% [5, 11, 12, 13, 14, 15]. The pathogenesis of RA-ILD is largely unknown [11, 16, 17, 18]. In practice, RA-ILD appears as chronic

inflammation of the lungs, where the lung parenchyma is progressively replaced by fibrotic tissue, which leads to death from respiratory failure.

These data indicate that although RA affects a relatively small percentage of the general population (around 1%), a significant subset of these patients develops a potentially serious pulmonary complication, highlighting the importance of early screening and diagnostic strategies for RA-associated interstitial lung disease.

Clinically, patients may initially present with nonspecific symptoms such as exertional dyspnea and dry cough, often attributed to other causes. By the time pulmonary symptoms prompt evaluation, significant fibrosis may already be established. HRCT scans reveal characteristic patterns of fibrosis, honeycombing, and traction bronchiectasis. Pulmonary function tests (PFTs) typically show restrictive ventilatory defects with reduced diffusing capacity for carbon monoxide (DLCO) [5].

As noted previously, HRCT remains the diagnostic gold standard, but repeated imaging for monitoring carries risks and costs. A routine use of HRCT for screening programs is not advisable for both the high costs to be sustained by the national health system (NHS) and the exposition to ionizing radiation of patients. PFTs, while useful, may fail to detect early functional impairment. These limitations highlight the unmet clinical need for accessible, non-invasive, and reliable screening methods capable of identifying RA-ILD at its earliest stages.

The detection of adventitious lung sounds, particularly velcro crackles, represents an underutilized clinical sign with potential to aid early diagnosis. Velcro crackles arise from the sudden opening of fibrotic alveoli during inspiration and correlate well with radiologic fibrosis extent [6, 7]. However, accurate detection requires trained clinicians and remains subjective.

The development of ILD in RA patients significantly worsens prognosis. Mortality rates are notably increased in RA-ILD patients, with median survival ranging from 3 [8, 9]to 8 [10] years following diagnosis, substantially shorter than in RA patients without lung involvement. The disease course can be heterogeneous; some patients experience rapid progression leading to respiratory failure, while others have a more indolent evolution. Risk factors for developing RA-ILD include older age at RA onset, smoking history, and the presence of anti-CCP antibodies that are strongly associated with RA-ILD in both sexes [3].

Significant attention has been devoted to the study of RA-ILD in recent years because it has been proved that the risk of developing ILD is much greater in RA patients than in non-RA patients (7.7% against 0.9% according to the study presented in [9].

The burden of RA-ILD extends beyond mortality. Progressive lung fibrosis leads to chronic respiratory symptoms including dyspnea, cough, and reduced exercise tolerance, significantly impairing quality of life (QOL) and increasing healthcare utilization. Hospitalizations due to respiratory complications and acute exacerbations contribute to rising costs and strain on healthcare systems.

2.2.2 Sjögren's Syndrome and Lung Complications

Sjögren's syndrome is a chronic autoimmune disorder primarily affecting exocrine glands, leading to sicca symptoms such as dry eyes and mouth. Beyond glandular involvement, systemic manifestations, including pulmonary complications, are observed in a significant subset of patients. Pulmonary involvement in Sjögren's syndrome is diverse, encompassing airway disease, lymphocytic interstitial pneumonia, and interstitial lung disease (ILD) [31].

Epidemiological studies report lung involvement in approximately 10–20% of Sjögren's patients [29]. Subclinical lung involvement is even more prevalent and frequently presents with evidence of small airway disease and airway inflammation. Overall, patients often exhibit both airway and interstitial abnormalities on imaging and histopathology. The most common airway manifestations include bronchiolitis and bronchiectasis, whereas interstitial lung pathologies observed in Sjögren's syndrome comprise nonspecific interstitial pneumonitis, usual interstitial pneumonitis, and lymphocytic interstitial pneumonitis. Additionally, patients with Sjögren's syndrome have an elevated risk of developing lymphoma [29]. The clinical presentation can be variable, often with insidious onset and nonspecific respiratory symptoms, making diagnosis challenging.

ILD in Sjögren's syndrome, though less common than in rheumatoid arthritis or systemic sclerosis, carries a significant risk of progressive lung impairment and reduced quality of life. Radiologic and histopathologic patterns overlap with those seen in other connective tissue diseases, including nonspecific interstitial pneumonia (NSIP) and usual interstitial pneumonia (UIP) [30].

Early recognition of lung involvement is essential to guide immunosuppressive therapy and monitor disease progression. However, the lack of sensitive, non-invasive screening tools limits timely diagnosis.

Auscultation for velcro crackles may aid clinical suspicion but requires significant expertise. Emerging technologies, such as electronic auscultation devices and automated lung sound analysis algorithms, may enhance early detection capabilities in this population, supporting more proactive pulmonary evaluation and management [7].

Pulmonary manifestations include airway disease, lymphocytic interstitial pneumonia, and ILD. The latter is particularly significant, contributing to morbidity and impaired pulmonary function.

2.3 Pulmonary Implications of Sars-CoV-2 and Vasculitides

The coronavirus disease 2019 (COVID-19) has placed an unprecedented burden on healthcare systems worldwide. One of the main challenges faced by physicians is

the monitoring of pauci-symptomatic patients at home, especially considering that hospital access is often limited or should be minimized. Early identification of interstitial pneumonia is crucial for improving survival in these patients. Recent studies on rheumatoid arthritis and interstitial lung disease (ILD) have demonstrated that pathological lung sounds can be automatically detected using dedicated algorithms. Exist preliminary work [33] aimed to assess whether similar algorithms could also identify abnormal lung sounds in patients with COVID-19 pneumonia. Specifically, the VECTOR software [33], originally developed for ILD, was applied to lung sound recordings from 28 patients admitted to the emergency department of the University Hospital of Modena (Italy) in December 2020 [33]. The performance of VECTOR was compared with imaging-based diagnostic modalities, including lung ultrasound, chest X-ray, and high-resolution computed tomography (HRCT), used as the gold standard. Remarkably, VECTOR achieved an overall diagnostic accuracy of 75%, despite the lack of specific training in lung auscultation for emergency staff and the absence of software parameter optimization for COVID-19 pneumonia. These findings support the potential of this approach as a novel tool for monitoring pulmonary involvement in pauci-symptomatic COVID-19 patients [33].

Severe acute respiratory syndrome coronavirus 2 (SARS-CoV-2), the causative agent of COVID-19, is an RNA virus with diverse clinical manifestations. Fever is the most frequently reported symptom (84–87% of cases), although hyposmia, hypogeusia, and diarrhea are also possible presentations [34, 35]. In early disease stages, fever may be absent, and patients can present with chills or isolated respiratory symptoms. While most cases are mild, a subset of patients develop pulmonary complications such as ground-glass opacities on chest imaging, progressing in severe cases to pneumonia, acute respiratory distress syndrome (ARDS), refractory hypoxemia, or even respiratory failure with multi-organ dysfunction. The appearance of extrapulmonary complications significantly increases the risk of sepsis, septic shock, and mortality. Evidence suggests that approximately 81% of patients experience mild disease, while only a minority develop severe pulmonary or systemic involvement [36, 37].

Chest X-ray remains an essential first-line imaging tool to differentiate COVID-19 from other conditions such as bacterial pneumonia, pleural effusion, or pulmonary edema. Typical COVID-19 findings include bilateral and peripheral hazy opacities. Reported sensitivity varies across studies but has been described as very high, reaching near 100% in early pandemic reports. Nevertheless, HRCT remains the most accurate diagnostic modality when combined with molecular testing, reducing false negatives [37, 38, 39].

The COVID-19 pandemic has also accelerated the development and adoption of telemedicine solutions, particularly for monitoring patients with mild disease at home or for those whose hospital access is limited. Despite this, two scenarios still require direct lung auscultation: critically ill intubated patients in intensive care, and pauci-symptomatic patients monitored at home. In the latter group, early detection of interstitial pneumonia is vital, as it often requires prompt hospital admission [40]. Recent studies have highlighted the prognostic value of auscultatory

findings in COVID-19. For example, Wang et al. investigated clinically relevant acoustic features in lung sounds of COVID-19 patients [41], while Zhang et al. successfully employed electronic stethoscopes to perform auscultation in physicians wearing personal protective equipment [42].

Regarding vasculitis ANCA-associated vasculitis (AAV) is a group of autoimmune diseases that mainly affect small blood vessels. The main types are granulomatosis with polyangiitis (GPA), microscopic polyangiitis (MPA), and eosinophilic granulomatosis with polyangiitis (EGPA) [43].

The lungs are often involved in these conditions, although the type of involvement can vary between diseases. In recent years, special attention has been given to ILD, which is more common in MPA (up to 45% of patients) than in GPA (around 23%) [43].

Among ANCA subtypes, anti-MPO antibodies are most frequently linked to ILD (46–71% of cases), while anti-PR3 antibodies are less often involved (0–29%) [43].

HRCT scans can detect interstitial changes in the lungs in as many as two-thirds of MPA patients, sometimes even in those without clear symptoms. The most frequent findings are ground-glass opacities (often related to diffuse alveolar hemorrhage), but reticulations, interlobular septal thickening, and honeycombing (a sign of lung fibrosis) are also reported [43].

ILD has a strong impact on both quality of life and survival, with mortality rates two to four times higher than in patients without ILD. The risk is especially increased in MPA patients with pulmonary fibrosis. At present, immunosuppressive therapy is also considered as a possible treatment option for ILD in this context [43].

In summary, although CTD-ILD, COVID-19 pneumonia, and AAV-associated ILD arise from different etiologies, autoimmune and infectious, they share a common clinical denominator represented by interstitial lung involvement and the possible presence of pathological inspiratory crackles. However, these conditions differ in terms of temporal evolution (chronic-progressive versus acute or subacute), severity, and clinical setting, ranging from outpatient monitoring to intensive care. Such variability may influence the acoustic characteristics of lung sounds, including amplitude, frequency content, and temporal distribution. Consequently, a lung sound acquisition system intended to be applicable across these scenarios must ensure sufficient bandwidth to capture high-frequency transient events and adequate sensitivity to detect subtle mechanical vibrations under heterogeneous clinical conditions. Recognizing both the shared features and the disease-specific differences is essential to inform the design requirements of the transducing element.

2.4 Early Diagnosis, Lung Auscultation and Automatic Analysis Technologies

Across chronic connective tissue diseases, coronavirus disease 2019 and vasculitis, pulmonary involvement is frequently insidious, with early symptoms that are subtle or absent. This latency in clinical manifestation complicates early diagnosis and delays initiation of treatment. Pulmonary complications represent a significant cause of morbidity and mortality [23] in patients with autoimmune diseases such as connective tissue diseases (CTDs) like rheumatoid arthritis (RA) and Sjögren's syndrome. Mortality rates are notably increased in RA-ILD patients, with median survival ranging from 3 [8, 9]to 8 [10] years following diagnosis, substantially shorter than in RA patients without lung involvement. Among these, interstitial lung disease (ILD) is the most clinically relevant and life threatening pulmonary manifestation, characterized by progressive fibrosis and impairment of lung function. Understanding the epidemiology and burden of these diseases is critical to appreciating the clinical impact and guiding research efforts towards early diagnosis and effective management.

High-resolution computed tomography (HRCT) scanning remains the gold standard for detecting interstitial lung disease, as discussed above, capable of identifying early fibrotic changes with high sensitivity. However, the practical limitations of HRCT, including cost, radiation exposure, and limited availability, restrict its routine use as a screening tool in asymptomatic or mildly symptomatic patients.

Pulmonary function tests (PFTs) are widely used for assessing lung involvement, but their sensitivity in detecting early disease is limited. PFTs measure the lungs' ability to hold air, to inhale and exhale, and to absorb oxygen through the use of a spirometer. Restrictive ventilatory defects and reduced diffusing capacity (DLCO) typically appear only after significant lung involvement. Variability in patient cooperation and effort can further confound PFT interpretation.

Numerous studies have validated the association between velcro crackles and early ILD. The presence of these crackles correlates well with fibrotic changes observed on HRCT, suggesting their utility as a non invasive biomarker for early pulmonary fibrosis.

Detection of velcro crackles through auscultation can precede radiologic and clinical signs, providing a critical time window for early intervention. However, the subtlety of these sounds and their similarity to other crackles or respiratory noises often challenge even experienced clinicians.

The limitations of traditional auscultation have driven innovation in lung sound acquisition and analysis. Electronic stethoscopes equipped with sensitive sensors and noise reduction technology improve sound quality and enable digital recording and storage. This facilitates off-line analysis and integration with automated diagnostic algorithms.

One promising approach involves the use of vibrating membrane sensors specifically designed to capture lung sounds with high fidelity. Coupled with machine learning and signal processing techniques, these systems can automatically detect and classify pathological lung sounds, including velcro crackles. Studies using these technologies report diagnostic accuracies of over 80% for identifying interstitial lung disease in patients with RA and connective tissue diseases [32].

As previously outlined, early detection of pulmonary involvement in connective tissue diseases is clinically crucial. From a technological standpoint, this requirement exposes important limitations in current auscultation systems.

Although electronic stethoscopes and automated lung sound analysis have been proposed to improve diagnostic reproducibility, most commercially available devices are characterized by limited bandwidth and suboptimal sensitivity. These constraints may hinder the detection of subtle acoustic components, particularly fine crackles associated with early interstitial changes.

Since machine learning-based diagnostic systems critically depend on the quality and spectral richness of the acquired signal, limitations at the sensor level may directly affect feature extraction and classification performance. However, while considerable research has focused on developing increasingly sophisticated algorithms, comparatively less attention has been devoted to optimizing the physical design of the acoustic sensor itself.

In particular, it remains insufficiently investigated whether improving bandwidth and sensitivity at the acquisition stage could enhance downstream automated diagnostic accuracy.

This PhD project specifically addresses this gap by focusing on the design and implementation of a vibrating membrane lung sound sensor. The central hypothesis is that a broader bandwidth and higher sensitivity will provide higher-fidelity acoustic data, enabling more robust feature extraction and supporting improved automated analysis

3 Electronic Stethoscope

3.1 Overview

Since its introduction by René Laennec in 1816, the stethoscope has become one of the most recognizable and enduring tools in medicine [77]. More than a diagnostic instrument, it has long represented a symbol of the physician's role, embodying the idea of careful listening to the patient's body. Despite the technological revolution in healthcare, the stethoscope has remained central to medical practice because of its simplicity, portability, and immediacy. However, the acoustic stethoscope relies heavily on the physician's hearing acuity and experience, which inevitably introduces subjectivity and variability [32]. Rather than representing a replacement of traditional auscultation, electronic stethoscopes and automated analysis systems should be viewed as complementary tools that augment clinical expertise. In the context of increasingly large clinical datasets, computational methods may enable preliminary screening and systematic characterization of lung sounds. However, experienced physicians remain essential to interpret, validate, and contextualize algorithmic outputs within the broader clinical picture. In this perspective, digital auscultation technologies serve not to substitute clinical judgment, but to enhance reproducibility, support early detection, and facilitate informed decision making.

While the stethoscope has historically represented a symbol of medical practice, modern national health systems (NHSs) face challenges that call for its technological evolution. Modern NHSs are called to tackle several challenges. The main issue encountered worldwide is represented by the lack of general doctors and physicians [46, 47, 48]. Indeed, large parts of the world also suffer from a shortage of advanced diagnostic tools, such as high resolution computed tomography (HRCT) and nuclear magnetic resonance (see for instance [49] and the references therein). Very high operating and maintenance costs complete the critical picture. Information and communication technology (ICT) is capable of pushing innovation in the medical field and can therefore play a fundamental role in tackling the challenges of NHSs [7]. Well-known fields of research are the so called eHealth and personalized medicine. eHealth or telemedicine can be defined as a set of ICT tools targeted at the remote fruition or application of medical services, so the main focus is on data communication. Personalized medicine considers the individual's genetic profile as a resource to devise very accurate drug prescriptions and clinical treatments [45]. Indeed, the design and development of new diagnostic tools represent a pioneering field of research.

Electronic stethoscopes can provide several advantages compared to their acoustic counterparts [50]. Both traditional and electronic stethoscopes rely on a sensing element that captures mechanical vibrations generated within the thorax. In conventional devices, these vibrations are transmitted through an acoustic pathway and ultimately processed by the physician's auditory and cognitive system. In contrast, electronic stethoscopes convert the detected mechanical vibrations into electrical signals through appropriate transducers. These signals can then be amplified, digitized, filtered, recorded, and further processed using computational methods.

Therefore, the fundamental difference does not lie in the presence of a sensing mechanism itself, but in the subsequent processing stage: traditional auscultation relies on biological signal processing performed by the human auditory system and clinical experience, whereas electronic auscultation enables electrical and digital signal processing, potentially allowing storage, sharing, quantitative analysis, and automated classification.

Modern sensors can be employed to take advantage of their technical properties, for instance in terms of sensitivity, dynamic range, and bandwidth. In particular, micro electro-mechanical systems (MEMS) and piezoelectric sensors are gaining wide commercial diffusion because of their appealing performance cost trade off. Signal processing onboard the electronic stethoscope discloses a huge potential. Several tasks can be programmed to support general doctors and physicians in clinical practice, such as environmental noise reduction, filtering, equalization, and detection of pathological lung sounds. Furthermore, data can be transmitted wirelessly to remote specialists, which is of paramount importance in telemedicine scenarios [45].

Within this field of application, Professor Fabrizio Pancaldi leads a heterogeneous team composed of professors, engineers, researchers, students, and clinical professionals, working on the development of an electronic stethoscope suitable for detecting pathological lung sounds and hence raising the diagnostic suspicion of RA-ILD and CTD-ILD. This device represents a promising and cost effective tool for ILD screening.

The diaphragm or vibrating membrane is a fundamental component of the stethoscope, since it couples the elastic wave propagating inside the human body with the sensor. It is well known that the technical properties of the diaphragm affect the performance of the stethoscope [51]. However, despite several theoretical and experimental studies on membrane vibration being available (see [52] and the references therein), the exact role of the diaphragm in a stethoscope for acoustic coupling is still mostly unclear [51]. A methodology for the quantitative comparison of different commercial diaphragms during heart auscultation is proposed in [51]. No design formulas or procedures are provided, but this thesis offers important conclusions. The main conclusions reported in that study are:

- No significant frequency filtering is evidenced by the diaphragms
- Stiff diaphragms with elastic suspension reveal better performance than stiff uniform membranes and bell type chestpieces

- These findings are applicable in the frequency range of heart sounds

Although a different behavior is not expected at higher frequencies and wider bandwidths, the study [51] does not provide definite indications for the acquisition of pathological lung sounds. The superiority of stiff diaphragms with elastic suspension is confirmed by the work [53], where two different suspensions are analyzed and compared. In particular, the extensible diaphragm can provide better performance than suspended diaphragms.

Recent advances include the design of a soft wearable stethoscope for continuous real-time auscultation and automated disease diagnosis [54]. The diaphragm in this case can be classified as bell-type, since the microphone is directly coupled to the skin. The soft enclosure yields an excellent skin contact, thus minimizing changes in acoustic impedance.

Building upon these results, this thesis introduces quantitative performance criteria for diaphragm evaluation in lung sound acquisition, focusing on bandwidth and sensitivity, which are critical for auscultation systems.

Standard stethoscope is shown in Figure 3.1.

Figure 3.1: Stethoscope assembly. Imaged taken from Littmann.

3.2 Applications

Acoustic information retrieved via digital stethoscopes or equivalent sensors has been employed for a wide range of applications, from continuous health monitoring, to automatic recognition and identification of cardiac patterns, to person identification algorithms [55, 56]. Recently, various studies have proved the effectiveness of electronic phonendoscopes and suitably developed software in the early detection of pulmonary fibrosis and interstitial lung diseases [57, 7].

Acoustics of stethoscopes and their performance as sensors have been studied for more than 50 years, with seminal articles dating as early as 1966 [58]. Subsequent investigations [59, 60] consolidated the knowledge that the usable information which can actually be retrieved through a stethoscope is limited to 2 kHz [61], even if Ertel and colleagues measured frequency responses of stethoscopes exceeding 3 kHz of bandwidth [58].

3.3 Relevance and Open Challenges

Electronic stethoscopes can democratize access to diagnostics thanks to their low cost, portability, and integration with telemedicine, enabling early detection and standardized auscultation. However, challenges remain, including sensitivity to environmental noise, lack of standardized acquisition protocols, and the need for large-scale clinical validation to ensure reliable diagnostic performance [45].

Another important limitation worth mentioning is the bandwidth of current electronic stethoscopes. Studies have shown that some pulmonary diseases, such as interstitial lung diseases (ILDs), generate characteristic acoustic signatures, velcro-like crackles, at frequencies higher than the resonance of most existing devices (see figures therein [32, 44]). In practice, the stethoscope behaves as a band-pass filter, attenuating these higher frequencies and thereby discarding clinically valuable information [32, 44]. This limitation underscores the need for a careful redesign of the diaphragm, or vibrating membrane, which plays a central role in acoustic coupling.

From an engineering perspective, the stethoscope diaphragm is more than a simple plastic film covering the chestpiece. While its detailed vibro-acoustic behavior depends on geometry, thickness, material properties, and suspension, for the purposes of this study it is modeled as a mass-spring-damper system mechanically coupled to the chest wall. This simplification captures the diaphragm's effective dynamic response, allowing a velocity-sensing approach to be implemented efficiently. In this framework, the mass, stiffness, and damping parameters represent the combined influence of the diaphragm's physical characteristics.

While a pressure-sensing diaphragm typically requires a resonance frequency well above the bandwidth of interest to achieve a stiffness-controlled, flat sensitivity response, such a highly rigid system reduces acoustic impedance matching with the

human body. As a result, mechanical coupling is diminished, and diagnostically relevant information, particularly at lower frequencies, may be significantly attenuated.

By contrast, a velocity-sensing diaphragm benefits from a resonance frequency located within the frequency range of interest, enhancing energy transfer from the skin to the sensor and improving sensitivity to subtle vibrational components. In principle, direct contact sensors, such as electrodynamic microphones or accelerometers attached to the skin, could provide an even more faithful measurement of skin vibrations by bypassing the mechanical-to-acoustic conversion step. However, in practical clinical applications, the combination of a membrane and a microphone remains widely used due to its familiar interface for clinicians, ease of handling, and robustness in capturing lung sounds. In this framework, the diaphragm resonance is intentionally tuned to balance sensitivity, bandwidth, and damping, ensuring effective acquisition of lung sounds while preserving mechanical coupling and signal fidelity across the clinically relevant spectrum.

Although this thesis focuses primarily on the physical design of the diaphragm, it is important to recognize the complementary role of artificial intelligence. Algorithms based on deep learning and spectrogram analysis have already shown encouraging results in classifying respiratory sounds such as crackles, wheezes, and rhonchi [32, 33, 7]. When coupled with hardware optimized for sensitivity and bandwidth, such algorithms could significantly expand the diagnostic potential of electronic stethoscopes. Ultimately, the combined advancement of hardware and software solutions will determine the success of these devices in real-world healthcare environments.

3.4 Needs Requirements and Constraints

In summary, as outlined in Chapter 2, the early detection of interstitial lung disease relies on the acquisition of subtle lung sounds characterized by relatively high-frequency components. These clinical requirements directly inform the technological design choices discussed in this chapter. Clinical studies reported in [32] indicate that diagnostically relevant information is concentrated around 500 Hz. Consequently, this work aims to design a vibrating membrane with an effective bandwidth approaching or exceeding this frequency range, while ensuring system sensitivity equal to or greater than the commercial benchmark used for this thesis that is Littmann Master Cardiology.

The diaphragm diameter of the custom membrane presented in this work is constrained to match that of the commercial version. This design choice allows straightforward integration onto the stethoscope chestpiece, enabling direct experimental comparison and facilitating preliminary clinical evaluations in collaboration with physicians.

An additional design constraint is industrial manufacturability. The proposed diaphragm must therefore be compatible with scalable and cost effective production processes, ensuring that the design can be realistically transferred from a laboratory prototype to a deployable medical device.

This thesis work addresses precisely this open challenge: simulating, designing, and testing a vibrating diaphragm for electronic stethoscopes with the goal of increasing both bandwidth and sensitivity, thereby enabling a more accurate identification of disease related lung sounds. The novelty of this thesis lies precisely in addressing the diaphragm as a key enabling technology for next generation auscultation. While much of the existing literature has focused on software-based approaches such as advanced filtering or machine learning classification, the hardware bottleneck imposed by current diaphragm designs has been largely overlooked (see for instance [32] and the references therein) . By simulating, dimensioning, designing, and experimentally testing a vibrating diaphragm specifically optimized for pulmonary auscultation, this work aims to close this gap. The central objective is to extend the bandwidth and improve the sensitivity of electronic stethoscopes, ensuring that clinically relevant high-frequency components, such as velcro-like crackles, are faithfully captured.

In practical terms, this effort can provide two major contributions. First, from a biomedical perspective, a more accurate detection of pathological lung sounds could enable earlier and more reliable screening of interstitial lung diseases and other respiratory conditions, potentially reducing dependence on expensive imaging techniques such as HRCT. Second, from an engineering standpoint, the development of design rules and experimental validation of diaphragm prototypes can serve as a methodological framework for future devices. In this sense, the thesis aspires not only to deliver a proof of concept but also to establish guidelines that may inspire subsequent research and industrial applications.

4 Validation Framework

4.1 System model

The system model investigated in this manuscript is represented in Figure 4.1 and is organized into four main components: the lung, human tissues, the vibrating membrane, and the microphone. The lung is modeled as the source of the signal of interest, namely the respiratory sound. In reality, the propagation of pulmonary sounds takes place through a highly heterogeneous medium composed of lung parenchyma, muscular layers, bone structures, pleura, and skin. For the purposes of this preliminary study, such anatomical complexity is simplified by assuming an equivalent homogeneous propagation medium. This abstraction is referred to, with a slight abuse of notation, as "human tissues" or "human body." The vibrating membrane constitutes the main focus of the investigation, while the microphone is modeled as the sink that collects the acoustic signal.

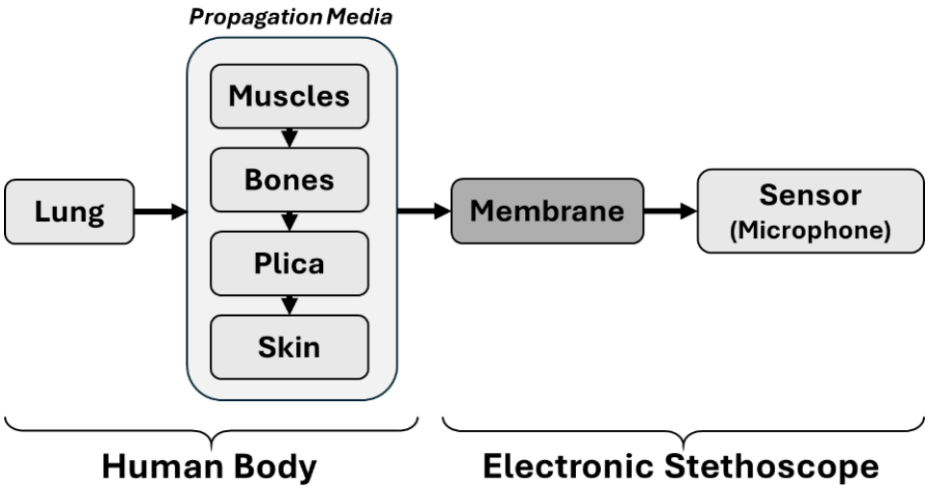

Figure 4.1: The model of the system under investigation is composed by lung, human tissues, vibrating membrane and microphone.

To accurately capture the complex mechanical behavior of human tissue, a detailed 3D mechanical model of the tissue and 3D mechanical model of the vibrating membrane is first developed. The results of these 3D models are then used to inform a simplified 1-D simulation of the entire system, providing realistic values for velocity

originated from lung signals, mass, stiffness, and damping. Later in the study, a separate 3D model of the entire system is used to validate the 1-D simulation results. This approach ensures that the simplified 1-D model maintains fidelity to the underlying tissue mechanics while remaining computationally tractable.

In a first attempt a one-dimensional (1D) approach has been adopted, meaning that the physical variables are assumed to depend on a single spatial dimension along the axis connecting the lung to the sensor. Although the time–frequency characteristics of pulmonary sounds are well documented in literature and provide clear theoretical requirements in terms of bandwidth and sensitivity, no consolidated design procedures are currently available for translating these requirements into diaphragm geometries optimized for velocity-based pulmonary auscultation. As a consequence, the relevant diaphragm design parameters, such as material properties, thickness, diameter, and mechanical damping, and their mutual interactions cannot be fully defined a priori. In this early design phase, the diaphragm design space is therefore explored using simplified models, which allow the identification of promising configurations before resorting to more detailed analyses. The adoption of a 1D model allows a substantial reduction in computational cost and simulation time compared to a direct multidimensional analysis, enabling the execution of multiple simulations in a reasonable timeframe. This facilitates the narrowing of the design space and supports a more efficient exploration of candidate solutions. Furthermore, the 1D framework provides a flexible environment for the rapid assessment of diverse scenarios, which in turn lays the foundation for the implementation of a well-structured design of experiments (DOE). Such an approach can quickly highlight whether a given solution is worth further investigation. Nevertheless, the simplifications inherent in a 1D model imply that certain effects cannot be captured, including the influence of the actual diaphragm geometry or the turbulence phenomena that arise in the acoustic chamber of a stethoscope. These effects are strongly dependent, on the detailed three-dimensional structured of the system. For this reason, the results obtained at this stage are intended as a preliminary assessment and are subsequently refined through three-dimensional simulations, as discussed in the following sections.

During this preliminary phase, two complementary simulation tools are employed. Simcenter Amesim is used to model the overall system depicted in Figure 4.1, taking advantage of its capabilities in multidisciplinary and multiphysics system-level simulations. Ansys is instead adopted to simulate both the 3D mechanical behavior of the biological tissues and to extract the parameters (mass spring damper) required for the setup of the system-level model. The simulations performed in Simcenter Amesim and Ansys are carried out independently and subsequently integrated at the modeling stage.

Following the 1D analysis, a three-dimensional model of the overall system is developed using COMSOL Multiphysics in order to refine the results and account for effects that cannot be captured within a monodimensional framework.

4.2 Simulations mono-dimensional

As discussed above the direct use of 3D simulations for the entire system is computationally expensive and time consuming, particularly when exploring a wide parameter space or performing multiple iterations for design optimization. Therefore, the validated 3D model of the biological tissue (not 3D model of the system shown in Figure 4.1) was employed to extract key parameters that could be incorporated into a simplified one-dimensional (1D) numerical model of the overall system. This 1D model retains the essential physics of wave propagation while significantly reducing computational cost, enabling efficient exploration of design variations and rapid simulation of different scenarios. In this way, the combination of high-fidelity 3D modeling and simplified 1D simulation provides a practical and effective framework for investigating wave propagation in human tissues and for supporting the subsequent design of the experimental and numerical studies presented in this work. The mono-dimensional simulation of the entire system, performed with Simcenter Amesim, is presented and discussed in sub-section 4.2.5. Before entering this section, it is useful to briefly introduce the main components of the 1D simulation:

- The signal generated by the lung, see sub-section 4.2.1
- The model of the biological tissues, see sub-section 4.2.2 - extract velocity from 3D model of the biological tissue (Ansys simulation)
- The model of the vibrating membrane, see sub-section 4.2.3 - extract mass-spring-damping coefficients from 3D model of the vibrating membrane (Ansys simulation)
- The model of the microphone., see sub-section 4.2.4

4.2.1 Lung as a signal source

Air and other fluids move from a region at higher pressure to a region at lower pressure [62]. As a consequence, a pressure difference between the atmosphere and the alveoli must be established to move air into and out the lung. Indeed, if no pressure difference is available, no airflow is possible. Under normal circumstances, inspiration occurs when the alveolar pressure falls below the atmospheric pressure. In the technical literature dealing with breathing mechanics (see for instance [62] and the references therein), atmospheric pressure is conventionally referred to as 0 cm H_2O, so a negative pressure between alveoli and atmosphere is necessary for inspiration. When the pressure difference is sufficient to overcome the load losses associated to the respiratory tract, air starts flowing into the lung. The force exerted by gases within the alveoli is called intra-alveolar (intrapulmonary) pressure, whereas the force exerted by gases in the pleural cavity is called intrapleural pressure (see Figure 4.2). Typically, intrapleural pressure is lower, or negative, with respect to intra-alveolar pressure. The difference between intrapleural and intra-alveolar

pressures is called transpulmonary pressure (see for instance [62] and the images and references therein).

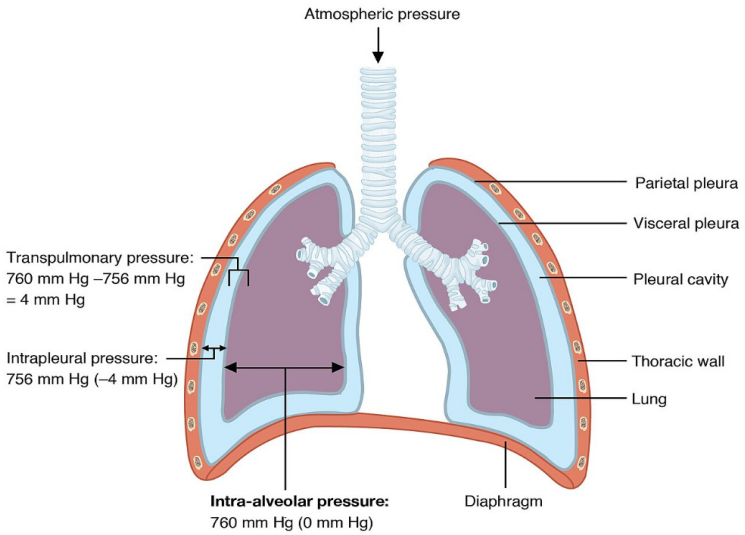

Figure 4.2: Intra-alveolar, intrapleural and transpulmonary pressure. Image taken from https://commons.wikimedia.org/wiki/File:2315_Intrapulmonary_and_Intrapleural_Pressure.jpg. No remix done.

During a forced expiration, the muscles devoted to expiration generate a positive intrapleural pressure up to +25 cm H_2O. The positive intrapleural pressure depends on how deep and forced is the expiration. In eupneic inspiration, the value of intrapleural pressure is -8 cm H_2O on the average [62]. Lung auscultation is performed by physicians through a stethoscope under deep breathing conditions, so we consider in our simulation an intrapleural pressure of 13 - 14 cm H_2O, i.e. about half of the maximum intrapleural pressure of +25 cm H_2O. A sinusoidal waveform is adopted for the intrapleural pressure as a first approximation, based on the observed shape of the physiological signal. This simplification facilitates frequency-domain analysis and reduces computational complexity, since some parameters of the human body model are frequency dependent. While this approach does not capture all features of real respiratory sounds, it provides a reasonable first step for model exploration. More complex waveforms may be considered in future studies to account for additional signal harmonics. We assume that the lung pressure is applied to a circular area of diameter 50 mm. The surface form is arbitrary at this stage of our research, however we have adopted it for its peculiar symmetry. The diameter has been selected similarly to the typical intercostal distance, since in the clinical practice the stethoscope is placed by physicians between two ribs; in fact, commercial diaphragms are of similar form and dimension. As a result, the amplitude of the sinusoidal waveform is 2.6 N. Based on the results reported in [44], the present study explored the frequency band $50 - 800$ Hz at steps of 50 Hz.

4.2.2 Model of the Human Body Tissue

To the best of our knowledge, there is currently no model in the technical literature capable of accurately predicting the propagation of mechanical waves within the human body. We initially addressed this challenge by deriving an analytical expression describing the propagation of a wave in a visc-oelastic medium and by numerically solving the corresponding partial differential equation. While this analytical approach provided useful insights into the general behavior of wave propagation, the resulting predictions did not demonstrate a satisfactory agreement with the experimental data reported in [44], indicating the need for a more comprehensive modeling framework.

To overcome this limitation, and because the velocity input is required for the mass-spring-damper simulation in the 1D Amesim model, this velocity was extracted from a targeted 3D simulation of the specific subsystem of interest (3D model of the biological tissue). We developed a three-dimensional (3D) model of the biological tissue to simulate wave propagation in the visco-elastic material (see Figure 4.4). The 3D simulations of the human body tissue incorporated a more detailed representation of the material properties and boundary conditions, allowing for a more accurate capture of the dynamic response. The results of these simulations showed a strong correlation with the apparent mass measurements documented in [44], thereby providing confidence in the validity of the 3D modeling approach of the biological tissue.

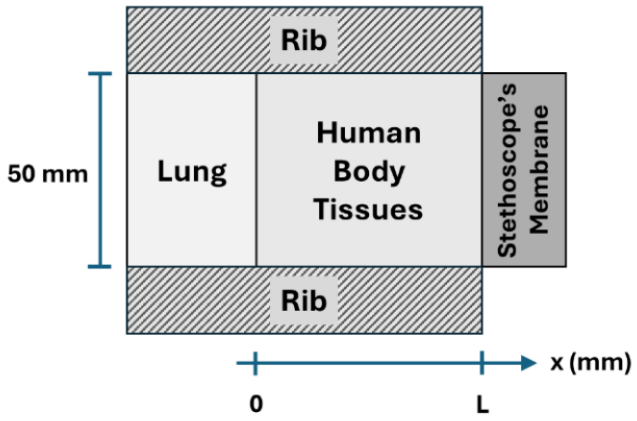

Figure 4.3: Cross section of the system considered for the human body tissues.

Mathematical model The propagation of mechanical vibrations from the lung to the sensor is approximated by a one-dimensional equivalent model. While the human body cannot be regarded as a beam in a mechanical sense, this abstraction is introduced to describe wave transmission along a preferential direction and to enable a tractable analytical formulation. Although biological tissues exhibit elastic behavior, the propagation of respiratory sounds through the thoracic wall is not

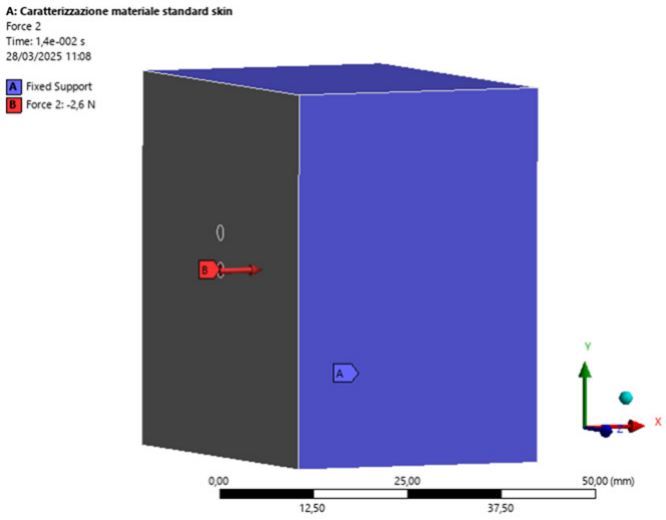

Figure 4.4: Simulation setup of the human body tissue for transient structural analysis in Ansys.

associated with global bending phenomena. Consequently, a classical beam interpretation implying flexural rigidity, bending moments, and shear forces is not physically representative of the underlying process. In the following, the governing equation is derived using a one-dimensional elastic wave formulation that is mathematically analogous to classical beam vibration theory. Here, the beam formalism is employed solely as a mathematical tool, while the resulting model should be interpreted as an effective description of longitudinal wave propagation along the lung to sensor direction [63].

$$\rho \cdot S \cdot \frac{\partial^2 u}{\partial t^2} = \frac{\partial N}{\partial x}, \tag{4.1}$$

where ρ denotes the material density, S is the cross-sectional area of the beam, u is the displacement along the longitudinal axis x, t is the temporal, x is the space variable and N represents the internal perturbing force acting along the x axis. By recalling the constitutive relations associated with the visco-elastic behavior of a Kelvin–Voigt material [64], the force N can be expressed as

$$N = S \cdot E \cdot \frac{\partial u}{\partial x} + S \cdot \eta \cdot \frac{\partial^2 u}{\partial x \partial t}, \tag{4.2}$$

where E is the Young modulus of the material and η is the viscosity coefficient of the material. We assume that density ρ, Young modulus E and viscosity η are independent by time and space. Substituting the Kelvin–Voigt constitutive law eq. (4.2) into the beam vibration equation (4.1) yields, after straightforward manipulations, the following mixed partial differential equation:

$$\rho \frac{\partial^2 u}{\partial t^2} = E \frac{\partial^2 u}{\partial x^2} + \eta \frac{\partial u^3}{\partial x^2 \partial t}. \tag{4.3}$$

The mixed partial differential equation (4.3) describing the propagation of a wave in a 1D visco-elastic material has been also mentioned by Caputo in [65]. Equation 4.3 has been firstly approached through the finite difference method implemented in Matlab environment.

In this framework, the system is driven by an input pressure. The input variable of our system is a pressure as discussed in Section 4.2.1, while the main dependent variable involved by equation (4.3) is the displacement $u\,(x,t)$. Initial values of the parameters were chosen in line with previous studies of biological tissues of human body [66, 67, 68, 69], namely density $\rho = 1000$ Kg/m^3, Young modulus $E = 4300$ Pa and viscosity $\eta = 10$ Pa·s. Boundary conditions are

$$u(0,t) = 0 \tag{4.4}$$

and

$$u(L,t) = 0, \tag{4.5}$$

i.e. the displacement is null at both sides of the human body tissue, this means that the displacement is constrained to vanish at both extremities of the propagation path. The imposed zero displacement boundary conditions do not imply that the thoracic wall is immobile in an absolute sense. Instead, the model is formulated in a reference frame attached to the body, and it describes small amplitude vibrational motions superimposed on the slow global movement associated with respiration. Under this assumption, the average displacement at the boundaries is set to zero, while the model captures only the relative mechanical vibrations responsible for sound transmission. In our reference system, $x = 0$ denotes the lung and $x = L$ denotes the skin. The distance L between the lung and the skin (in touch with the vibrating membrane) has been set to $L = 30$mm. The remaining initial conditions are

$$u\,(x,0) = \sin(\omega \cdot x) \tag{4.6}$$

and

$$\frac{\partial u\,(x,t)}{\partial t} = 0 \tag{4.7}$$

with $\omega = 2\pi f$. Equation (4.6) corresponds to the sinusoidal excitation originating at the lung, whereas equation (4.7) sets the initial velocity to zero, i.e. the system is initially at rest. We considered a grid consisting of 50 points in the displacement axis and 50 points in the time axis. The numerical solution indicated that the absolute magnitude of the displacement u increases monotonically as time progressed. However, this result does not represent a realistic behavior, as well as it does not fit the experimental data presented in [44]. In our opinion, this mismatch can be ascribed primarily to numerical instability of the solution due to the adopted finite difference

scheme and to the oversimplified boundary conditions, which do not adequately reflect the anatomical constraints that is the real scenario. Although the 1D model captures small-amplitude vibrations along the lung to skin direction and provides useful insights, it cannot represent certain important aspects of thoracic dynamics. In particular, in reality the thoracic wall is laterally constrained by the ribs but can oscillate between them, as illustrated in Figure 4.3. These multi-dimensional effects, combined with the heterogeneous tissue properties and the curved geometry of the chest, cannot be adequately described in a 1D framework. Moreover, features such as the three-dimensional configuration and positioning of the diaphragm compensation hole cannot be represented in one dimension. These limitations clearly indicate the need for a higher dimensional model to reproduce pulmonary sound propagation more faithfully. Consequently, a full three-dimensional (3D) finite element model was developed using Ansys, as illustrated in Figure 4.4 and described in Section 4.2.2.

3D Model The 3D model of the human body tissue has been studied and investigated in Ansys. A transient structural analysis module was carried out in order to determine the fundamental static parameters of the system, providing a first characterization of its mechanical response under time-dependent loading conditions. Detailed information on the solver, its governing equations, and the treatment of external stimuli is available in the official Ansys manuals and on the Ansys website.

Subsequently, a harmonic analysis was performed to refine and validate the model in the frequency domain, capturing both the resonant behavior and the frequency-dependent characteristics of the 3D structure (see Figure 4.4). This two-step approach, combining transient and harmonic analyses, allowed us not only to extract the essential static properties but also to obtain a comprehensive representation of the system dynamics across the relevant frequency range. Moreover, the frequency response obtained from the harmonic analysis enables direct comparison with experimental frequency-domain data, serving as a validation step and ensuring that the simulated response accurately reflects the dynamic behavior of the tissue-membrane assembly.

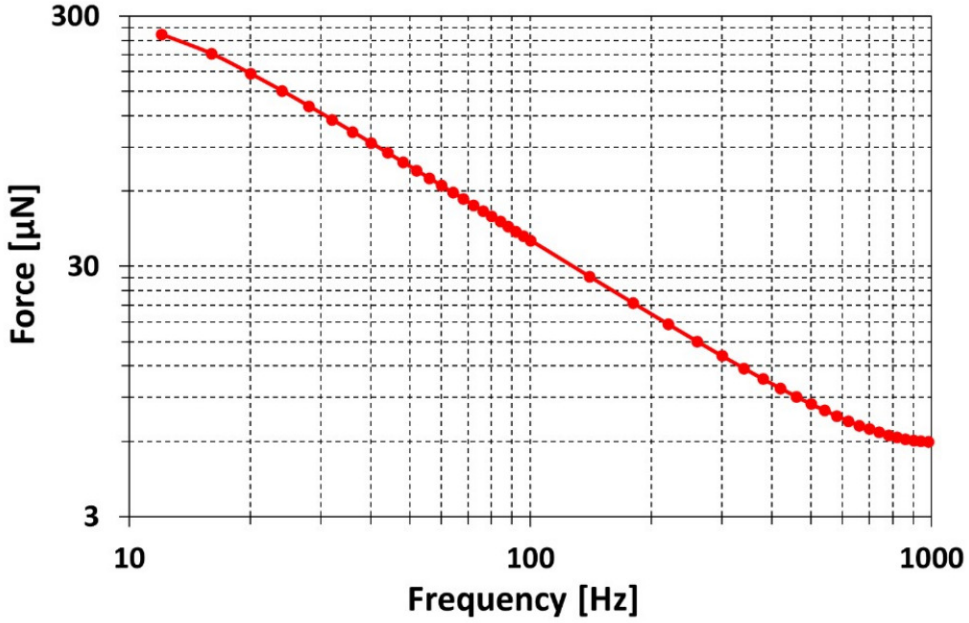

Figure 4.5: Smoothed experimental force extracted from experimental data of the work [44].

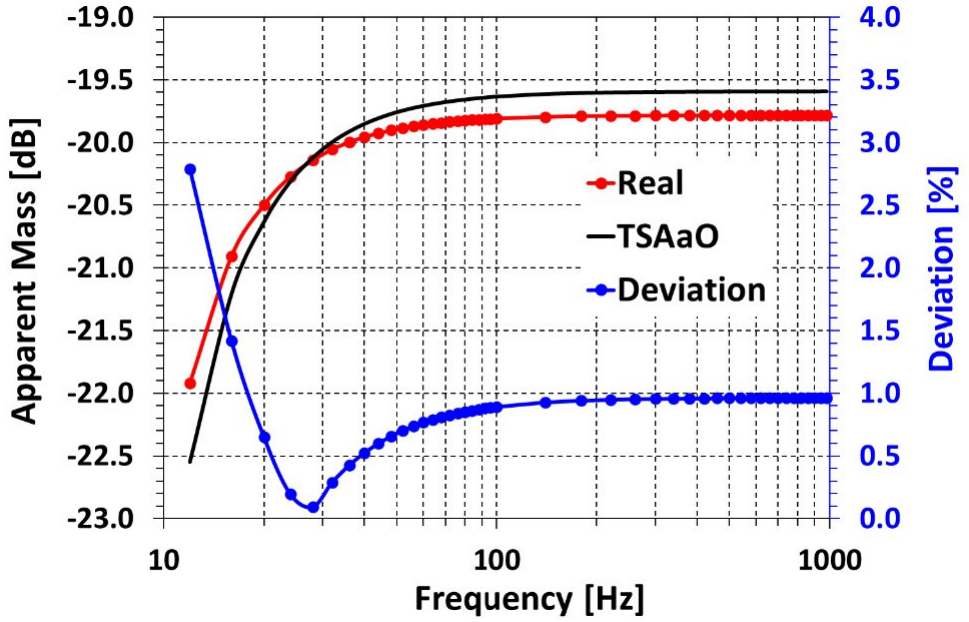

Figure 4.7: Smoothed apparent mass measured in [44] (solid red line) and apparent mass estimated by numerical simulation with TSAaO (solid black line). Percentage deviation is reported in blue solid line. The apparent mass is expressed in dB relative to 1 kg.

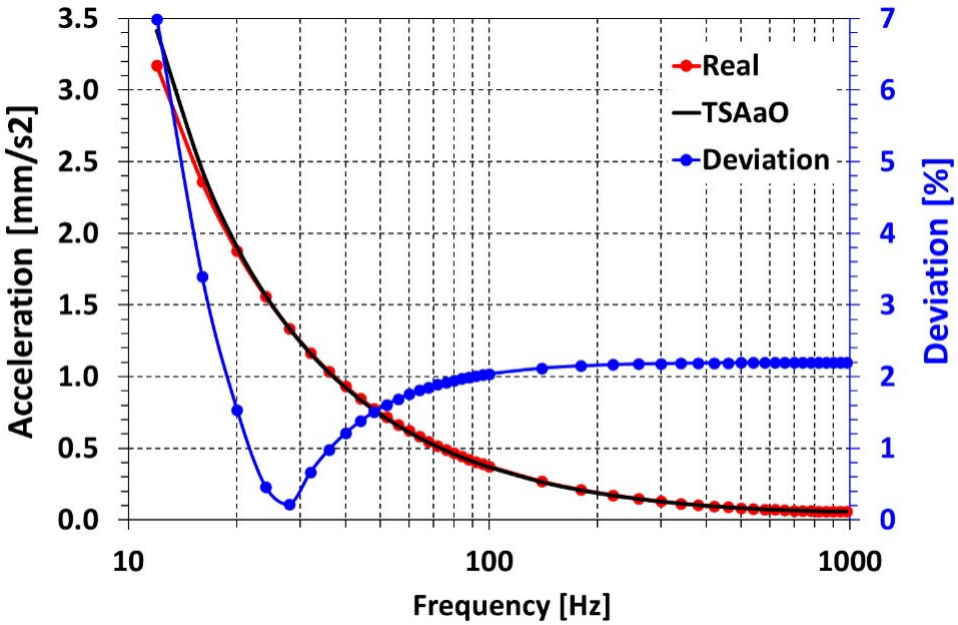

Figure 4.6: Smoothed acceleration measured in [44] (solid red line) and acceleration estimated by numerical simulation with TSAaO (solid black line). Percentage deviation is reported in blue solid line.

Force $F(f)$, acceleration $A(f)$ and apparent mass $H(f)$ as a function of frequency f have been extracted from the data set of [44]. The apparent mass $H(f)$ is directly related to the acoustic impedance of the system, providing information on how the tissue-membrane assembly responds to dynamic excitation across the frequency range. Therefore, these measurements are relevant for the characterization of the system dynamics and for setting up the simulation model.

Data smoothing has been performed to avoid overfitting; in particular, spline interpolation has been implemented in Matlab environment. In Ansys, a three-dimensional block with dimensions $50 \times 50 \times 35$ mm was designed in order to reproduce the geometry considered in the work [44]. This block was specifically designed to mimic the reference configuration and to ensure consistency with the experimental setup described in that work. The same geometry is schematically represented in Figure 4.3, which provides a cross sectional view of the human body tissue model adopted in our study. By defining this geometry within the simulation environment, we were able to establish a direct correspondence between the numerical domain and the physical configuration investigated experimentally, thus facilitating a more reliable comparison between simulated and measured results. The smoothed experimental force has been applied as tabular input to a circular area as described in Section 4.2.1. The simulation setup of the transient structural analysis is shown in Figure 4.4. The same load recorded from the hammer in [44] was applied in a simplified manner at five discrete points, each separated by 134 steps (smoothed experimental force). Subsequently, the material properties, namely

Young's modulus (E) and density (ρ), were varied to identify the combination that best reproduces the frequency response of acceleration and apparent mass observed in the reference tissue-material 25/human tissues of work [44]. The blue side represents fixed faces and the force $F(f)$ is applied to the circular area whose center is pointed by the red arrow. A mesh refinement was performed near the regions where the force was applied and the output was measured, in order to better capture the local phenomena. Assuming the smoothed experimental acceleration as target function, the Ansys transient structural analysis and design exploration toolbox have been exploited to devise the Young modulus and density of the model. The optimization process was carried out using the nonlinear programming by quadratic Lagrangian (NLPQL) algorithm. Following this stage, a harmonic analysis was performed in order to refine the mathematical representation of the material properties associated with the block. At this point, the experimental data reported in [44] have been used to extract a correction term for the acceleration response, after which the apparent mass was computed on the basis of this adjusted formulation.This procedure used the experimental data to calibrate the numerical model, ensuring that the simulation parameters accurately reflect the observed system behavior. The absolute magnitude of the smoothed experimental force $|F(f)|$, i.e. the input of the 3D model, is shown in Figure 4.5. The absolute magnitude of acceleration $|A(f)|$ and apparent mass $|H(f)|$ are shown in Figures 4.6 and 4.7, respectively. The red solid curves represent the smoothed experimental measurements, which are taken as the target dynamic behavior that the 3D numerical model is required to reproduce. The black solid curves correspond to the results obtained from the Transient Structural Analysis after Optimization (TSAaO), that is, the outcome of the calibrated simulation. The blue solid curves illustrate the percentage deviation between the experimental observations and the TSAaO numerical predictions. Quantitatively, this deviation amounts to approximately 2% for acceleration and around 1% for apparent mass. Such a close agreement demonstrates the capability of the developed 3D model to reliably approximate the experimental behavior, thereby making it suitable for subsequent use as a reference within the framework of the overall 1D numerical simulation.

The optimization procedure led to the identification of an effective Young's modulus of $E = 3x10^6$ Pa and $\rho = 70$ Kg/m^3. It is important to emphasize that these values differ considerably from the corresponding material parameters commonly reported in the technical literature [66, 67, 68, 69]. This apparent discrepancy can be explained by considering the measurement methodology employed in [44]. In that study, the apparent mass of the human body was obtained by means of an instrumented hammer equipped with both force and acceleration sensors, with the explicit aim of capturing the dynamic response of biological tissues to elastic wave propagation in the frequency range up to 10 kHz. In contrast, the majority of literature values for density and elastic module of soft tissues are obtained under quasi-static or static loading conditions, and therefore reflect material properties in a different physical regime. The optimized parameters derived through TSAaO

should thus be interpreted as effective dynamic parameters, specifically tailored to reproduce the frequency dependent mechanical behavior of biological tissues in the context of wave propagation, rather than as intrinsic static material constants.

In line with the scope of the present manuscript, which is to establish a coherent framework for the design of the vibrating membrane suitable for use in the electronic stethoscope, the Young's modulus and density obtained through TSAaO, namely $E = 3x10^6$ Pa and $\rho = 70$ Kg/m^3, are adopted within our simulation environment. Finally, since the vibrating membrane requires velocity as its excitation input, this variable has been computed from the acceleration output provided by the validated 3D model. The procedure ensures consistency between the material block simulations and the subsequent analysis of the vibrating diaphragm, which is described in detail in Section 4.2.3.

4.2.3 Model of the Vibrating Membrane

In order to design an optimized membrane for pulmonary sound auscultation, the analysis was initiated by taking as reference a widely used commercial model, namely the Littmann Master Cardiology. This choice was motivated by the availability of extensive experimental data already collected on this specific membrane, which provided a reliable basis for validating the numerical simulations. These simulations, once verified against the commercial reference, could then be used to support the development of an optimized diaphragm model.

The study of this reference system relied on both publicly available technical specifications [70] and additional properties derived from measurements. More specifically, the geometry was reconstructed on the basis of the manufacturer's datasheet as well as direct measurements, whereas the mechanical parameters, such as Young's modulus, Poisson's ratio, and density, were estimated from materials known to exhibit properties similar to those of the commercial diaphragm. The main geometrical features of the membrane are as follows: an external diameter of 50 mm, an effective vibrating diameter of 46 mm (corresponding to the free portion not constrained by the outer ring), and a thickness of 0.15 mm. In terms of materials, the outer ring is manufactured from neoprene rubber, while the central diaphragm is composed of E-glass epoxy.

Model validation was performed through a straightforward yet robust approach. A static load of 0.25 N was applied to a circular region concentric with the diaphragm, having a diameter of 25 mm, corresponding to the effective loading area of the membrane. The resulting maximum displacement was measured at the center of the diaphragm. The simulation setup is presented in Figure 4.8: the outer ring is shown in blue and was treated as fixed, since in practice it is mechanically coupled to the stethoscope chassis through its inner edge, while the loading area is highlighted in red.

Figure 4.8: Simulation setup in Ansys environment suitable to devise the parameters of the Littmann Master Cardiology commercial diaphragm.

A direct comparison between experimental displacement and numerical results obtained in the Ansys environment was then carried out. To achieve the closest possible agreement with the commercial diaphragm, selected model parameters were iteratively tuned. At the end of the calibration process, the discrepancy between measured and simulated displacements was reduced to less than 10%, confirming the adequacy of the developed model for its subsequent use in the optimization of the vibrating membrane. It should be noted that this procedure provides a static estimation of the spring constant and the corresponding compliance of the membrane surround. As such, it is strictly valid only for small displacements and at very low frequencies. Non-linear effects at larger amplitudes or higher frequencies, are not captured by this static calibration. Despite this limitation, the model provides a sufficient approximation for subsequent use in the preliminary optimization of the vibrating membrane.

The frequency response function (FRF) of the 3D model is derived from Ansys and then the half-power method [71] is used to estimate the damping factor c. The amplitude of the FRF of the simulated Littmann Master Cardiology diaphragm is shown in Figure 4.9. The damping coefficient ξ is given by

$$\xi = \frac{f_2 - f_1}{2f_n}, \tag{4.8}$$

where $f_n = 248$ Hz is the natural frequency of the membrane, $f_1 = 247.63$ Hz and $f_2 = 248.37$ Hz are the half power frequencies, around the natural frequency. The spring factor k has been estimated as

$$k = (f_n * 2\pi)^2 * m \tag{4.9}$$

Considering a mass $m = 3$ g, the spring factor results in $k = 7277$ N/m. Finally,

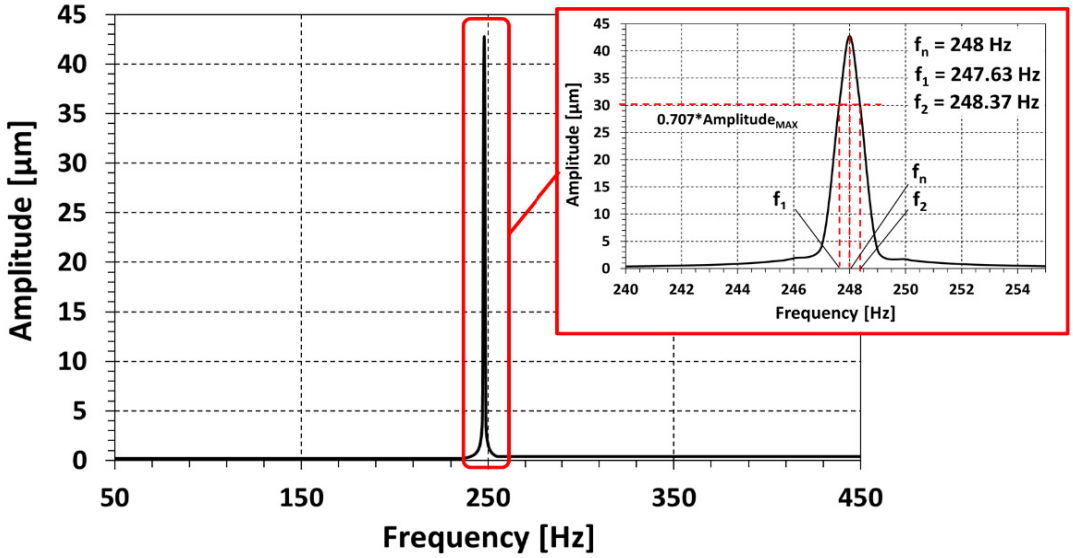

Figure 4.9: Amplitude of the FRF of the vibrating membrane obtained from harmonic analysis in Ansys. The technical characteristics, both publicly available and devised by experiments, of the Littmann Master Cardiology diaphragm have been considered in the analysis.

the damping factor c is then computed as

$$c = 2 * \xi * \sqrt{k * m} = 0.014\,\text{Ns/m}. \tag{4.10}$$

In the following, the vibrating membrane is modeled as a mass-spring-damper system with parameters m, k and c, respectively.

Characterization test by means Modal Shaker In this first attempt to estimate the damping coefficient c, we relied on the default values suggested by the software for the material properties of rubber. However, since rubber materials exhibit a wide variability in their parameters, a second attempt was conducted by first performing a frequency characterization of the Master Littmann Cardiology membrane shown in Figure 4.10, currently used in the electronic stethoscope (already developed by collaborator of professor F. Pancaldi) application, by means of a modal shaker. This allowed to obtain a graph with a shape similar of Figure 4.9, after which the value of c was adjusted accordingly (see Figure 4.13).

The test setup is configured as shown in Figure 4.11 and Figure 4.12, respectively with the block diagram and real setup. A Model Shop K2007E01 modal shaker was used, this is a mini modal shaker based on permanent magnet technology, with an integrated power amplifier. The base of the outer ring of the three membrane variants described previously was fixed to the shaker's base plate using beeswax. At the center of the vibrating diaphragm, a small square of reflective tape was applied

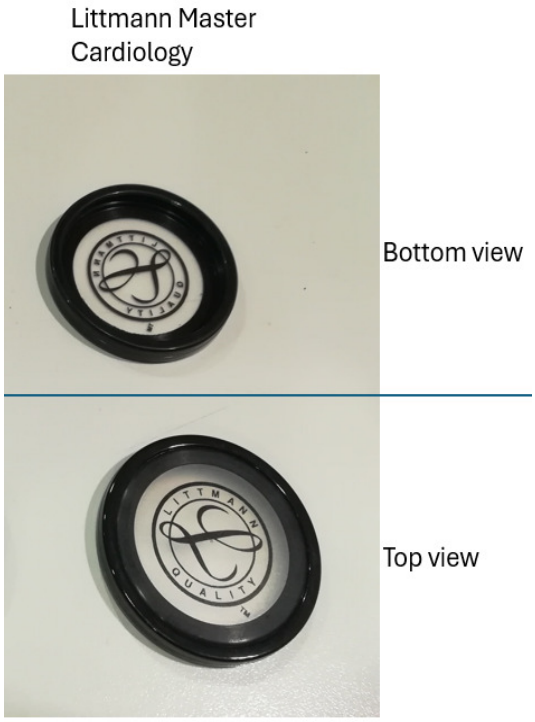

Figure 4.10: Littmann Master Cardiology membrane tested on Modal Shaker

to ensure optimal laser signal return from the Polytec OFV-505 sensor head. The system was controlled using a Polytec OFV-5000 controller.

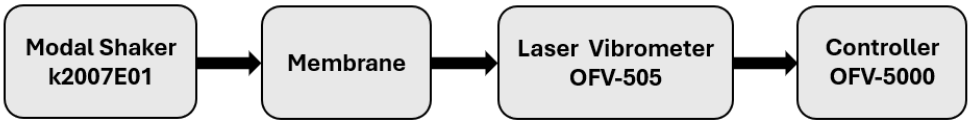

Figure 4.11: Block diagram of the test setup vibration analysis.

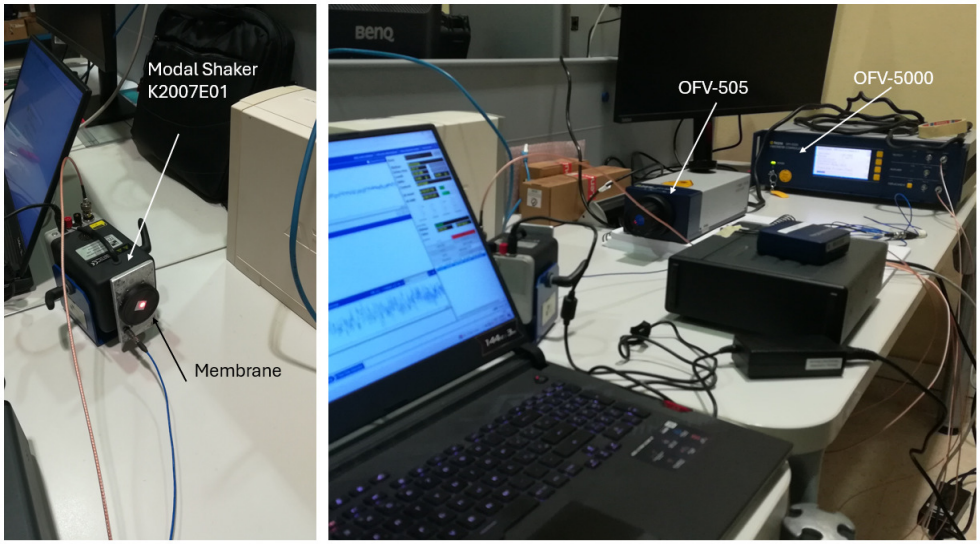

Figure 4.12: Test setup vibration analysis.

The system is excited using a flat Power Spectral Density (PSD) input within the frequency range from 100 Hz to 1000 Hz. The input level is adjusted in order to achieve 1g RMS acceleration. The use of random excitation allows the dynamic response of the diaphragm to be evaluated over the entire frequency band of interest within a single measurement, avoiding the need for multiple single-frequency tests. The results will be presented in the following paragraph and they are elaborated in Matlab.

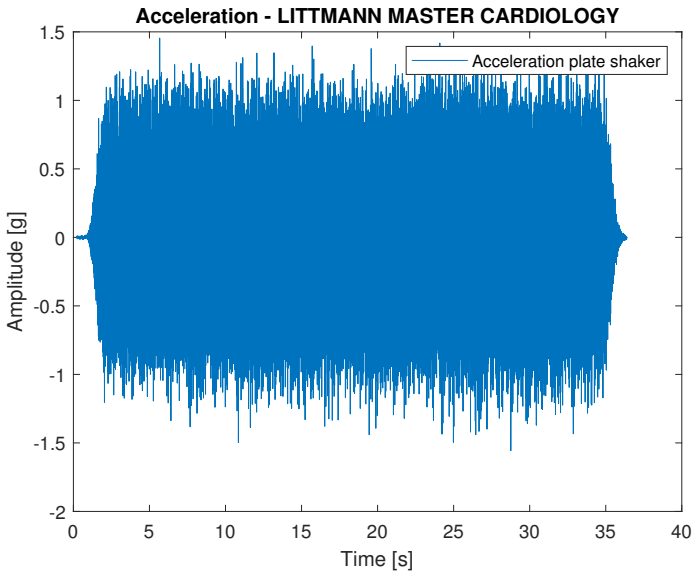

(a) Acceleration Input of the plate of the modal shaker K2007E01 for Littmann Master Cardiology membrane.

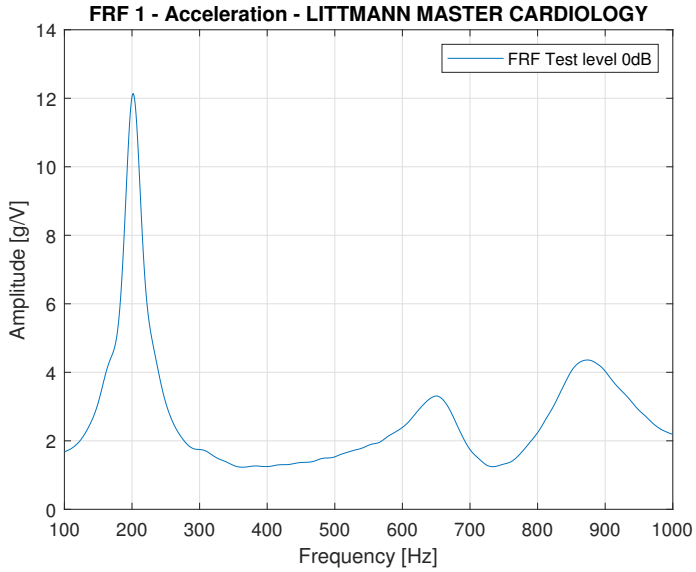

(b) Acceleration Output of the vibrating diaphragm Litmann Master Cardiology.

Figure 4.13: Littmann Master Cardiology characterization test. Acceleration Input of the modal shaker base and acceleration Output of the vibrating diaphragm.

Figure 4.13 shows the experimental modal shaker results obtained for the Littmann Master Cardiology membrane. The output signal represents acceleration; however, due to the absence of an impedance sensor in the setup, the resulting unit is expressed as acceleration over voltage [g/V]. Nonetheless, the resonance frequency can be directly extracted from these curves, and the real damping factor can be estimated

using the half-power bandwidth method for use in simulation models. There is a good agreement between the experimental and simulated data [45]. Based on these tests, the damping parameters were subsequently adjusted to achieve highly accurate simulation results.

From Figure 4.13a, it can be inferred that the resonance frequency is approximately 200 Hz, while the damping factor is estimated to be 0.13 Ns/m using the half-power bandwidth method [45]. The calculation of the damping factor is the same of that one shown in 4.9 using equations 4.8, 4.9 and 4.10.Compared with [44] reported resonance frequency of about 250 Hz, the discrepancy is expected and can be attributed to the statistical variability of both the product and the experimental setup.

Considering the simulated resonance frequency of 248 Hz [45] and the experiment 4.13b the percentage error is:

$$Error[\%] = \frac{\mid frequency_{simulated} - frequency_{real} \mid}{frequency_{simulated}} * 100 = \frac{\mid 248 - 200 \mid}{248} * 100 = 19\% \tag{4.11}$$

The percentage error is computed by normalizing the absolute difference between measured and theoretical frequencies to the theoretical value, which is taken as the reference baseline of the model. Considering the real frequency as the reference baseline the error is 24%.

while, considering the experiment [44], where the $frequency_{real}$ is equal to 250 Hz, the $Error[\%]$, using eq. 4.11, become less than 1%. In the adjustment process, I refer to the experiments I personally conducted, specifically those presented in Figure 4.13b, which demonstrate a resonance frequency of 200 Hz for the Littmann diaphragm.

For the damping factor, the error is larger, as rubber exhibits a wide variability in its mechanical properties (Ashby plots) also because the Littmann diaphragm is a multi material system with complex interactions, and the simulator's default damping value does not reflect the real sample. Specifically, the percentage error is $Error[\%] = \frac{|0.014-0.13|}{0.13} * 100 = 89\%$.

To strengthen the reliability of these extracted parameters, it would be advisable to test additional samples, thereby providing stronger statistical significance.

Using these parameters I adjusted the geometry of the vibrating membrane inside the simulations.

4.2.4 Model of the Microphone

The microphone employed in this study is the SPM0687LR5H-1, a device based on MEMS technology, operated here in a single-ended configuration. Its free-field

magnitude and phase responses were extracted from the manufacturer's datasheet [72] and are reported in Figure 4.14. According to the specifications, the lower cutoff frequency is defined at -3dB at 10Hz, while the response remains essentially flat (unitary gain) up to several kilohertz, thus fully covering the frequency range of interest for this work.

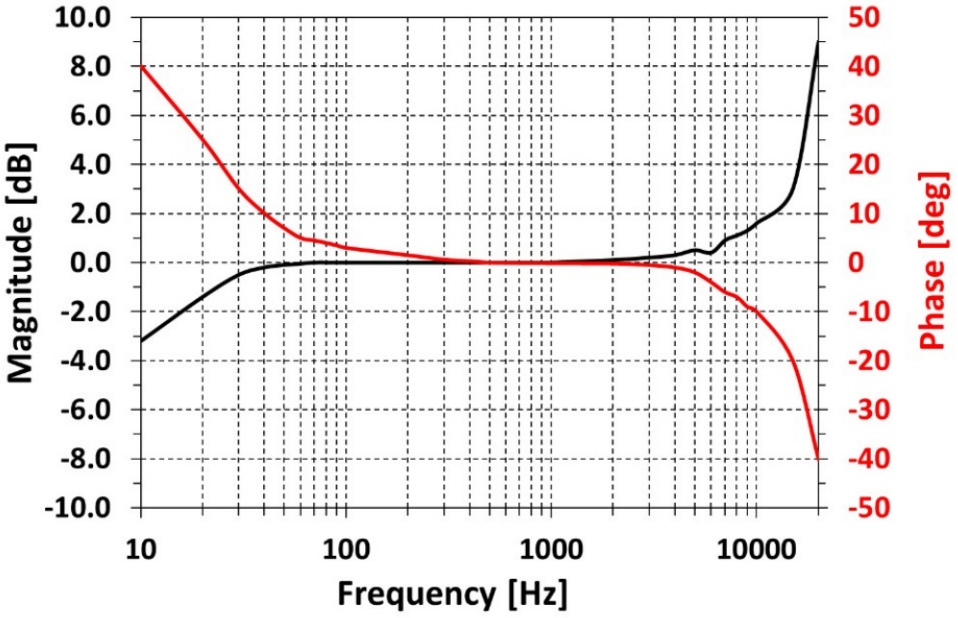

Figure 4.14: Free field magnitude and phase response of the microphone SPM0687LR5H-1. Data have been extracted from the datasheets of the component [72].

In the simulation environment, the microphone is represented as a sensing element composed of a pneumatic chamber subjected to an absolute reference pressure of 1.013 bar. For modeling purposes, the gain is assumed to be unitary (in linear scale) across the entire frequency band of $50 - 2000$ Hz as it is possible to see in the Figure 4.14. Consequently, no lower cutoff is included in the model, which allows for a simplified yet sufficiently accurate representation of the sensor within the operational bandwidth relevant to our application.

This modeling choice is justified by the fact that the main phenomena under investigation occur within the $50 - 2000$ Hz range, where the sensor response is effectively flat. Neglecting the low-frequency cutoff below 10Hz does not introduce a significant error in the interpretation of the results, since such frequencies are not relevant for auscultation-related applications. On the other hand, it must be acknowledged that this approximation does not account for certain real-world behaviors of MEMS microphones, such as phase distortions at very low frequencies, thermal noise contributions, or sensitivity drifts due to manufacturing tolerances and environmental conditions.

Nevertheless, this level of simplification is common in first-order simulation studies, as it ensures computational tractability and isolates the primary effects of interest without introducing unnecessary complexity. More refined models could include the full manufacturer response curve, as well as stochastic variations in sensitivity and noise, to improve the accuracy and statistical robustness of the analysis. However, for the scope of this work, the adopted model provides a reasonable balance between fidelity and efficiency, while remaining consistent with the objectives of the study.

4.2.5 Simulation 1D of the entire system by using Amesim Simcenter

The lung and the human body were modeled in Ansys, following the methodologies described in Sections 4.2.1 and 4.2.2, respectively. The human body was represented as a block of tissue with dimensions $50 \times 50 \times 35$ mm, constrained along the external contour which, in principle, corresponds to the mechanical support provided by the rib cage. Sinusoidal forces at different frequencies were applied to one face of the block, while the corresponding directional velocities along the main axis were measured on the opposite face. This setup allowed the extraction of a frequency-dependent mechanical transfer function.

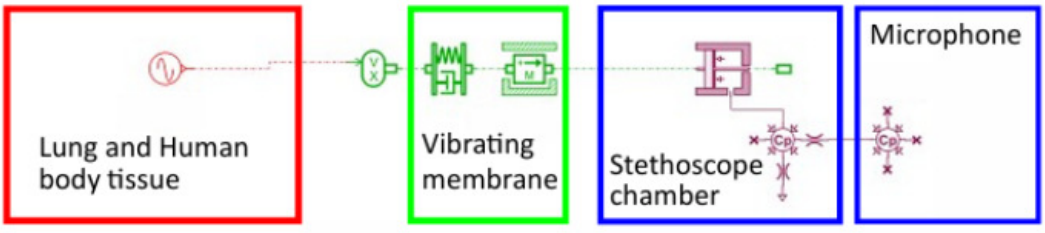

Figure 4.15: Simcenter Amesim scheme of the system composed by lung, human body tissue, vibrating membrane and microphone.

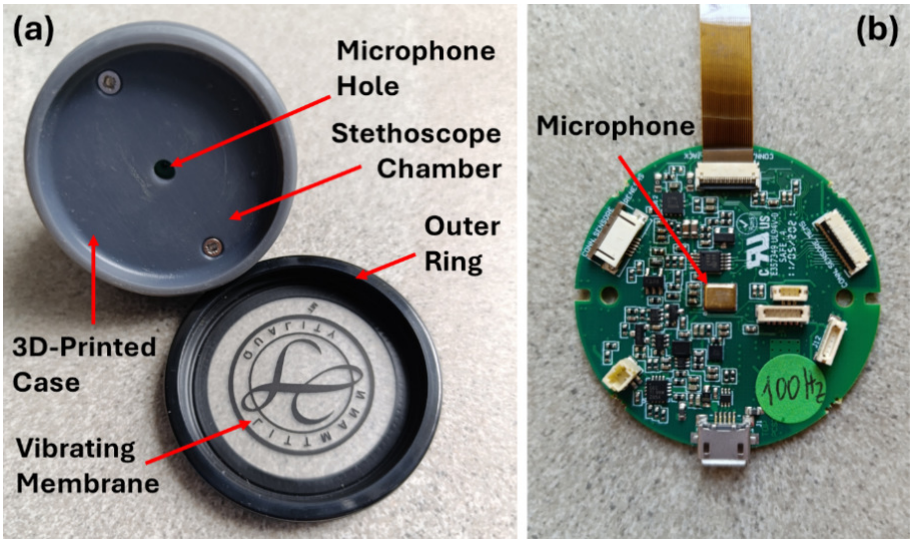

Figure 4.16: Disassembled prototype of electronic stethoscope: (a) commercial diaphragm detached from the 3D-printed case showing the pneumatic acoustic chamber and the hole for the MEMS microphone; (b) electronic board with the MEMS microphone aligned with the hole in the pneumatic acoustic chamber. This prototype was already made by professor F Pancaldi and different collaborators. This was the starting point.

The Ansys sub-model was then integrated into Simcenter Amesim, as illustrated in Figure 4.15. In this framework, the results of the Ansys TSAaO simulations serve as input excitation for the vibrating membrane model implemented in Simcenter Amesim. The vibrating membrane itself is represented as a classical mass – spring – damper system, with coefficients derived according to the procedure detailed in Section 4.2.3. To ensure consistency with the experimental setup, several parameters were extracted from the 3D cad model of the electronic stethoscope prototype. The main structural components considered in the simulation are highlighted in Figure 4.16, namely the diaphragm, the outer ring with snap-fit connection to the chassis, the pneumatic acoustic chamber, and the microphone mounted on the electronic board. Although the microphone could, in principle, also be modeled as a mass–spring–damper system, within Simcenter Amesim it is represented as a "pure" pressure sensor. This choice is motivated by two considerations. First, the focus of this work lies in optimizing the performance of the vibrating membrane, while the commercial microphone essentially functions as a pressure detector, with well-characterized and nearly flat amplitude and phase responses across the band of interest (see Figure 4.14). Second, duplicating the modeling of the microphone would increase the complexity of the simulation framework without bringing significant improvements in accuracy, and might even introduce additional sources of uncertainty due to parameter estimation. Thus, the simplified modeling strategy provides a reasonable balance between computational efficiency and fidelity, while remaining fully consistent with the practical objectives of this study.

In order to validate our simulated system, we consider the commercial vibrating membrane of the Littmann Master Cardiology stethoscope. The corresponding parameters were derived as described in Section 4.2.3. The following results are obtained from simulations performed in Simcenter Amesim. To assess the consistency of the model, the resulting bandwidth values were evaluated using two different approaches: first, by analyzing the peak-to-peak force response in the frequency domain, expressed in decibels and normalized with respect to a reference force of 1 N (see Figure 4.17), and second, by examining the pressure response recorded at the microphone node in Simcenter Amesim (see Figure 4.18). Both approaches yield frequency responses that are in good agreement with the experimental data reported in [44], indicating that the simulated model accurately captures the dynamic behavior of the vibrating membrane. Comparing these two metrics provides additional confidence in the simulation framework, as it demonstrates that both the mechanical excitation of the membrane and the subsequent acoustic response measured by the microphone are consistently represented. This dual validation approach is particularly important for ensuring that the model can reliably predict the membrane's performance in practical applications, such as electronic stethoscope prototypes.

The -3dB bandwidth of the system before the sensor is approximately $200-250$Hz; this result has a good match with our findings presented in the works [73, 32, 44].

The pressure detected at the microphone as a function of frequency $p^{mic}_{pk-pk}(f)$ is reported in Figure 4.18. In order to carry out the measurements, we mounted the Littmann Master Cardiology diaphragm together with the MEMS analog microphone SPM0687LR5H-1 [72] on the prototype of the electronic stethoscope (see Figure 4.16). The polarization circuit of the microphone was designed by the collaborator of professor F. Pancaldi to include a first-order high-pass filter with a -3 dB cutoff frequency of 120 Hz, in order to attenuate heart sounds and suppress most low-frequency artifacts, as suggested in our previous works [73, 32]. Preliminary experimental tests were essential to design the conditioning circuit of the microphone so as to avoid saturation of the amplification chain. To this aim, Pancaldi's group measured the maximum output voltage of the microphone's polarization network during outpatient examinations of volunteers at the University Hospital of Modena (Italy). The highest recorded voltage corresponded to an input pressure at the microphone of approximately 3 Pa peak-to-peak, observed during deep inspiration and expiration. Unfortunately, it was not experimentally investigated in detail the frequency response of the subsystem composed of the vibrating diaphragm, the analog microphone, and the polarization circuit. Nevertheless, it is worth emphasizing that the experimental pressure recorded at the microphone input corresponds to about half of the full-scale value predicted by the simulations (see Figure 4.18). This agreement allows to reasonably claim a satisfactory match between numerical predictions and experimental observations, thus supporting the validity of the adopted modeling approach [44].

Finally, the absolute magnitude of the frequency response function of the overall system $H_p(f)$ which includes the contribution of the lungs, the human tissues, and

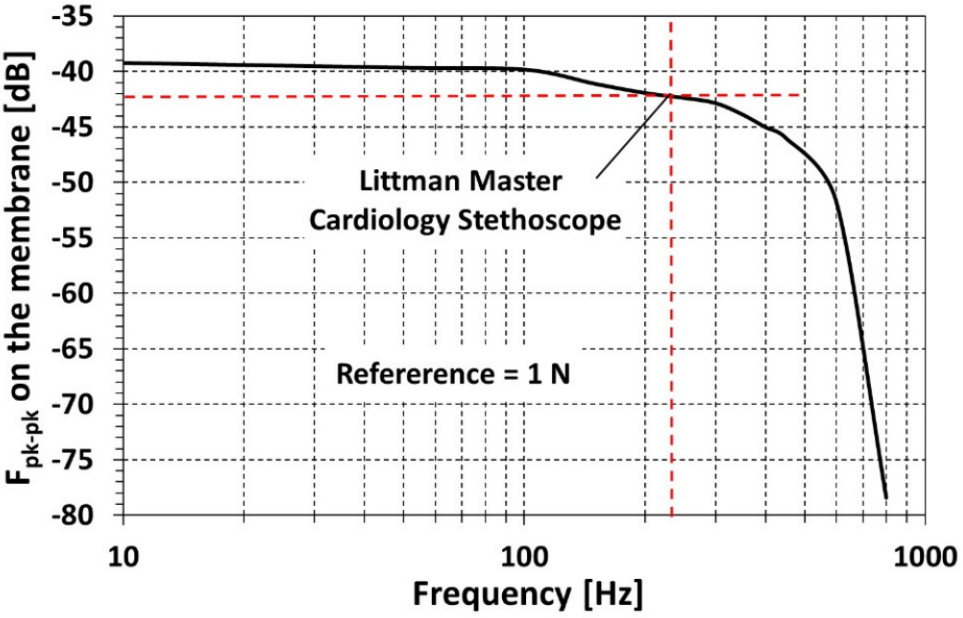

Figure 4.17: Peak-to-peak force on the membrane in dB referring to 1N as a function of frequency. The commercial vibrating membrane of the Littmann Master Cardiology stethoscope is considered in the simulation. The resonance frequency of the Littmann Master Cardiology diaphragm was evaluated through simulation over the frequency range 10–1000 Hz. This range was chosen for convenience in the analysis and does not influence the intrinsic resonance of the diaphragm, which is a property of its geometry and material.

the vibrating diaphragm, can be formally defined as follows:

$$H_p(f) = \frac{p^{mic}_{pk-pk}(f)}{p^{lung}_{pk-pk}(f)} \tag{4.12}$$

where $p^{lung}_{pk-pk}(f)$ is the peak-to-peak pressure at the lung (see Section 4.2.1) and $p^{mic}_{pk-pk}(f)$ is the peak-to-peak pressure measured at the microphone. The absolute magnitude of the frequency response function $H_p(f)$ is shown in Figure 4.19. The stimulus applied was the same of Figure 4.17 and 4.18 that is a velocity simulated as explained in the previous sections. The low-pass behavior of the system becomes evident at frequencies around $700 - 800$Hz as experimentally observed in the works [73, 32, 44].

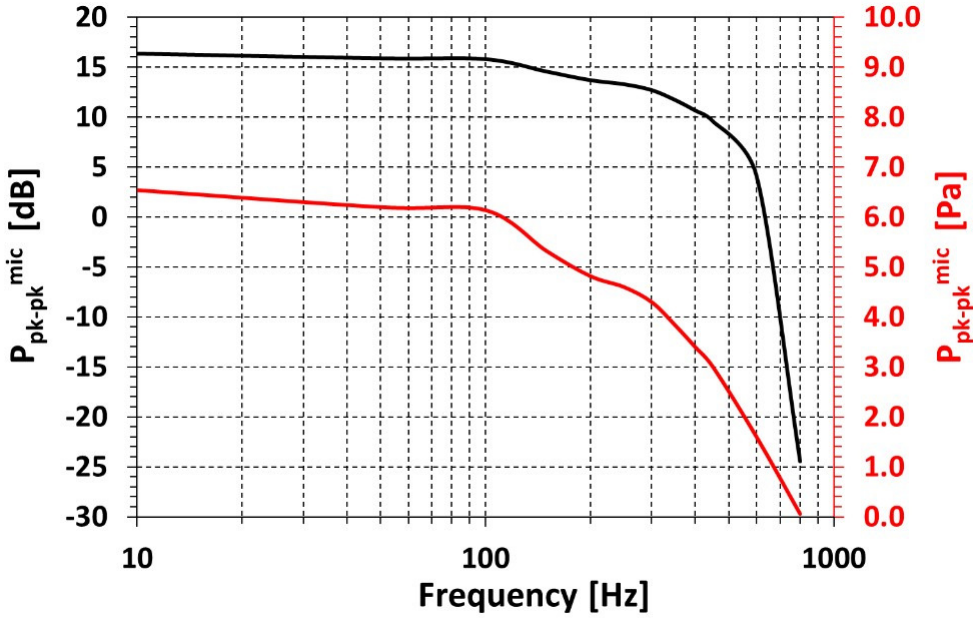

Figure 4.18: Peak-to-peak pressure at the microphone in dB relative to 1 Pa (left black vertical axis) and in Pa (right red vertical axis) as a function of frequency. The resonance frequency of the Littmann Master Cardiology diaphragm was evaluated through simulation over the frequency range 10–1000 Hz. This range was chosen for convenience in the analysis and does not influence the intrinsic resonance of the diaphragm, which is a property of its geometry and material.

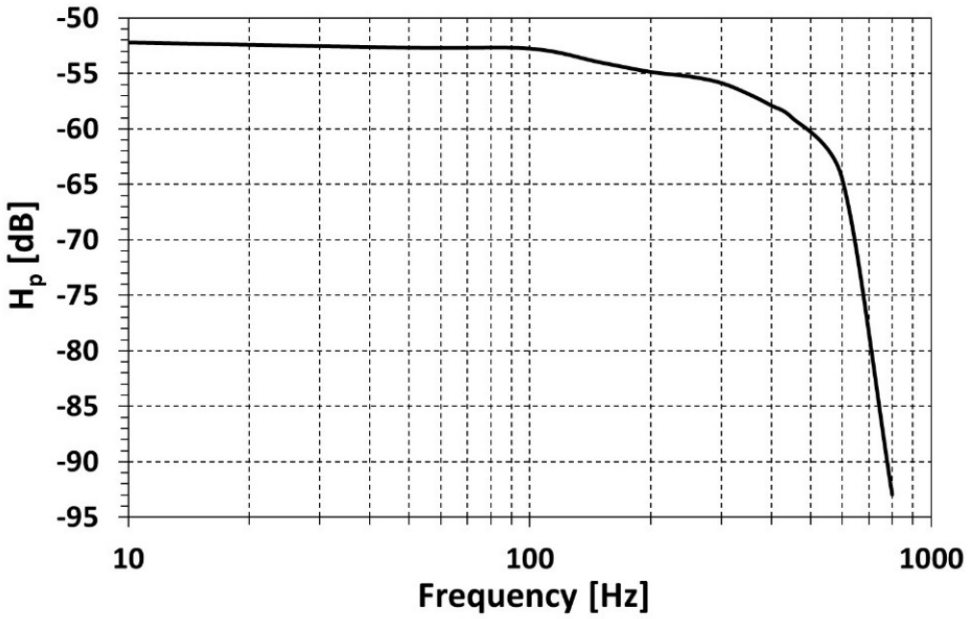

Figure 4.19: Frequency response function of the whole system $H_p(f)$ including the Littmann Master Cardiology diaphragm and the MEMS analogical microphone SPM0687LR5H-1 [72].

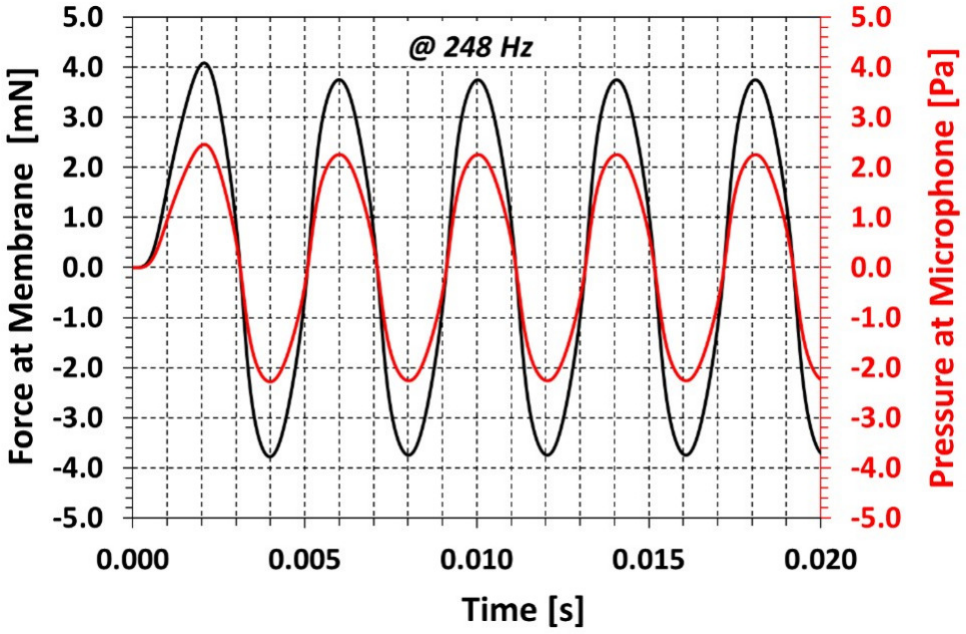

Figure 4.20: Example of time domain simulation in Amesim environment. A sine wave at the frequency of 248 Hz is applied to the human body tissue. After an initial transient, the force applied to the diaphragm is a pure sine wave at the same frequency. The pressure at the microphone is characterized by the same fundamental frequency of 248 Hz, but the waveform is not a pure sine wave because of the elasticity of the vibrating membrane and the propagation of the signal in the pneumatic acoustic chamber of the stethoscope.

In agreement with the expected behavior, the shapes of the force on the membrane, pressure on the microphone and frequency response function of the whole system are very similar, as evidenced by Figures 4.17, 4.18 and 4.19, respectively. Absolute magnitudes in dB differ because they correspond to distinct physical quantities, namely force, pressure, and pressure ratios. The -3 dB bandwidth is approximately 250 Hz, with minor deviations introduced by losses in the system components. Since the MEMS microphone SPM0687LR5H-1 used in the electronic stethoscope prototype exhibits a bandwidth much larger than 250 Hz (see Figure 4.14), the overall system bandwidth is primarily constrained by the acoustic properties of human body tissues and, potentially, by the mechanical characteristics of the diaphragm.

An example of a time-domain Amesim simulation is presented in Figure 4.20. In this case, the excitation applied to the human body tissue is a sinusoidal signal at the resonance frequency of the vibrating membrane, namely 248 Hz (see Figure 4.9). After the initial transient response, the force transmitted to the diaphragm stabilizes into a steady-state sinusoidal waveform at the same frequency, with a peak amplitude of 3.7 mN. Correspondingly, the acoustic pressure measured at the microphone also exhibits the same fundamental frequency of 248 Hz, with a nearly constant peak amplitude of 2.2 Pa. Nevertheless, the resulting pressure waveform

cannot be considered a pure sine wave, as it is influenced by the elastic behavior of the vibrating membrane as well as by the propagation phenomena occurring within the pneumatic acoustic chamber of the stethoscope. These effects introduce slight distortions in the signal, highlighting the role of both mechanical and acoustic dynamics in shaping the response of the system.

4.3 Two and three dimensional simulations

Once the one-dimensional model had been validated, the analysis was extended by taking advantage of the benefits offered by 1D simulations, namely their efficiency and capability to provide rapid insight into the system behavior. These results were subsequently refined through three-dimensional (3D) simulations based on the finite element method (FEM), which enable a more detailed and physically accurate description of the coupled mechanical–acoustic phenomena. The 3D simulations of the entire system were performed using Comsol Multiphysics.

To validate the 3D model, the starting point was the simulation of the Littmann Master Cardiology diaphragm in isolation. This step was essential to correctly define the material parameters, such as the damping coefficient of the rubber of the membrane, which had previously been characterized through experimental tests (see Section 4.2.3). After this calibration stage, an axisymmetric two-dimensional (2D) model of the complete system, comprising the diaphragm and the acoustic chamber of the stethoscope, was developed. The purpose of this step was to evaluate the interaction between the mechanical and acoustic domains and to identify possible coupling effects between these two physical subsystems.

In the mechanical domain, the model included the vibrating diaphragm, the suspension connecting the diaphragm to the outer ring, the outer ring itself, and the rear wall of the stethoscope (see Figure 4.16, where the rear wall of the stethoscope is on the same plane of the microphone hole and indicated by “3D printed case” arrow). Together, these elements form the structural boundaries of the acoustic chamber. The acoustic domain, in turn, was used to model the volume of air enclosed within the stethoscope, representing the acoustic chamber. The two domains were then coupled, allowing a mechanical excitation applied to the diaphragm to be consistently translated into an acoustic pressure output through deformation of the air volume.

Furthermore, to reproduce the operating conditions of the electronic stethoscope prototype, a small vent hole was incorporated in the model. This feature reflects the vent present in the commercial MEMS microphone adopted in the prototype. In the simulation, the vent was modeled as a narrow passage connected to the external atmosphere, terminated with a spherical wave radiation boundary condition. This implementation effectively avoids spurious reflections, which would otherwise occur in a closed computational domain but are absent in real-world conditions due to

radiation into open air. To account for internal reflections within the stethoscope chamber, boundary coupling conditions were implemented between the acoustic and mechanical domains.

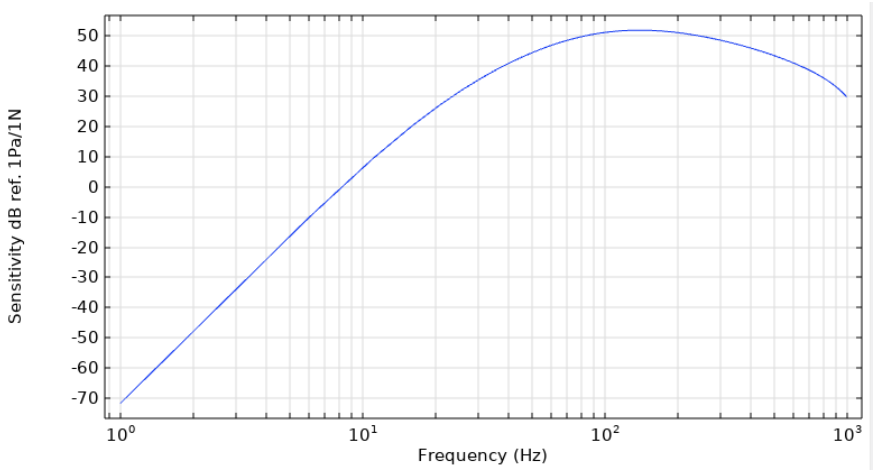

Figure 4.21: COMSOL sensitivity result of Littmann Master cardiology membrane. Bandwidth at -3dB is around 300Hz and maximum sensitivity is 52dB.

To compute the sensitivity curve, the acoustic pressure was evaluated at the microphone location. Since the pressure field inside the chamber is nearly uniform (see Figure 4.22), the exact position of the microphone is not critical (see Figure 4.22). The sensitivity was obtained by dividing the computed pressure by the force applied to the diaphragm, following the same methodology described in [44] and with very similar results. Finally, to account for human auditory perception, the simulated output was filtered using an A-weighting function. The resulting frequency response is reported in Figure 5.13. The deformation of the membrane is shown in Figure 4.23.

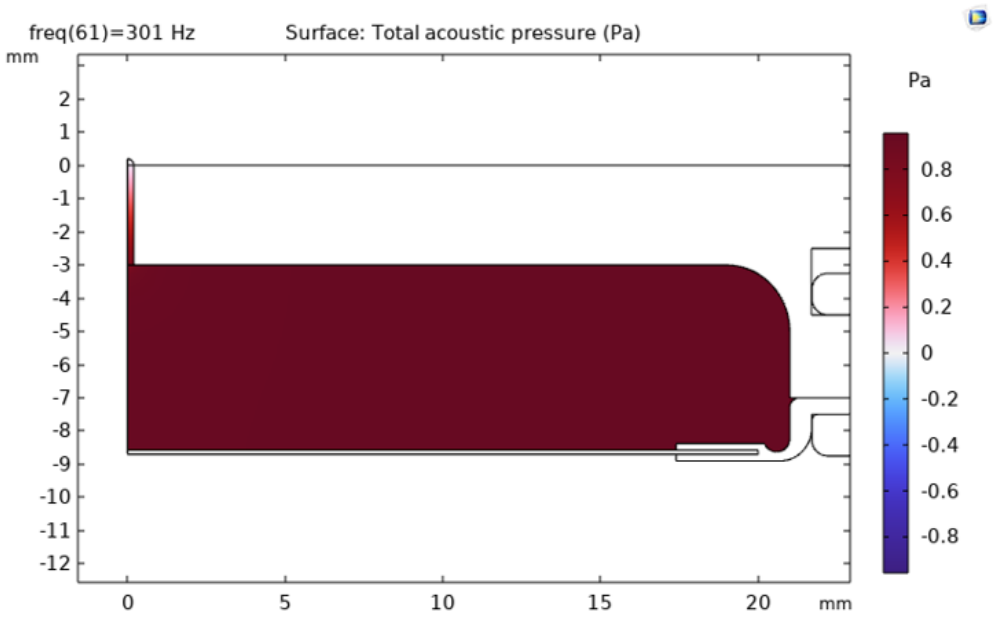

Figure 4.22: COMSOL distribution of pressure inside the acoustic chamber of the electronic stethoscope equipped with Littmann Master Cardiology.

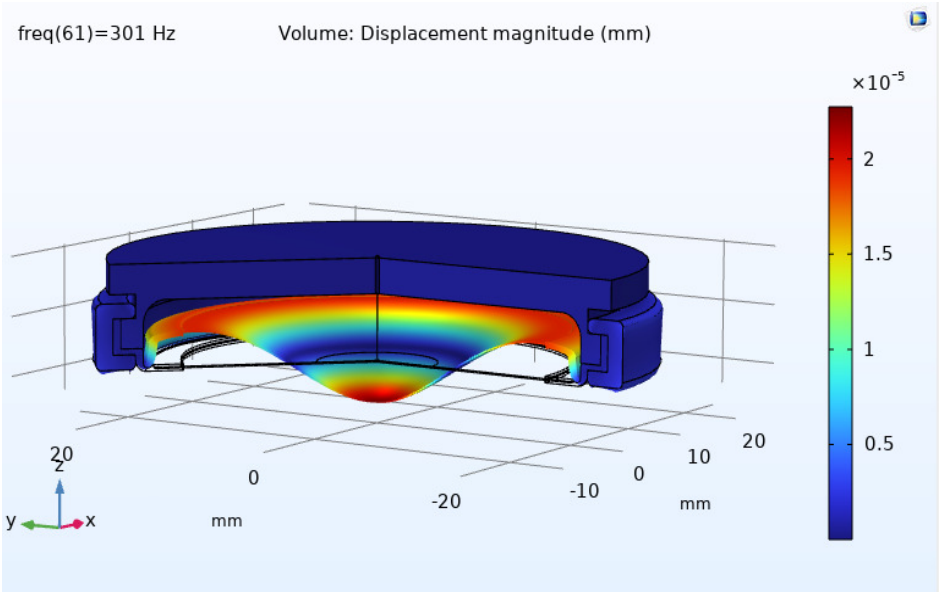

Figure 4.23: COMSOL deformation of the membrane. Amplitude of 20 μm at resonance frequency 300Hz

5 Membrane Optimization and Prototyping

5.1 Optimization Design Of Experiment

In order to improve the current vibrating membrane, namely the Littmann Master Cardiology, with which we are conducting our comparative analysis, we aim to stiffen the central disc while preserving the annular suspension. This modification is intended to increase the bandwidth while maintaining and enhancing sensitivity.

The vibrating membrane was initially analyzed using one-dimensional simulations [45]. One of the main advantages of performing 1D simulations in Simcenter Amesim is the low computational cost, which makes it particularly suitable for early stage design exploration. After validating the simulation model against experimental results [45], as explained in Chapter 4, a Design of Experiment (DOE) study was conducted using the software Design Expert.

The simulation framework described in Chapter 4 has been exploited to develop a new diaphragm for the prototype of electronic stethoscope. The goal of the design consists of maximizing bandwidth and gain of the system FRF $H_p(f)$. It is the absolute magnitude of the frequency response function of the whole system composed by lung, human tissues and vibrating membrane can be defined as

$$H_p\left(f\right) = \frac{p^{mic}_{pk-pk}\left(f\right)}{p^{lung}_{pk-pk}\left(f\right)} \tag{5.1}$$

where $p^{lung}_{pk-pk}\left(f\right)$ is the peak-to-peak pressure at the lung (see Section 4.2.1) and $p^{mic}_{pk-pk}\left(f\right)$ is the peak-to-peak pressure measured at the microphone as explained in Chapter 4.

The optimization phase follows the same approach as the validation framework: first, 1D simulations are performed, and then a refinement is carried out with 3D simulations. The process starts with the 1D model, the membrane was simplified as a classical mass-spring-damper system [45]. Accordingly, the key parameters: mass m, spring factor k, and damping factor c were systematically varied within realistic ranges. The DOE analysis yielded four viable parameter sets, in Table 5.1 is possible to note the input parameters, while in Table 5.2 are shown the results: Bandwidth at -3dB expressed in Hz; Pressure peak to peak at 300 Hz, identified as a significant

frequency for pressure, expressed in Pa and the delta of gain of pressure between 800Hz and 100Hz, $\triangle H_p = H_p@100Hz - H_p@800Hz$, that is dimensionless number and represents the decay of gain of the system (see Eq. 5.1). Figure 5.1 shows the results obtained from Design Expert for the first of these four configurations. The best parameter set has the lower value of Output (in signed value) because this means high bandwidth, high pressure that means high sensitivity due to the input is known and always the same and low decay of frequency response function $H_p(f)$. Since the excitation is known and identical across the frequency range, the pressure response (gain of pressure) can be directly interpreted as an indicator of the system sensitivity. The value of Output is equal to ((Bandwidth * Pressure peak to peak) / $\triangle H_p$). The bandwidth, delta gain pf pressure and pressure have been find with Amesim Simcenter, therefore performing 1D simulations.

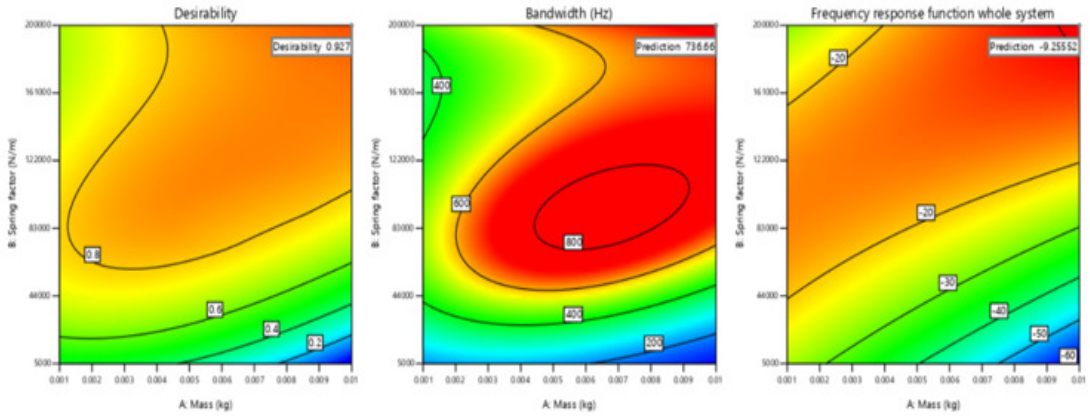

Figure 5.1: Solution 1 of DOE in Design Expert. The graphs show the desirability, bandwidth and frequency response function of the whole optimized system. The frequency response function is equal to Hp@800Hz-Hp@100Hz. The influence of damping factor is less important than the mass and the spring factor for this reason it does not appear in the x and y axis of the graphs.

Based on these findings, physical prototypes were designed using Solidworks and analyzed using Ansys.

Subsequently, Ansys, in combination with its software optimization tool, was employed to estimate the density, Young's modulus, and Poisson's ratio of the material deemed most suitable for the diaphragm. It is important to stress that these theoretically derived properties may not correspond to any naturally occurring material. Nevertheless, it is possible to identify either a composite or an existing material that closely approximates the target set of properties. The "optimal" material suggested by the simulations is characterized by being both lightweight and stiff, as exemplified by Kapton® and aluminum. This outcome is not unexpected: stiff materials facilitate the transmission of elastic waves at high frequencies, thereby satisfying the requirement for a broad operational bandwidth. Conversely, lightweight mate-

#RUN or #Solution DOE	#Configuration	M [kg]	K [N/m]	C [Ns/m]
Solution 1	1	0.01	200000	0.0267
Solution 66	2	0.0061	117705	0.1
RUN 26	3	0.0075	151250	0.02575
RUN 5	4	0.0055	102500	0.1

Table 5.1: DOE input with the goal of maximizing the bandwidth, the pressure and the gain of pressure.

#Configuration	Bandwidth [Hz]	$\triangle H_p$	P pk-pk [Pa]	Output
Reference	250	-40.75	4.3	-26
1	**723**	**-9.3**	**7**	**-544**
2	700	-11	7	-445
3	700	-10.3	7.34	-499
4	690	-10.65	7.18	-465

Table 5.2: DOE output. Bandwidth, pressure and gain of pressure are shown.The row called Refernce is Littmann Master Cardiology.

rials are essential to achieve acoustic impedance matching with human skin, which ultimately enhances the sensitivity and overall performance of the system.

A total of 34 runs were executed in Design-Expert, resulting in 66 possible solutions. For each of the four configurations listed in the Tables 5.1 and 5.2, physical prototypes were developed using real materials and subsequently tested in Ansys to verify that their mechanical properties matched as closely as possible the parameter sets identified by the Design Expert analysis.

For Configuration 1, the central diaphragm was modeled using a 0.6 mm thick AISI 316 stainless steel shim, coupled with a neoprene suspension and an outer ring made of epoxy resin. Using these material combinations, the Ansys simulation predicted a resonance frequency of the membrane of approximately 734 Hz while Amesim Simcenter predicted a bandwidth of the system of 723Hz. For Configuration 1, an alternative version, 1 bis of Table 5.3 was also proposed that maintains the same mass distribution proportions among the diaphragm, suspension, and outer ring. Specifically, the distribution was designed as two thirds of the total mass in the outer ring and one third in the diaphragm plus suspension. In this variant, the central vibrating diaphragm was modeled as a 0.7 mm thick aluminum alloy 6082 disk, combined with a neoprene suspension and an outer ring made of aluminum alloy 7075. In this case, the simulated resonance frequency was approximately 721 Hz.

For Configuration 2, the central vibrating diaphragm was made of aluminum alloy

7075, paired with a neoprene suspension and an epoxy resin outer ring.

Configuration 3 employed a 0.4 mm thick aluminum alloy 7075 diaphragm, again with a neoprene suspension and an outer ring made of aluminum alloy 7075.

For configuration 4 it has been used also a 0.3 mm aluminum alloy 7075 diaphragm, combined with a neoprene suspension and the same epoxy resin outer ring as in Configuration 2. However, in this case, the suspension geometry was modified to be slightly thinner and more compliant, which affected the system's dynamic behavior.

We opted to develop the first prototype of configuration 4 of diaphragm in 3D printing technology, since it allows us to control both the material properties and the geometry, at least in given ranges. The prototype has been realized in ONYX® by using a Markforged X7 3D-printer. The mechanical characteristics are Young modulus 2.4 GPa and density 1200 Kg/m3. We designed the diaphragm geometry to fit the case of the prototype of electronic stethoscope already developed by the collaborator of professor F. Pancaldi and to match the desired mass-spring-damper parameters.

The prototype of vibrating diaphragm is shown in Figure 5.2. It consists of a central disc capturing and transferring vibration waves to the pneumatic chamber, a suspension that links the central disc to the outer ring and a joint to fix the structure to the stethoscope body. Unlike the commercial membrane of the Littmann Master Cardiology stethoscope, where membrane and outer ring are two distinct parts, we implemented our new diaphragm in a single block due to the limit of 3D printer and its materials. Consequently, the suspension was designed with a thickness smaller than that of the central disc to make it more flexible. It is worth pointing out that the material employed in the first prototype is non-isotropic by the nature of the 3D printed process and layers orientation. In particular, the layer by layer deposition typically leads to different mechanical properties in the build direction (Z) compared to the in-plane directions (X–Y), with reduced stiffness and increased compliance along the stacking direction. As a consequence, the practical dynamic behavior of the prototype may deviate from that predicted by numerical simulations, which assume isotropic material properties. Additionally, manufacturing tolerances associated with the 3D-printing process may result in small deviations of the actual geometric dimensions from their nominal values, further contributing to discrepancies between simulated and experimental results.

In the case of the 3D-printed prototypes, two different design alternatives were developed and tested. The first, referred to as Configuration 4 bis, consists of a single monolithic component in ONYX®, in which both the outer ring and the central diaphragm were manufactured together during the same printing process, as described previously. This approach allowed for a straightforward fabrication process and ensured a perfect mechanical continuity between the ring and the diaphragm.

A second and slightly modified design, hereafter denoted as Configuration 4 tris, was also produced. In this configuration, the outer ring was not 3D-printed but taken directly from the Littmann Master Cardiology membrane, while only the central

Figure 5.2: New optimized 3D printed diaphragm with a thickness of 500 um and an external diameter of 51.8 mm. The external ring used to fix the diaphragm to the stethoscope has been considered as a rigid body to speed up the simulations

diaphragm was additively manufactured. This solution was specifically conceived to take advantage of the high mechanical quality and reliability of the Littmann outer ring when integrated into the stethoscope system, while still enabling the customization of the diaphragm through 3D printing. In this latter case, the thicknesses of the central disc were adjusted in order to restore values of mass m, spring constant k, and damping coefficient c consistent with the theoretical analyses.

Amesim Simcenter 1D simulation results related to the new 3D printed diaphragm are shown in Section 5.1.1.

Table 5.3 summarizes the actual material and geometric configurations corresponding to the parameter sets described in Tables 5.1 and 5.2.

#RUN or #Solution DOE	#Configuration	M [kg]	K [N/m]	C [Ns/m]
Solution 1	1	0.011	233962	0.1382
Solution 1	1 bis	0.0097	199068	0.085
Solution 66	2	0.00596	115293	0.127
RUN 26	3	0.0076	147018	0.076
RUN 5	4	0.00551	100584	0.046
RUN 5	4 bis	0.005	100000	0.014
RUN 5	4 tris	0.005	100000	0.014

Table 5.3: Results of DOE using real material. The column are from left to write: The number of RUN or the Solution, the configuration name, the mass, the spring factor and the damping factor expressed in the International System (SI) base unit.

Figure 5.3 shows the 3D Ansys simulation of the configuration 4 (case 4) membrane,

which was selected for physical prototyping due to its favorable performance and the availability of its constituent materials at scale. It is worth noting that the resonance frequency of the membrane in configuration 4 is 680 Hz, as shown in Figure 5.3, which differs from the 690 Hz reported in Tables 5.1 and 5.2. This discrepancy arises because the frequency shown in Figure 5.3 refers to the resonance of the membrane alone, whereas the value in Tables 5.1 and 5.2 accounts for the entire system, including the acoustic impedance of the stethoscope chamber. Since this is a modal analysis, the total deformation values shown in the legend are meaningful only up to a constant scaling factor.

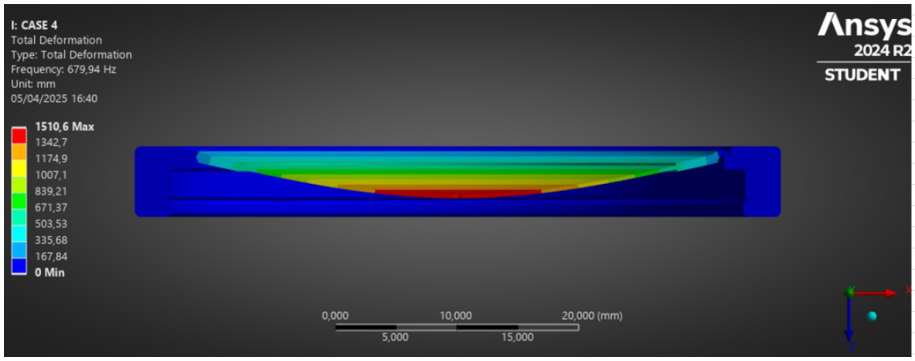

Figure 5.3: Ansys 3D Modal analysis simulation of configuration number four.

5.1.1 Results of 3D printed diaphragm

The prototype of the vibrating diaphragm is illustrated in Figure 5.2. The structure is composed of three main elements: a central disc responsible for capturing the acoustic induced vibrations and transferring them into the acoustic chamber; a suspension region that mechanically links the central disc to the outer ring; and a joint designed to secure the entire structure to the stethoscope body. Unlike the commercial Littmann Master Cardiology diaphragm, where the membrane and outer ring are manufactured as two distinct components, the newly developed prototype was conceived both as a single monolithic block and as two distinct parts. This design choice required the suspension region to be implemented with a reduced thickness compared to the central disc, thereby enhancing its flexibility and ensuring that the central portion could vibrate effectively. It should also be noted that the material, after deposition, employed for the first prototype is intrinsically non-isotropic due to the process of manufacturing, meaning that its real mechanical behavior may not perfectly coincide with the idealized properties assumed in numerical simulations.

The results of the Amesim 1D simulations conducted with this novel 3D-printed diaphragm (configuration 4 bis) virtually mounted on the electronic stethoscope are presented in Figures 5.4, 5.5 and 5.6. A comparison with the commercial Littmann diaphragm highlights a marked difference in resonance frequency: while

the Littmann diaphragm resonates at approximately 248 Hz, the ONYX® diaphragm exhibits a significantly higher resonance at 720 Hz. As a consequence, the pressure at the microphone, as well as the frequency response function (FRF) of the overall system, display a flatter behavior across a broader frequency range, which may represent an advantage for capturing higher frequency components of body sounds.

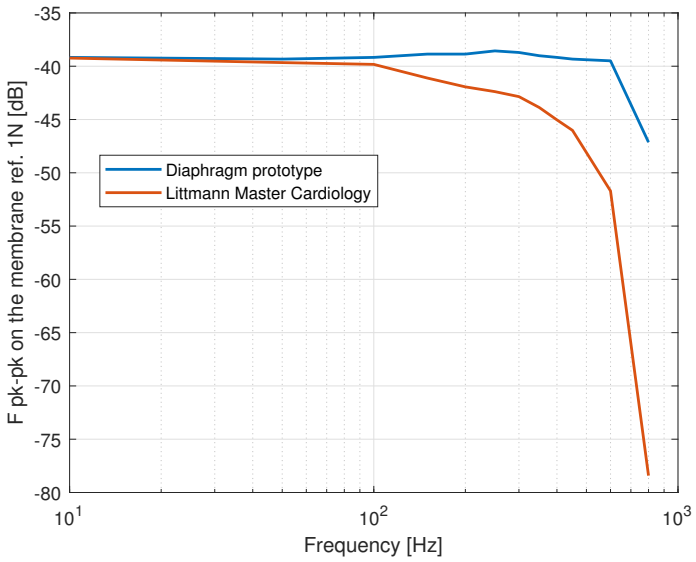

Figure 5.4: Peak-to-peak force on the new 3D-printed diaphragm in dB referring to 1N as a function of frequency blue line. Peak-to-peak force on the benchmark Littmann Master Cardiology diaphragm in dB referring to 1N as a function of frequency red line.

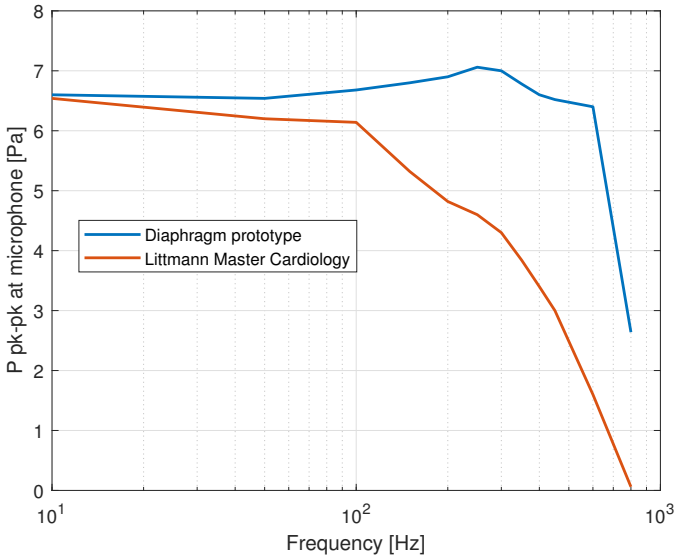

Figure 5.5: Pressure at microphone as a function of frequency for the new 3D printed diaphragm blue line. Pressure at microphone as a function of frequency for the benchmark Littmann Master Cardiology diaphragm red line.

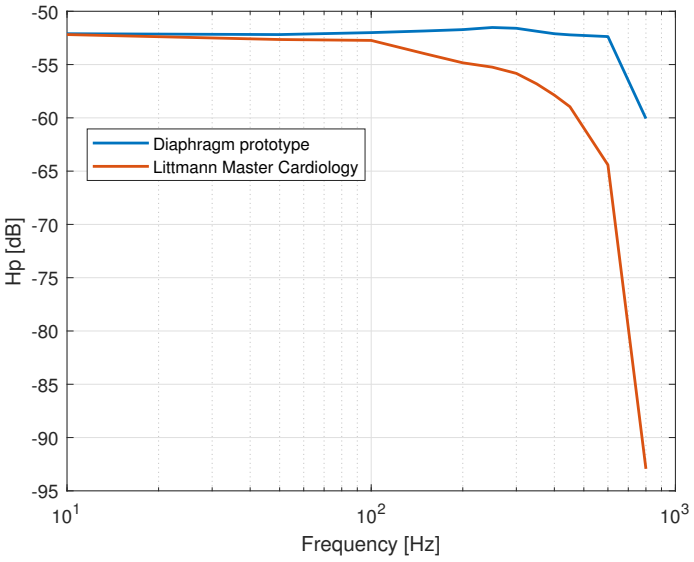

Figure 5.6: Frequency response function of the whole system Hp(f) including the new ONYX 3D printed diaphragm and the MEMS analogical microphone SPM0687LR5H blue line. Frequency response function of the whole system Hp(f) including the benchmark Littmann Master Cardiology diaphragm and the MEMS analogical microphone SPM0687LR5H red line.

A purely illustrative example of the harmonic response analysis, in Ansys, is pro-

vided in Figure 5.7. In this case, a sinusoidal pressure of 4.5 Pa is applied to the diaphragm, mimicking the pressure distribution observed at the microphone location at 720 Hz (bandwidth at -3dB as reported in Figures 5.4and 5.5). For clarity, the external ring is not shown, so as to emphasize the deformation pattern of the diaphragm. As expected, the maximum displacement occurs at the center of the diaphragm, gradually diminishing towards the periphery where the hidden external ring constrains the structure. This outcome confirms the validity of the suspension design and provides useful insight into the dynamic behavior of the diaphragm under harmonic excitation.

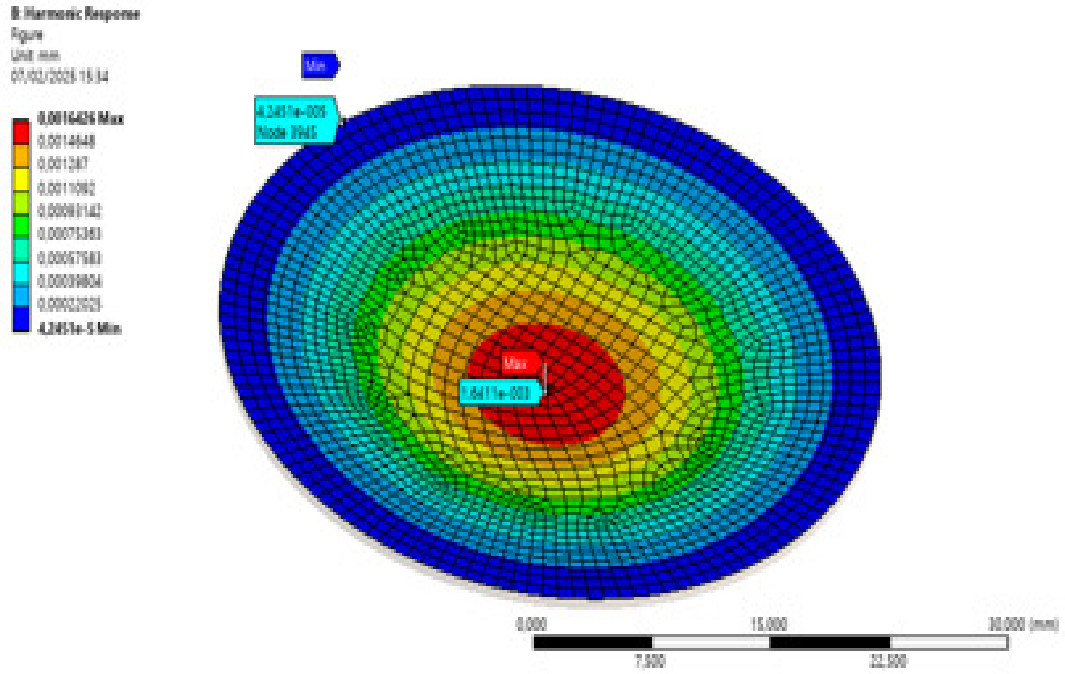

Figure 5.7: Example of simulation results carried out in Ansys 2024R2. The simulation represents the total deformation of diaphragm with a pressure of 4.5 Pa at resonance frequency of 720 Hz. The maximum displacement (red area) is 0.0016mm while the minimum (blue area) is 4.3x10^{-5}mm.

Characterization test by means Modal Shaker and Results In this paragraph, we analyze the real vibration test performed using a real modal shaker, which was carried out to measure the resonance frequency and the real damping factor of both the 3D printed membrane, configuration 4 bis and configuration 4tris (explained in Section 5.1), internally developed prototypes fabricated in our laboratory using 3D-printed ONYX® material. This represents an important starting point for potentially adjusting the damping parameters of the rubber and ONYX® materials in the simulation environment, which are difficult to estimate a priori due to the wide variability in the mechanical properties of plastics. The frequency range investigated

is from 100 Hz to 1000 Hz. Frequencies below 100 Hz correspond to cardiac sounds and are not relevant for the test conducted, as the focus is on pathological lung sounds [32]. The membranes tested include:

1. A membrane entirely made of ONYX®, including both the outer ring and the vibrating diaphragm (Full ONYX®/configuration 4 bis)

2. An hybrid membrane, consisting of the Littmann's outer ring and a vibrating central diaphragm in ONYX® (Hybrid/configuration 4 tris)

These 2 versions are shown in Figure 5.8.

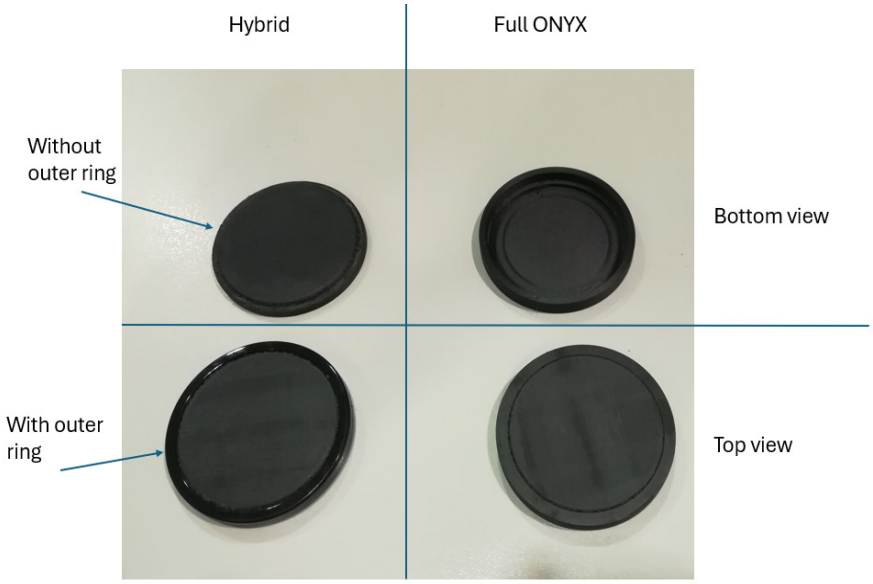

Figure 5.8: Tested membranes, two variants: Full ONYX®, Hybrid.

The test setup is configured as explained and showed in 4.2.3. For simplicity, the figure is reproduced below.

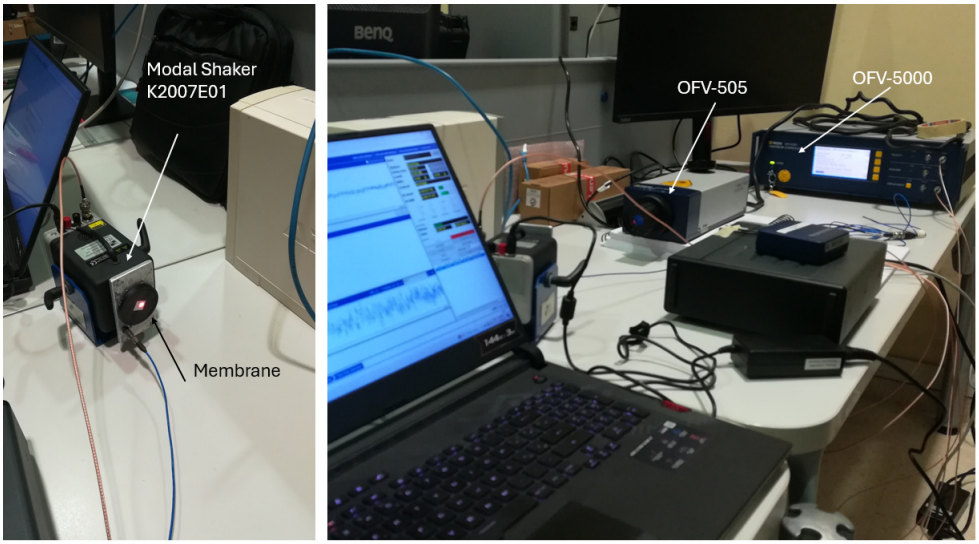

Figure 5.9: Test setup modal shaker.

The full ONYX® configuration 4 bis and the Hybrid configuration 4 tris were tested. In Figure 5.10 and respectively are shown the results. Although the input acceleration of the base of the modal shaker is nominally identical, it will be consistently displayed in subfigure a for the sake of completeness. In subfigure b, it has been represented the velocity output and not the acceleration because the accelerations were too noisy. In this case it has been applied, in Matlab environment, a low pass filter called Butterworth of the second order with a cutoff frequency of 20Hz and samplig frequency of 3200Hz for Figure 5.10b and cutoff frequency of 60Hz and samplig frequency of 3200Hz for Figure 5.11.

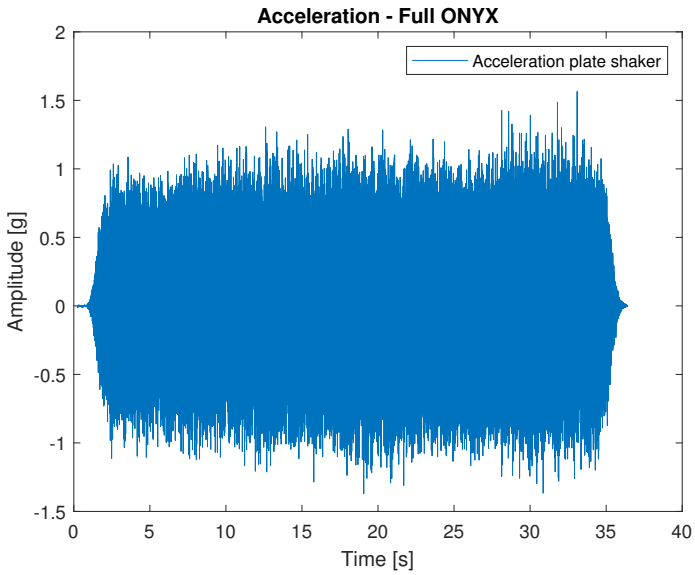

(a) Acceleration Input of the plate of the modal shaker K2007E01 for full ONYX membrane. The test setup is configured as explained in 4.2.3.

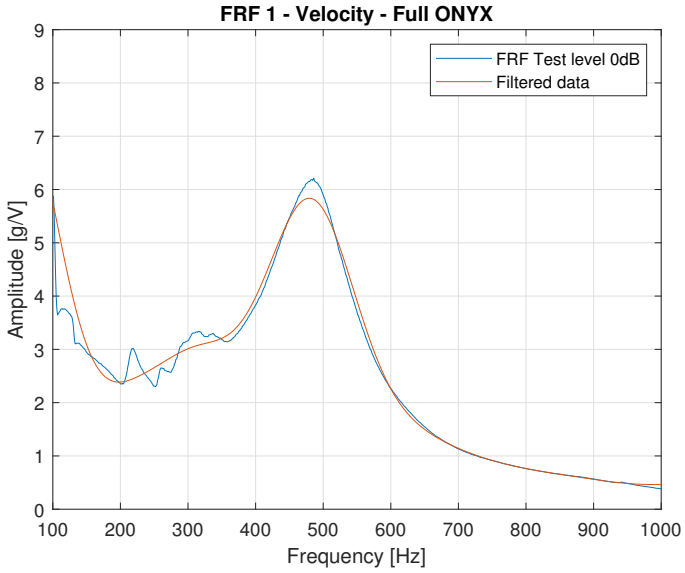

(b) Velocity Output of the vibrating diaphragm full ONYX membrane. Resonance frequency 485 Hz.

Figure 5.10: Configuration 4 bis (full ONYX®) characterization test. Acceleration Input of the modal shaker base and velocity Output of the vibrating diaphragm.

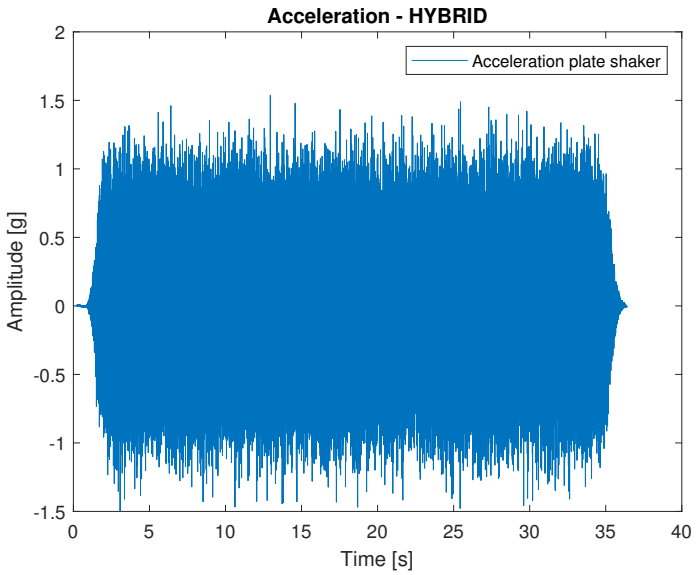

(a) Acceleration Input of the plate of the modal shaker K2007E01 for hybrid membrane. The test setup is configured as explained in 4.2.3.

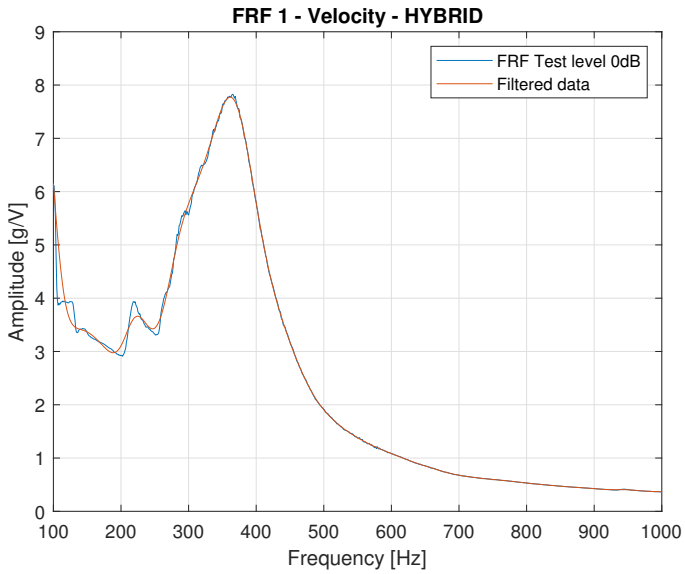

(b) Velocity Output of the vibrating diaphragm full ONYX membrane. The same filtering procedure was applied for consistency with the other analyses, even though the data were already relatively clean.

Figure 5.11: Configuration 4 tris (hybrid) characterization test. Acceleration Input of the modal shaker base and velocity Output of the vibrating diaphragm.

The blue line represents the real test result obtained after exciting the system with the acceleration level shown in subfigures a (see the explanation of the test provided

above and in Section 4.2.3). Before reaching this excitation level, it is good practice to perform preliminary tests at reduced signal intensity to avoid potential damage to the structure. The legend label "Test level 0 dB" indicates that the output shown corresponds exactly to that input level, and not to a reduced one.

The results for the full ONYX® membrane are quite close to the simulated ones (see Figures 5.4 and 5.10b), especially when considering the dimensional tolerances inherent to the 3D printing process used to fabricate the membrane. Assuming a manufacturing tolerance of ± 0.1 mm applied to the dimensions highlighted in purple in Figure 5.12, the resonance frequency, nominally 708 Hz, is expected to fall within a range of approximately 417 Hz to 944 Hz. The measured value of 485 Hz lies within this range, confirming the validity of the simulation under these tolerance constraints of the 3D printer process.

A different situation arises for the hybrid membrane version, for which the nominal resonance frequency was expected to be around 692 Hz, yet the measured value is significantly lower, as shown in Figure 5.11. Upon inspection of the printed sample, small micro-holes were observed along the outer circumference connecting the vibrating diaphragm to the outer ring. These defects, introduced during the 3D printing post-processing phase, likely compromised the structural integrity, reducing stiffness and consequently lowering the resonance frequency.

Additionally, in the simulation model the material was assumed to be isotropic for simplicity, whereas in reality, 3D printed materials exhibit anisotropic behavior, with mechanical properties depending on the build direction and layer orientation (e.g., reduced stiffness along the printing direction). This modeling assumption introduces further discrepancies between simulated and experimental results. Despite these limitations, in Littmann Master Cardiology and Full ONYX® cases the simulations closely match the experimental data, and the results can be considered highly satisfactory.

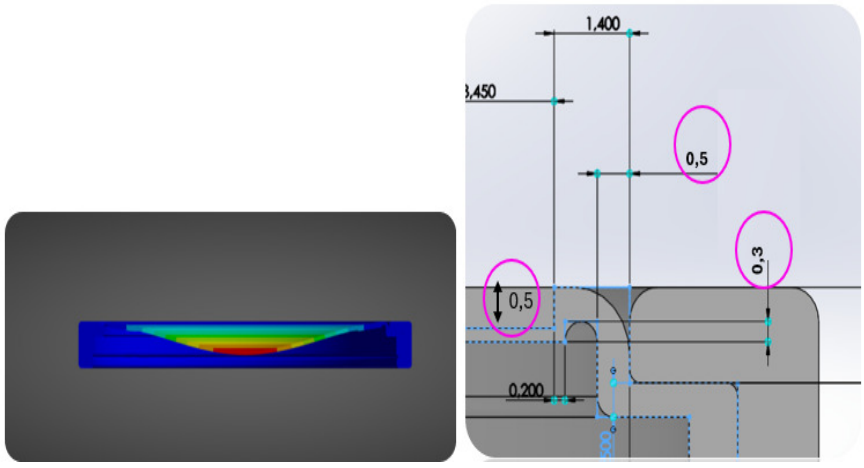

Figure 5.12: Ansys 3D simulations modal analysis of full ONYX membrane considering the tolerances of manufacturing. The dimensions highlighted in purple refer to features that have a influence on the resonance frequency. The dimensions in the figure represents the nominal ones.

5.1.2 Verifying by means three dimensional simulations

Since the 3D-printed prototypes were manufactured using an anisotropic manufacturing process, the resulting diaphragms exhibited limited repeatability and non-uniform mechanical properties. For this reason, it was decided not to pursue further developments with 3D-printed versions. Instead, configuration 4, 0.3 mm aluminum alloy 7075 diaphragm, combined with a neoprene suspension and the same epoxy resin outer ring (it is not monolithic), was selected as the reference design for refining the simulations, transitioning from the one-dimensional approach to a full three-dimensional analysis. Building upon the insights gained from both the 1D and preliminary 3D simulations, which were used to define the diaphragm geometry, a comprehensive 3D multiphysics simulation of the entire system was subsequently carried out using COMSOL Multiphysics.

The model involved a coupled structural–acoustic domain, enabling an accurate representation of the full physical behavior. The setup of simulation is explained in Chapter 4.

The input used in the 3D simulations was the same as that employed in the one-dimensional simulations, derived through FEM analysis (see Section 4.2.1). Once a simulation closely matching the real system behavior was achieved, the simulation model was considered validated. At that point, the geometry and material configuration corresponding to Configuration 4 were introduced.

A slight discrepancy was observed when comparing the results with the 1D simulations, likely due to a slightly higher acoustic impedance modeled in COMSOL,

which resulted in a lower resonance frequency, around 500 Hz (see Figure 5.14 and Table 5.2). However, the sensitivity increased by approximately 8 dB respect to Littmann Master Cardiology Benchmark (see Figures 5.13 and 5.14), indicating excellent performance, in close agreement with the one-dimensional simulation results.

This discrepancy can likely be attributed to the fact that the actual damping of the membrane is somewhat higher than what was initially assumed in the 1D model, which did not yet incorporate the results from the material characterization tests. Additional differences between the 1D and 3D simulations, such as the presence of wave reflections and acoustic energy absorption, also contribute to the observed variations.

Furthermore, the 3D simulations revealed that the material used for the outer ring does not significantly influence the system's dynamic response.

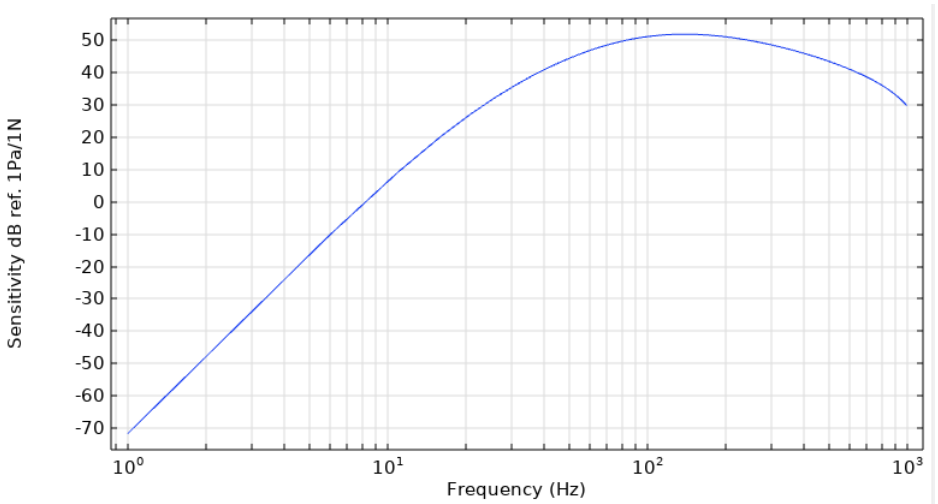

Figure 5.13: COMSOL sensitivity result of configuration 4 modified. Bandwidth at -3dB is 500Hz and maximum sensitivity is 60dB.

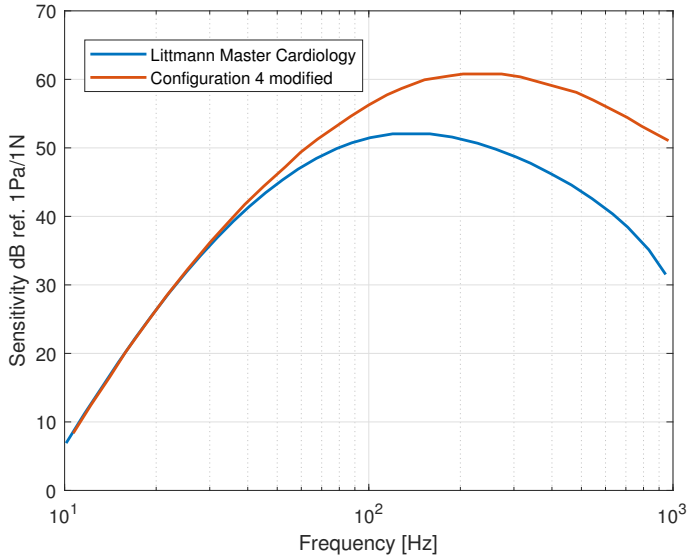

Figure 5.14: COMSOL sensitivity result of configuration 4 modified. Bandwidth at -3dB is 500Hz and maximum sensitivity is 60dB in blue. COMSOL sensitivity result of Littmann Master cardiology membrane. Bandwidth at -3dB is 290Hz and maximum sensitivity is 52dB in red. Graph realized in Matlab and data extracted by means web tool from the original images, Figures 5.13 and 5.13.

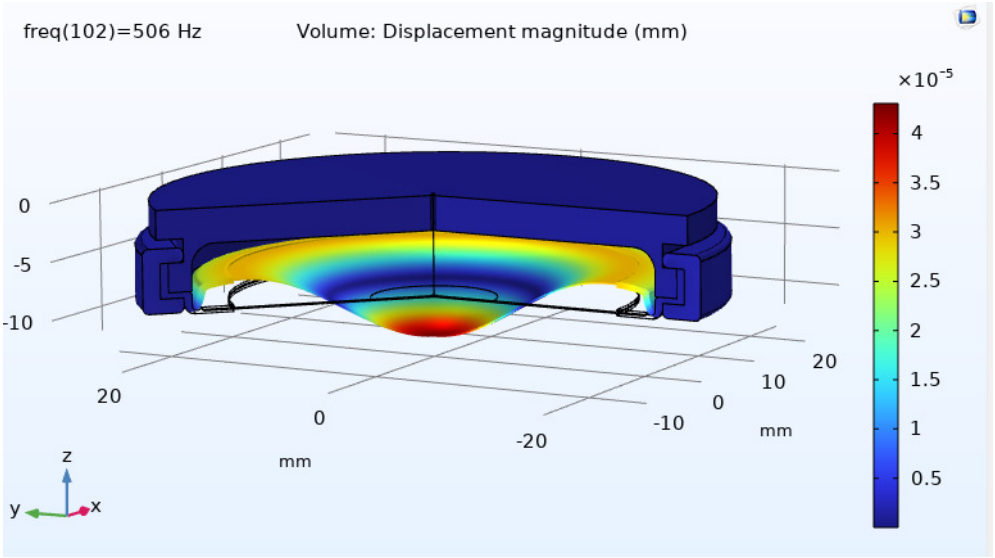

Figure 5.15: COMSOL deformation result of configuration 4 modified. Amplitude of 40μm of the diaphragm.

Figure 5.14 shows the sensitivity of membrane Configuration 4. The parametric study indicated that the material properties of the outer ring, originally modeled using epoxy resin, have a negligible influence on the overall system sensitivity, espe-

cially when compared to the dominant effect of the suspension elements. In light of this result, and with the objective of reducing the number of different materials to improve manufacturability and production feasibility, the outer ring was remodeled using neoprene. The central vibrating diaphragm was modeled as a 0.3 mm thick aluminum alloy 7075 disk as should be. This optimized membrane shows great performance respect to Littmann Master Cardiology membrane for the lung acquisition sounds environment. The sensitivity increase of 8dB and the frequency from 290Hz to 500Hz. The deformation of the optimized membrane is shown in Figure 5.15.

5.2 Prototyping

Finally, physical prototypes of this optimized version, i.e., the modified Configuration 4 with both the suspension and outer ring made of neoprene, were fabricated. To achieve this, a manual overmolding process was devised, combining the aluminum alloy 5052 diaphragm with the silicone-based suspension and outer ring.

A mold was designed in SolidWorks and 3D-printed. Aluminum alloy 5052 shows similar mechanical properties to aluminum alloy 7072 and silicone, whose mechanical properties are a little bit different to those of neoprene, was injected manually through casting channels using a syringe. As shown in Figure 5.16, the mold consists of three separate parts, which facilitates the removal of the final component after curing.

Alignment of the three mold components was ensured using dowel pins, and the assembly was held together with four M4 screws. The pre-cut aluminum disk was positioned inside the mold prior to closure, after which the silicone was injected. Figure 5.17 shows the resulting finished prototype.

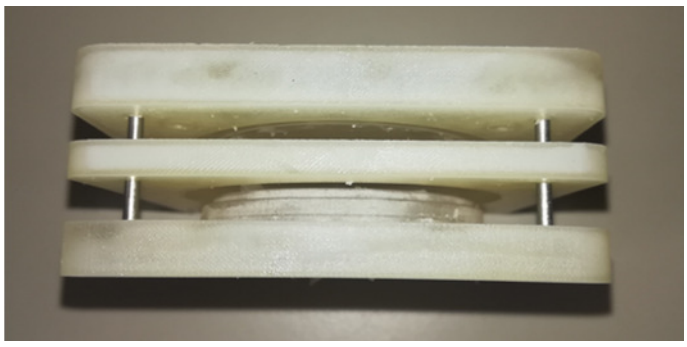

Figure 5.16: Mold realized by means resin 3D printed for fully silicone and aluminum alloy version.

Figure 5.17: Optimized membrane composed of central disc in aluminum alloy and outer ring and suspension in silicone.

The characterization tests have been carried out on the final prototype. The characterization test is explained in Chapter 4. The measured behavior generally agrees with that predicted by the simulations, although some discrepancies in the numerical values were observed due to differences in the actual material properties. These differences arise from technological limitations in the fabrication of the mold and, consequently, of the prototype itself. In particular, since the mold was produced using a resin-based process, it was not possible to employ neoprene rubber, whose high vulcanization temperature is incompatible with the resin material and the manual manufacturing procedure. Instead, silicone was selected as an alternative material, offering similar, though not identical, mechanical characteristics. The silicone material employed in the prototype exhibits a lower Shore hardness and Young's modulus compared to neoprene. As a result, during the characterization tests, the outer ring had a significant influence on the system's behavior, since it served as the fixation area of the diaphragm to the shaker base through beeswax. As shown in the experimental results (see Fig. 5.18), the measured bandwidth was relatively limited, which can be attributed to the softness of the silicone outer ring. The test setup is configured as explained and showed in 4.2.3.

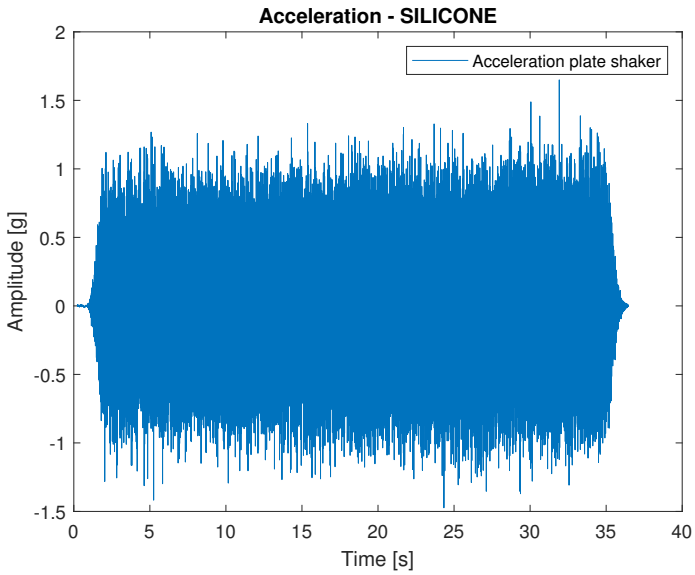

(a) Acceleration Input of the plate of the modal shaker K2007E01 for configuration 4 membrane.

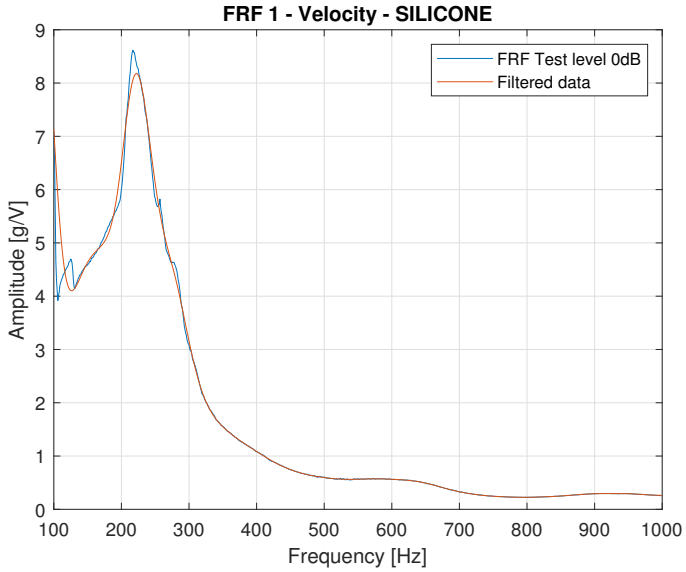

(b) Velocity Output of the vibrating diaphragm where the outer ring and suspension are made in silicone and the central disc is made in aluminum alloy 5052.

Figure 5.18: Configuration 4 characterization test. Acceleration Input of the modal shaker base and velocity Output of the vibrating diaphragm.

To address this limitation, a new version of the prototype was developed. In this configuration, the outer ring of the Littmann stethoscope, made of neoprene, was retained, while the central Aluminum Alloy (AA5052) disk was co-molded with the silicone suspension. The co-molded component was then inserted into the Littmann

outer ring, following the same layout as the configuration 4 tris (hybrid with silicone and aluminum alloy) model. Figure 5.19 shows the mold used for this process, while Figure 5.20 presents the molded and assembled component within the Littmann outer ring.

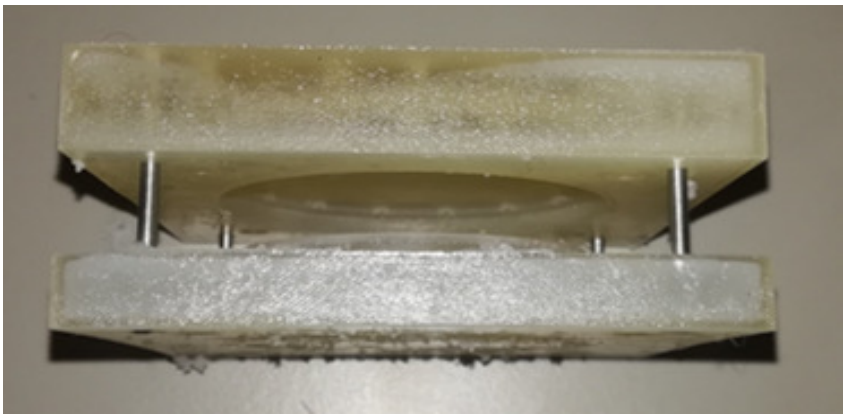

Figure 5.19: Mold realized by means resin 3D printed for hybrid version: silicone, neoprene and aluminum alloy.

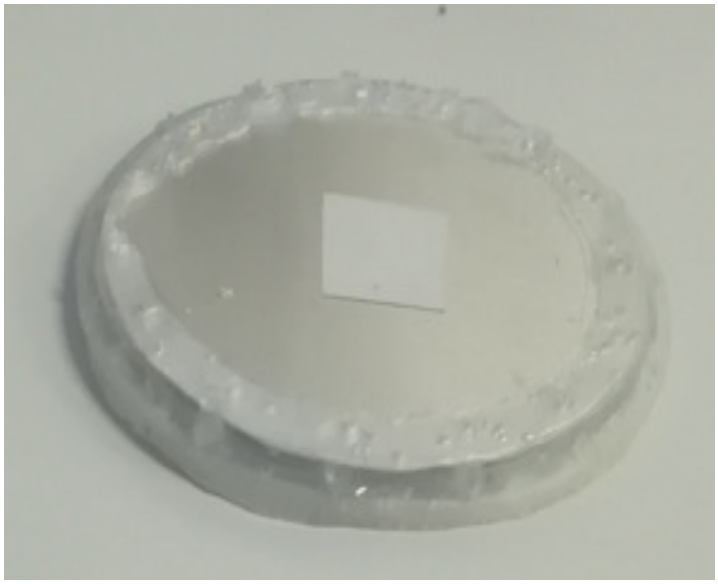

(a) Central disc in aluminum alloy plus suspension in silicone.

(b) Central disc in aluminum alloy plus suspension in silicone plus outer ring of Littmann Master Cardiology stethoscope.

Figure 5.20: Optimized membrane composed of central disc in aluminum alloy and suspension in silicone and outer ring is the Littmann one.

As can be observed in Figure 5.21, this configuration exhibits an increased bandwidth. Although the measured response does not perfectly match the simulated one, the overall behavior remains consistent with the numerical predictions, considering that the silicone material is softer than neoprene.

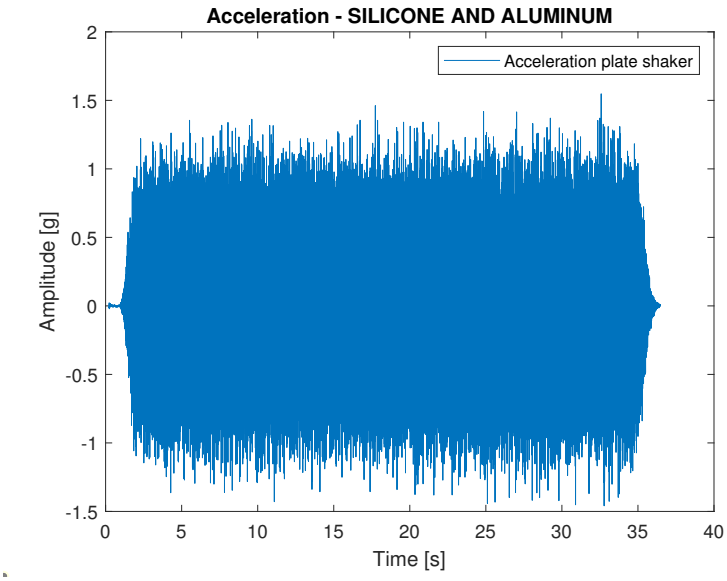

(a) Acceleration Input of the plate of the modal shaker K2007E01 for hybrid membrane.

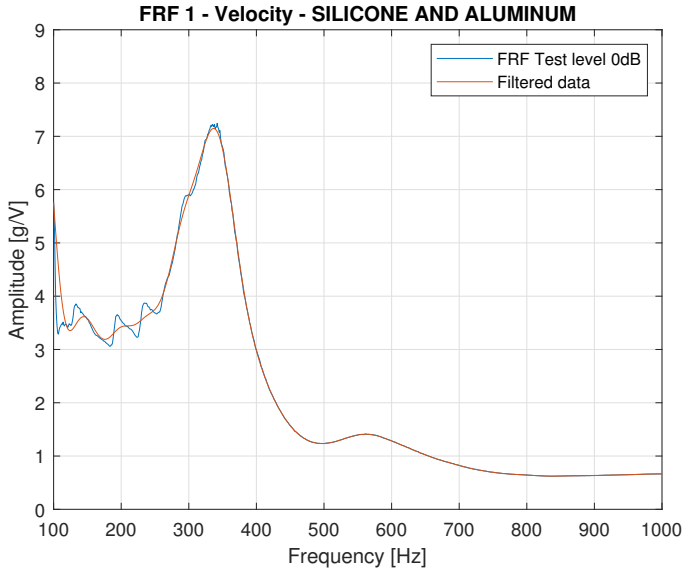

(b) Velocity Output of the vibrating diaphragm where the outer ring is made in neoprene, suspension is made in silicone and the central disc is made in aluminum alloy 5052.

Figure 5.21: Configuration 4 hybrid characterization test. Acceleration Input of the modal shaker base and velocity Output of the vibrating diaphragm.

The acoustic sensitivity cannot be accurately assessed from these tests alone, as it would require replicating the experimental setup described in [44], which includes coupling with the standard skin. Nevertheless, Figure 5.22 compares the responses of the four optimized versions with that of the original Littmann diaphragm. The

Aluminum Alloy and Silicone version (orange curve) demonstrates higher sensitivity than the Aluminum Alloy, Silicone and Neoprene version (yellow curve), likely because the latter configuration is slightly constrained within the outer ring, resulting in reduced transmissibility due to the stiffer suspension. Conversely, the Aluminum Alloy and Silicone version (orange curve), where the suspension is not mechanically constrained, exhibits a sensitivity comparable to the Littmann diaphragm. It should be noted that the sensitivity curves presented are not expressed in decibels and are not evaluated solely at the resonance peak. In this figure, sensitivity is primarily assessed in the pre-resonant frequency region, which is more representative of the operational regime and less affected by damping-dependent amplification effects.

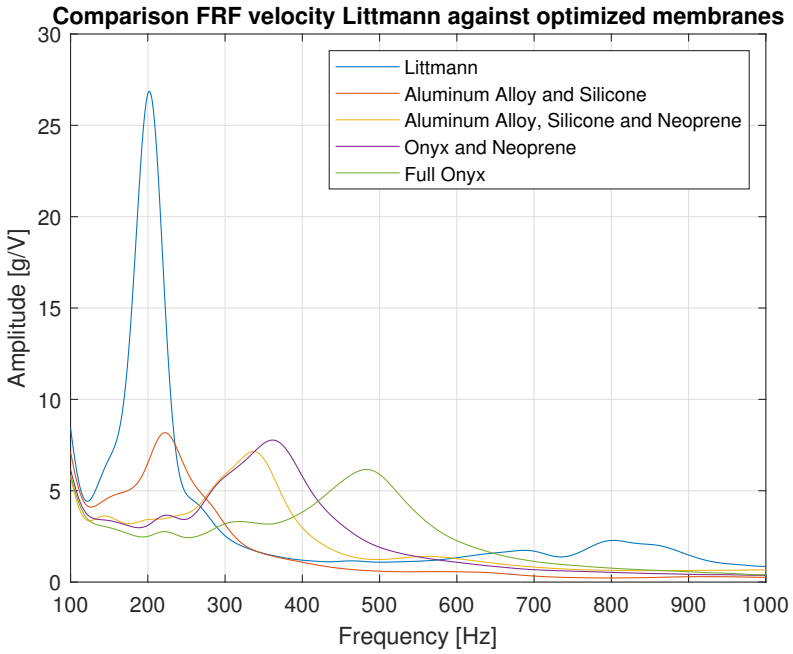

Figure 5.22: Comparison among the four optimized version of membrane wit the Littmann Master Cardiology.

Regarding the Aluminum Alloy, Silicone and Neoprene configuration (yellow curve), the frequency response reveals an increased transmissibility with respect to the Littmann diaphragm within the spectral range associated with pathological lung sounds, approximately from 200–300 Hz up to 600–700 Hz. Below 266 Hz (intersection between the two curves), the response is attenuated respect to Littmann Master Cardiology. This behavior can be interpreted as a mechanically induced filtering effect, resulting from the combined stiffness and damping of the suspension membrane system. In particular, the increased effective stiffness shifts the dynamic response toward higher frequencies, thereby reducing sensitivity to low-frequency components typically associated with heart sounds. From a sensor perspective, this selective frequency response is advantageous, as it enhances lung-sound-related vibrations while suppressing undesired low-frequency excitation. The optimized con-

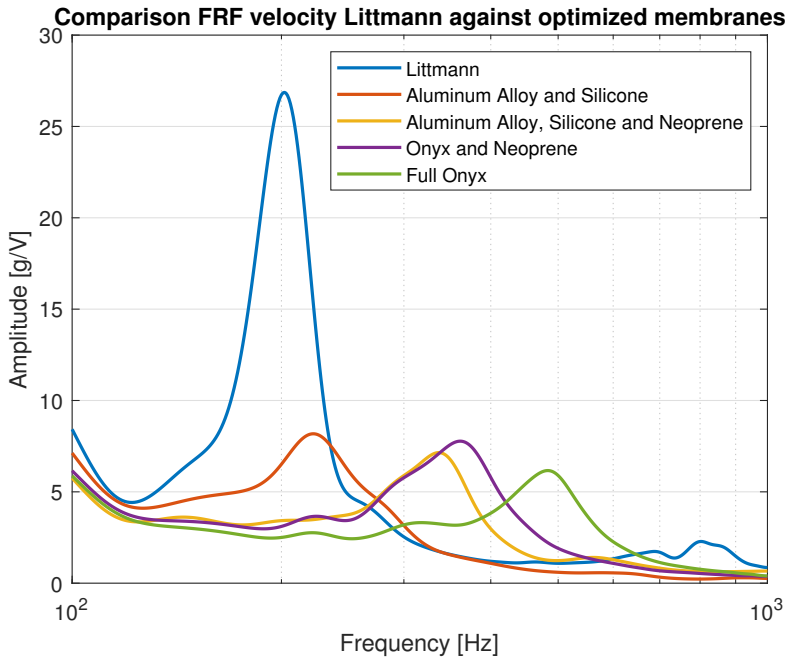

Figure 5.23: Comparison among the four optimized version of membrane wit the Littmann Master Cardiology. X-axis logaritmic.

figurations (ONYX® and neoprene – purple curve; full ONYX® – green curve) further exhibit a significantly wider operational bandwidth compared to the Littmann Master Cardiology diaphragm, indicating a more broadband and stable mechanical response rather than a narrow resonance-dominated amplification. The slightly reduced transmissibility observed for the full ONYX® diaphragm can be attributed to the increased global stiffness of the one-piece structure, which effectively stiffens the suspension and limits vibration amplitude.

Despite this, each optimized configurations achieve performance levels comparable to the reference device at low frequencies, while offering improved bandwidth and frequency selectivity.

These results are particularly encouraging considering that the materials employed differ from those assumed in the numerical optimization, due to the manufacturing constraints discussed previously. At low frequency (100 Hz - before Littmann Master Cardiology peak) the magnitude between Littmann Master Cardiology and the optimized versions are very close.

A fully controlled industrial manufacturing process will be required to precisely reproduce the targeted mechanical properties of both the mold and diaphragm, ensuring consistency with the optimized design parameters.

6 Conclusions

In this thesis we investigated the effect of the vibrating diaphragm on the sensitivity and bandwidth of an electronic stethoscope, with the overarching objective of improving the quality of lung sound acquisition for the early identification of pathological events. The research followed a structured path, progressing from clinical considerations to numerical modeling, simulation, prototyping, and experimental validation.

As a first step, the clinical context was analyzed in order to define the requirements of the system in terms of acoustic bandwidth, pressure gain, sensitivity and pressure exerted by the lungs. On this basis, a numerical framework of the entire system for one-dimensional (1D) simulation was developed by means Amesim Simcenter software. The 1D model describes the system composed of the lung, the chest wall, the vibrating diaphragm, and the sensing unit (microphone). The diaphragm was represented as a mass–spring–damper system, allowing its dynamic behavior to be approximated with a small set of parameters: mass m, spring factor k, and damping coefficient c.

To extract realistic values for these parameters, a three-dimensional (3D) finite element model of the only human body tissues was developed in Ansys. As an initial reference, the commercial Littmann Master Cardiology diaphragm was considered. Its mechanical behavior was experimentally characterized using a modal shaker, and the corresponding spring and damping constants were calibrated by matching numerical predictions with measured frequency response. This step enabled the refinement of both the 1D and 3D models, ensuring that they were consistent with experimental data and with previously reported results in the literature.

Once validated, the 1D model was employed as the main tool for rapid parametric studies and optimization, thanks to its computational efficiency. The design variables were adjusted to maximize the acoustic bandwidth, the gain of pressure at the microphone, and the overall sensitivity. The best performing configurations identified by the 1D model were then further refined and verified using the 3D simulations by means Comsol Multiphysics of the entire system. From this combined numerical investigation, a set of promising diaphragm configurations was obtained, satisfying the defined design objectives.

Prototyping was carried out in two phases. In a preliminary attempt, selected configurations were fabricated using 3D printing technology and tested with the same modal shaker employed for the characterization of the reference Littmann

diaphragm. While some prototypes provided encouraging results, limitations of 3D-printed anisotropic manufacturing process became evident: the non-homogeneous and non-isotropic behavior of printed polymers compromised the reliability and fidelity of the acoustic response. To overcome these limitations, a new diaphragm was realized using isotropic and homogeneous materials. An aluminium alloy central disk with a thickness of 0.3 mm was combined with a neoprene suspension. The material of the outer ring was found to have negligible influence on the global performance. This manufacturing approach provided a more robust and reliable prototype, even though industrial grade moulding techniques will be required in the future to achieve consistent results. Indeed, due to the constraints of the available 3D-printed resin mold, which cannot withstand the vulcanization temperature of neoprene, silicone was employed as a substitute material in the present prototypes, the silicone has not the same mechanical properties.

The experimental results confirmed the validity of the proposed design. The resonance frequency of the Littmann Master Cardiology diaphragm is about $200 - 250$ Hz, while the newly optimized membrane had a frequency resonance around 700 Hz in accordance to the 1D numerical framework, while the 3D simulations predicted 500 Hz, highlighting the role of the air cavity as an acoustic damper, which is only partially captured by the simplified 1D model. Importantly, the new diaphragm exhibited an increase in sensitivity of about 8 dB with respect to the commercial Littmann diaphragm, with sensitivity expressed in A-weighted terms. The predicted pressure at the microphone in the $100 - 800$ Hz band was in the range $0 - 6$ Pa peak-to-peak, while experimental tests with the prototype indicated approximately 3 Pa, confirming good agreement between numerical and experimental data. Each prototypes produced, two types made with 3D printing and two types made of silicone, were tested and showed consistency with the simulations, even when accounting for the differences in material properties compared to the ideal materials. The results are excellent, as they demonstrate a wider bandwidth than the current Littmann Master Cardiology diaphragm, with transmissibility comparable to that of the Littmann, despite the material limitations discussed in the previous chapter. Acoustic sensitivity was not evaluated in the performed tests, since it depends on the coupling with the human body and cannot be assessed solely from the results obtained using the modal shaker tests in air.

In conclusion, the thesis demonstrated that it is possible to design and fabricate a vibrating diaphragm that substantially enhances both bandwidth and sensitivity compared to current commercial solutions. The combined 1D–3D modeling framework proved effective for guiding the design process and provided physical insight into the role of diaphragm geometry, material properties, and acoustic interactions. Although the current prototype employs substitute materials due to manufacturing limitations, the results clearly point towards a path for industrial grade development. The next step will consist of validating the prototype on a modal shaker with optimized isotropic membranes manufactured through professional moulding processes, in collaboration with specialized industrial partners. Ultimately, these

results provide a strong foundation for the development of a new class of electronic stethoscopes with superior diagnostic capabilities.

Acknowledgments

First and foremost, I would like to express my deepest gratitude to my parents for the constant support they have given me from the very beginning of my university studies up to the present day, not only from an academic and financial perspective, but also on a personal level. Having always been a student living away from home, the sacrifices and economic efforts required have been considerable. I do not wish to thank them solely for their financial commitment, but above all for the personal encouragement they have provided at every significant academic milestone and beyond. Now that this cycle of studies is coming to an end, looking back I truly believe it has been a remarkable journey, and I sincerely hope that this chapter, which is now closing, will be only the beginning of another great adventure.

I am deeply grateful to my partner for her unwavering support throughout these past months and years, during this intense and rewarding doctoral journey. She has always been present and ready to share with me the daily challenges and commitments that this extraordinary path has entailed. She has been an invaluable presence, and truly the most supportive companion I could have hoped for by my side throughout this journey.

I would also like to extend my heartfelt thanks to my exceptional supervisors and tutors for their professionalism, guidance, and invaluable support during this doctoral program and on such a fascinating research topic. I am especially grateful for their kindness and affability, which have brought lightness and serenity to this journey. Dedicating time, effort, and energy with the ultimate aim of improving patients' lives is something truly inspiring, which has continuously motivated me to give my very best, even in the most challenging moments of fatigue and difficulty.

I would also like to thank all the people I have met along my path who have shared with me a piece of their knowledge.

Thanks to all.

Bibliography

[1] Alamanos Y, Drosos AA. Epidemiology of adult rheumatoid arthritis. Autoimmunity Rev. 2005 Mar;4(3):130-6. doi: 10.1016/j.autrev.2004.09.002

[2] Scott DL, Wolfe F, Huizinga TW. Rheumatoid arthritis. Lancet. 2010 Sep 25;376(9746):1094-108. doi: 10.1016/S0140-6736(10)60826-4

[3] Kelly CA, Saravanan V, Nisar M, et al. Rheumatoid arthritis-related interstitial lung disease: associations, prognostic factors and physiological and radiological characteristics--a large multicentre UK study. Rheumatology (Oxford). 2014 Sept;53(9):1676-82. doi: 10.1093/rheumatology/keu190

[4] M. Shaw, B. F. Collins, L. A. Ho, G. Raghu, Rheumatoid arthritis-associated lung disease, European Respiratory Review 2015 24(135): 1-16; DOI: https://doi.org/10.1183/09059180.00008014

[5]] J.K. Dawson, H.E. Fewins, J. Desmond, M.P. Lynch, D.R. Graham, Fibrosing alveolitis in patients with rheumatoid arthritis as assessed by high resolution computed tomography, chest radiography, and pulmonary function tests, Thorax 56 (2001) 622–627.

[6] Nikolic, A. Barney, F. Pancaldi, L. Larcher, F. Luppi, M.G. Jones, D. Davies, L. Richeldi, "velcro-type" crackles predict specific radiologic features of fibrotic interstitial lung disease, BMC Pulm. Med. 18 (1) (2018) http://dx.doi.org/10.1186/s12890-018-0670-0.

[7] A. Manfredi et al., Usefulness of digital velcro crackles detection in identification of interstitial lung disease in patients with connective tissue diseases, 2020 Jun 25;36(1):19–25. doi: 10.46497/ArchRheumatol.2021.7975

[8] G. Koduri, S. Norton, A. Young, N. Cox, P. Davies, J. Devlin, J. Dixey, A. Gough, P. Prouse, J. Winfield, P. Williams, Interstitial lung disease has a poor prognosis in rheumatoid arthritis: results from an inception cohort, Rheumatology 49 (2010) 1483–1489.

[9] T. Bongartz, C. Nannini, Y.F. Medina-Velasquez, S.J. Achenbach, C.S. Crowson, J.H. Ryu, R. Vassallo, S.E. Gabriel, E.L. Matteson, Incidence and mortality of interstitial lung disease in rheumatoid arthritis, Arthritis Rheum. 62 (6) (June 2010) 1583–1591

[10] C. Hyldgaard, O. Hilberg, A.B. Pedersen, S.P. Ulrichsen, A. Lokke, E. Bendstrup, T. Ellingsen, A population-based cohort study of rheumatoid arthritis-associated interstitial lung disease: comorbidity and mortality, Ann. Rheum. Dis. 76 (10) (June 2017) 1700–1706.

[11] E.J. Kim, B.M. Elicker, F. Maldonado, W.R. Webb, J.H. Ryu, J.H. Van Uden, J.S. Lee, T.E. King Jr., H.R. Collard, Usual interstitial pneumonia in rheumatoid arthritisassociated interstitial lung disease, Eur. Respir. J. 35 (2010) 1322–1328.

[12] E. Gabbay, R. Tarala, R. Will, G. Carrol, B. Adler, D. Cameron, F.R. Lake, Interstitial lung disease in recent onset rheumatoid arthritis, Am. J. Respir. Crit. Care Med. 156 (1997) 528–535.

[13] Z.X. Yunt, J.H. Chung, S. Hobbs, E.R. Fernandez-Perez, A.L. Olson, T.J. Huie, R.C. Keith, W.J. Janssen, B.L. Goldstein, D.A. Lynch, K.K. Brown, J.J. Swigris, J.J. Solomon, High resolution computed tomography pattern of usual interstitial pneumonia in rheumatoid arthritis-associated interstitial lung disease: relationship to survival, Elsevier Respir. Med. 126 (2017) 100–104.

[14] N. Mohd Noor, M.S. Mohd Shahrir, M.S. Shahid, R. Abdul Manap, A.M. Shahizon Azura, S. Azhar Shah, Clinical and high resolution computed tomographycharacteristics of patients with rheumatoid arthritis lung disease, Int. J. Rheum. Dis.12 (2009) 136–144.

[15] M.J. Hamblin, M.R. Horton, Rheumatoid arthritis-associated interstitial lung disease: diagnostic dilemma, Hindawi Pulm. Med. (2011), https://doi.org/10.1155/2011/872120.

[16] K.G. Saag, J.R. Cerhan, S. Kolluri, K. Ohashi, G.W. Hunninghake, D.A. Schwartz, Cigarette smoking and rheumatoid arthritis severity, Ann. Rheum. Dis. 56 (1997) 463–469.

[17] N.G. Papadopoulos, Y. Alamanos, P.V. Voulgari, E.K. Epagelis, N. Tsifetaki, A.A. Drosos, Does cigarette smoking influence disease expression, activity and severity in early rheumatoid arthritis patients? Clin. Exp. Rheumatol. 23 (2005) 861–866.

[18] B.R. Gochuico, N.A. Avila, C.K. Chow, L.J. Novero, H.-P. Wu, P. Ren, S.D. MacDonald, W.D. Travis, M.P. Stylianou, I.O. Rosas, Progressive preclinical interstitial lung disease in rheumatoid arthritis, Arch. Intern. Med. 168 (2) (2008) 159–166.

[19] Mehdi Mirsaeidi Pamela Barletta Marilyn K. Glassberg, Systemic Sclerosis Associated Interstitial Lung Disease: New Directions in Disease Management, Front. Med., 31 October 2019 Sec. Pulmonary Medicine Volume 6 - 2019, https://doi.org/10.3389/fmed.2019.00248

[20] G. Cerro Chiang, T. Parimon, Understanding Interstitial Lung Diseases Associated with Connective Tissue Disease (CTD-ILD): Genetics, Cellular Pathophysiology, and Biologic Drivers, Int J Mol Sci 2023 Jan 26;24(3):2405. doi: 10.3390/ijms24032405.

[21] Tyndall AJ, Bannert B, Vonk M, et al. Causes and risk factors for death in systemic sclerosis: a study from the EULAR Scleroderma Trials and Re-

search (EUSTAR) database. Ann Rheum Dis. 2010 Oct;69(10):1809-15. doi: 10.1136/ard.2009.114264. Epub 2010 Jun 15.

[22] Marie I, Hachulla E, Cherin P, et al. Interstitial lung disease in polymyositis and dermatomyositis. Arthritis Rheum. 2002 Dec 15;47(6):614-22. doi: 10.1002/art.10794

[23] A. Manfredi at al., Acute exacerbation of interstitial lung diseases secondary to systemic rheumatic diseases: a prospective study and review of the literature, J Thorac Dis. 2019 Apr;11(4):1621-1628. doi: 10.21037/jtd.2019.03.28.

[24] Gasperini ML, Gigante A, Iacolare A, Pellicano C, Lucci S, Rosato E. The predictive role of lung ultrasound in progression of scleroderma interstitial lung disease. Clin Rheumatol. 2020;39:119–123. - PubMed

[25] Antin-Ozerkis D, Hinchcliff M. Connective Tissue Disease-Associated Interstitial Lung Disease: Evaluation and Management. Clin Chest Med. 2019;40:617–636. - PubMed

[26] Wells A, Devaraj A, Renzoni EA, Denton CP. Multidisciplinary Evaluation in Patients with Lung Disease Associated with Connective Tissue Disease. Semin Respir Crit Care Med. 2019;40:184–193. - PubMed

[27] Dong X, Zhou J, Guo X, Li Y, Xu Y, Fu Q, et al. A retrospective analysis of distinguishing features of chest HRCT and clinical manifestation in primary Sjögren's syndrome-related interstitial lung disease in a Chinese population. Clin Rheumatol. 2018;37:2981–2988. - PubMed

[28] Cobo-Ibáñez T, López-Longo FJ, Joven B, Carreira PE, Muñoz-Fernández S, Maldonado-Romero V, et al. Long-term pulmonary outcomes and mortality in idiopathic inflammatory myopathies associated with interstitial lung disease. Clin Rheumatol. 2019;38:803–815. - PubMed

[29] M. Kreider , K. Highland, Pulmonary Involvement in Sjögren Syndrome, Thieme Medical Publishers 333 Seventh Avenue, New York, NY 10001, USA, Semin Respir Crit Care Med 2014; 35(02): 255-264 DOI: 10.1055/s-0034-1371529

[30] Markus Gutsche, Glenn D Rosen, Jeffrey J Swigris, Connective Tissue Disease-associated Interstitial Lung Disease: A review, Curr Respir Care Rep. 2012 Sep 21;1:224–232. doi: 10.1007/s13665-012-0028-7

[31] Clio P. Mavragani, Haralampos M. Moutsopoulos, Sjögren's syndrome: Old and new therapeutic targets, Journal of Autoimmunity Volume 110, June 2020, 102364, https://doi.org/10.1016/j.jaut.2019.102364

[32] A. Fava, B. Dianat, A. Bertacchini, A. Manfredi, M. Sebastiani, M. Modena and F. Pancaldi, "Pre-processing techniques to enhance the classification of lung sounds based on deep learning", Biomedical Signal Processing and Control, vol. 92, June 2024, DOI: 10.1016/j.bspc.2024.106009

[33] F. Pancaldi et al., VECTOR: An algorithm for the detection of COVID-19 pneumonia from velcro-like lung sounds, Computers in Biology and Medicine Volume 142, March 2022, 105220, https://doi.org/10.1016/j.compbiomed.2022.105220

[34] C.R. Carpenter, P.A. Mudd, C.P. West, E. Wilber, S.T. Wilber, Diagnosing COVID-19 in the emergency department: a scoping review of clinical examinations, laboratory tests, imaging accuracy, and biases, Acad. Emerg. Med. 27 (8) (2020) 653–670, https://doi.org/10.1111/acem.14048.

[35] Y. Cao, X. Liu, L. Xiong, K. Cai, Imaging and clinical features of patients with 2019 novel coronavirus SARS-CoV-2: a systematic review and meta-analysis, J. Med. Virol. 92 (9) (2020) 1449–1459, https://doi.org/10.1002/jmv.25822.

[36] E.S. Hosseini, N.R. Kashani, H. Nikzad, J. Azadbakht, H.H. Bafrani, H.H. Kashani, The novel coronavirus disease-2019 (COVID-19): mechanism of action, detection and recent therapeutic strategies, Virology 551 (2020) 1–9, https://doi.org/10.1016/j.virol.2020.08.011.

[37] N. Chen, M. Zhou, X. Dong, J. Qu, F. Gong, Y. Han, Y. Qiu, J. Wang, Y. Liu, Y. Wei, J. Xia, T. Yu, X. Zhang, L. Zhang, Epidemiological and clinical characteristics of 99 cases of 2019 novel coronavirus pneumonia in wuhan, China: a descriptive study, Lancet 395 (10223) (2020) 507–513, https://doi.org/10.1016/s0140-6736(20)30211-7.

[38] S. Guneyli, Z. Atceken, H. Dogan, E. Altinmakas, K.C. Atasoy, Radiological approach to COVID-19 pneumonia with an emphasis on chest CT, Diagn. Interventional Radiol. 26 (4) (2020) 323–332, https://doi.org/10.5152/dir.2020.20260.

[39] C.A. Raptis, M.M. Hammer, R.G. Short, A. Shah, S. Bhalla, A.J. Bierhals, P.D. Filev, M.D. Hope, J. Jeudy, S.J. Kligerman, T.S. Henry, Chest CT and coronavirus disease (COVID-19): a critical review of the literature to date, Am. J. Roentgenol. 215 (4) (2020) 839–842, https://doi.org/10.2214/ajr.20.23202.

[40] L. A. Valentino, M. W. Skinner, S. W. Pipe, The role of telemedicine in the delivery of health care in the COVID-19 pandemic, Haemophilia 26 (5). doi:10.1111/hae.14044.

[41] B. Wang, Y. Liu, Y. Wang, W. Yin, T. Liu, D. Liu, D. Li, M. Feng, Y. Zhang, Z. Liang, Z. Fu, S. Fu, W. Li, N. Xiong, G. Wang, F. Luo, Characteristics of pulmonary auscultation in patients with 2019 novel coronavirus in China, Respiration 99 (9) (2020) 755–763, https://doi.org/10.1159/000509610.

[42] P. Zhang, B. Wang, Y. Liu, M. Fan, Y. Ji, H. Xu, M. Xu, S. Chen, Q. Li, Z. Zhang, Lung auscultation of hospitalized patients with SARS-CoV-2 pneumonia via a wireless stethoscope, Int. J. Med. Sci. 18 (6) (2021) 1415–1422, https://doi.org/10.7150/ijms.54987.

[43] M. Sebastiani, A. Manfredi, C. Vacchi, G. Cassone, P. Faverio, A. Cavazza, N. Sverzellati, C. Salvarani, F. Luppi, Epidemiology and management of intersti-

tial lung disease in ANCA-associated vasculitis, In: CLINICAL AND EXPERIMENTAL RHEUMATOLOGY. - ISSN 0392-856X. - 38:2(2020), pp. 221-231.

[44] P. La Torraca, L. Ausiello, G. Zucchi, A. Farina and F. Pancaldi, "Identification of Soft Tissue-Mimicking Materials and Application in the Characterization of Sensors for Lung Sounds," in IEEE Sensors Journal, vol. 22, no. 1, pp. 1012-1019, 1 Jan.1, 2022, doi: 10.1109/JSEN.2021.3130546.

[45] M. Modena, A. Bertacchini, F. Paltrinieri, L. Dibiase and F. Pancaldi, "Modeling and Simulation of a Vibrating Membrane for the Acquisition of Lung Sounds," in IEEE Sensors Journal, vol. 25, no. 13, pp. 24421-24430, 1 July1, 2025, doi: 10.1109/JSEN.2025.3567733.

[46] A. Malko and V. Huckfeldt, “Physician shortage in Canada: A review of contributing factors,” Global J. Health Sci., vol. 9, no. 9, p. 68, Jun. 2017, doi: 10.5539/gjhs.v9n9p68.

[47] X. Zhang, D. Lin, H. Pforsich, and V. W. Lin, “Physician workforce in the United States of America: Forecasting nationwide shortages,” Hum. Resour. Health, vol. 18, no. 1, Dec. 2020, doi: 10.1186/s12960-020- 0448-3.

[48] H. Dumesnil, R. Lutaud, J. Bellon-Curutchet, A. Deffontaines, and P. Verger, “Dealing with the doctor shortage: A qualitative study exploring French general practitioners’ lived experiences, difficulties, and adaptive behaviours,” Family Pract., vol. 41, no. 6, pp. 1039–1047, Dec. 2024, doi: 10.1093/fampra/cmae017.

[49] B. Ofori, S. Twum, S. N. Yeboah, F. Ansah, and K. A. N. Sarpong, “Towards the development of cost-effective point-of-care diagnostic tools for poverty-related infectious diseases in sub-Saharan Africa,” PeerJ, vol. 12, Jun. 2024, Art. no. e17198, doi: 10.7717/ peerj.17198.

[50] X. Li, Y. Shang, J. Wei, and Y. Zhou, “Research on electronic stethoscope system and signal processing algorithm,” J. Phys., Conf. Ser., vol. 2634, no. 1, Nov. 2023, Art. no. 012037, doi: 10.1088/1742- 6596/2634/1/012037.

[51] L. J. Nowak and K. M. Nowak, “An experimental study on the role and function of the diaphragm in modern acoustic stethoscopes,” Appl. Acoust., vol. 155, pp. 24–31, Dec. 2019, doi: 10.1016/j.apacoust.2019.05.009.

[52] C. H. M. Jenkins and U. A. Korde, “Membrane vibration experiments: An historical review and recent results,” J. Sound Vibrat., vol. 295, nos. 3–5, pp. 602–613, Aug. 2006, doi: 10.1016/j.jsv.2006.01.036.

[53] T. Takashina, M. Shimizu, T. Muratake, and S. Mayuzumi, “New stethoscope with extensible diaphragm,” Circulat. J., vol. 80, no. 9, pp. 2047–2049, 2016, doi: 10.1253/circj.cj-16-0193.

[54] S. H. Lee et al., “Fully portable continuous real-time auscultation with a soft wearable stethoscope designed for automated disease diagnosis,” Sci. Adv., vol. 8, no. 21, May 2022, doi: 10.1126/sciadv.abo5867.

[55] A. A. Shkel and E. S. Kim, “Continuous health monitoring with resonant-microphone-array-based wearable stethoscope,” IEEE Sensors J., vol. 19, no. 12, pp. 4629–4638, Jun. 2019, doi: 10.1109/JSEN.2019.2900713.

[56] V.-T. Tran and W.-H. Tsai, “Stethoscope-sensed speech and breath-sounds for person identification with sparse training data,” IEEE Sensors J., vol. 20, no. 2, pp. 848–859, Jan. 2020, doi: 10.1109/JSEN.2019.2945364.

[57] A. Manfredi et al., “Diagnostic accuracy of a velcro sound detector (VECTOR) for interstitial lung disease in rheumatoid arthritis patients: The InSPIRAtE validation study (INterStitial pneumonia in rheumatoid ArThritis with an electronic device),” BMC Pulmonary Med., vol. 19, no. 1, pp. 1–6, Dec. 2019, doi: 10.1186/s12890-019-0875-x.

[58] P. Y. Ertel, M. Lawrence, R. K. Brown, and A. M. Stern, “Transmission and filtration patterns,” Circulation, vol. 34, no. 5, pp. 899–909, 1966.

[59] H. Pasterkamp, S. S. Kraman, and G. R. Wodicka, “Respiratory sounds,” Amer. J. Respiratory Crit. Care Med., vol. 156, no. 3, pp. 974–987, Sep. 1997, doi: 10.1164/ajrccm.156.3.9701115.

[60] A. A. Alanazi, S. R. Atcherson, C. A. Franklin, and M. F. Bryan, “Frequency responses of conventional and amplified stethoscopes for measuring heart sounds,” Saudi J. Med. Med. Sci., vol. 8, no. 2, pp. 112–117, 2020, doi: 10.4103/sjmms.sjmms_118_19.

[61] M. Sarkar, I. Madabhavi, N. Niranjan, and M. Dogra, “Auscultation of the respiratory system,” Ann. Thoracic Med., vol. 10, no. 3, pp. 158–168, 2015, doi: 10.4103/1817-1737.160831.

[62] Michael G. Levitzky, Pulmonary physiology, LANGE Physiology Series, McGraw-Hill Education: New York, NY, USA, 2007.

[63] I. A. Karnovsky and O. I. Lebed, Free vibrations of beams and frames, McGraw-Hill Professional, 2004.

[64] K. R. Rajagopal, "A note on a reappraisal and generalization of the Kelvin–Voigt model", Mechanics research communications, no. 2, vol. 36, pp. 232-235, 2009, DOI: 10.1016/j.mechrescom.2008.09.005

[65] M. Caputo, “Linear Models of Dissipation whose Q is almost Frequency Independent-II”, Geophysical journal international, no. 5, vol. 13, pp. 529-539, 1967.

[66] S. R. Ward and R. L. Lieber, “Density and hydration of fresh and fixed of human skeletal muscle”, Journal of biomechanics, no. 11, vol. 38, pp. 2317-2320, 2005, DOI: 10.1016/j.jbiomech.2004.10.001

[67] K. Comley and N. A. Fleck, “A micro-mechanical model for the Young’s modulus for adipose tissue”, International Journal of Solids and Structures, no. 21, vol. 47, pp. 2982-2990, 2010, DOI: 10.1016/j.ijsolstr.2010.07.001

[68] J. Liu, H. Zheng, P. S. P. Poh, H.-G. Machens and A. F. Schilling, “Hydrogels for engineering of perfusable vascular network”, International journal of molecular sciences, no. 7, vol. 16, pp. 15997-16016, 2015, DOI: 10.3390/ijms160715997

[69] A. I. Dyachenko, M. V. Veremyeva and E. S. Fomina, “Elasticity and viscosity of surface tissues of the human chest wall”, Russian Journal of Biomechanics, no. 2, vol. 21, pp. 164-174, 2017, DOI: 10.15593/RJBiomech/2017.2.06

[70] https://littmann.3mitalia.it/3M/it_IT/p/d/b00036656/, accessed online on January 3rd, 2025.

[71] S. S. Rao, Mechanical vibrations, New York: Addison-Wesley, 1995.

[72] Datasheet of the analog MEMS microphone Knowles SPM0687LR5H-1 Rev A, accessed online on January 3rd, 2025.

[73] B. Dianat, P. La Torraca, A. Manfredi, G. Cassone, C. Vacchi, M. Sebastiani, F. Pancaldi, “Classification of pulmonary sounds through deep learning for the diagnosis of interstitial lung diseases secondary to connective tissue diseases”, Comput. Biol. Med., no. 160, 2023, DOI: 10.1016/j.compbiomed.2023.106928.

[74] G. Sgalla, S. L. F. Walsh, N. Sverzellati, S. Fletcher, S. Cerri, B. Dim- itrov, D. Nikolic, A. Barney, F. Pancaldi, L. Larcher, F. Luppi, M. G. Jones, D. Davies, and L. Richeldi, “”velcro-type” crackles predict spe- cific radiologic features of fibrotic interstitial lung disease,” BMC Pul- monary Medicine, vol. 18, no. 1, Jun. 2018.

[75] F. Pancaldi, M. Sebastiani, G. Cassone, F. Luppi, S. Cerri, G. Della Casa, and A. Manfredi, “Analysis of pulmonary sounds for the diagnosis of interstitial lung diseases secondary to rheumatoid arthritis,” Computers in Biology and Medicine, vol. 96, pp. 91–97, May 2018.

[76] J. Driedger, M. Muller, and S. Ewert, “Improving time-scale modifi- cation of music signals using harmonic-percussive separation,” IEEE Signal Processing Letters, vol. 21, no. 1, pp. 105–109, Jan. 2014.

[77] A. Sakula, R T H Laënnec 1781--1826 his life and work: a bicentenary appreciation”, Thorax 1981 Feb;36(2):81-90. doi: 10.1136/thx.36.2.81.